2-7-2008

Focal waveform of a prolate-spheroidal impulse radiating antenna (IRA)

Serhat Altunc

Recommended Citation

Altunc, Serhat. "Focal waveform of a prolate-spheroidal impulse radiating antenna (IRA)." (2008). https://digitalrepository.unm.edu/ece_etds/13

Serhat Altunc
Candidate

Electrical and Computer Engineering
Department

This dissertation is approved, and it is acceptable in quality and form for publication on microfilm:

Approved by the Dissertation Committee:

, Chairperson

Accepted:

Dean, Graduate School

Date

FOCAL WAVEFORM OF A PROLATE-SPHEROIDAL IMPULSE RADIATING ANTENNA (IRA)

BY

SERHAT ALTUNC

B.S., ECE, Istanbul Technical University, 2000
M.S., ECE, Yildiz Technical University, 2003

DISSERTATION

Submitted in Partial Fulfillment of the
Requirements for the Degree of

Doctor of Philosophy

Engineering

The University of New Mexico
Albuquerque, New Mexico

December, 2007

DEDICATION

Dedicated to my family, especially my parents Gunar, Sehmus Altunc and my wife, Burcu…

Dedicated to my dreams…

ACKNOWLEDGMENTS

I wish to express my gratitude towards Dr. Edl Schamiloglu, my advisor and dissertation chair, for his help from admission to graduation.

I also thank my committee members, Dr. Carl E. Baum, Dr. Christos G. Christodoulou, for their valuable recommendations pertaining to this study and assistance in my professional development. Gratitude is extended to the Air Force Office of Scientific Research for the funding to pursue this research.

Finally, I would like to specially thank my parents Gunar and Sehmus Altunc and my wife, Burcu, for their support and continual motivations that I could gain valuable knowledge out of my work and I could finish it successfully.

Anne, baba, kardeslerim ve esim hersey icin cok tesekkurler…

FOCAL WAVEFORM OF A PROLATE-SPHEROIDAL IMPULSE RADIATING ANTENNA (IRA)

BY

SERHAT ALTUNC

ABSTRACT OF DISSERTATION

Submitted in Partial Fulfillment of the
Requirements for the Degree of

Doctor of Philosophy

Engineering

The University of New Mexico
Albuquerque, New Mexico

December, 2007

FOCAL WAVEFORM OF A PROLATE-SPHEROIDAL IMPULSE RADIATING ANTENNA (IRA)

by

Serhat Altunc

B.S., ENGINEERING, ISTANBUL TECHNICAL UNIVERSITY, 2000
M.S., ENGINEERING, YILDIZ TECHNICAL UNIVERSITY, 2003
PH.D., ENGINEERING, UNIVERSITY OF NEW MEXICO, 2007

ABSTRACT

Impulse Radiating Antennas (IRAs) are designed to radiate very fast pulses in a narrow beam with low dispersion and high field amplitude. For this reason they have been used in a variety of applications.

IRAs have been developed for the transient far-field region using paraboloidal reflectors. However, in this dissertation we focus on the near field region and develop the field waveform at the second focus of a prolate-spheroidal IRA. Recent research has shown that it is possible to kill certain skin cancers by the application of fast, high-amplitude electric-field pulses. This has been accomplished by the insertion of electrodes near the tumor, with direct contact from a high-voltage pulse generator. It has been suggested that it would be desirable to be able to apply fast, high-electric-field pulses without direct contact for this biological application, i.e., to irradiate them using an antenna from a distance.

Analytical, numerical and experimental behaviors for the focal waveforms of two and four-feed arm prolate-spheroidal IRAs are explored. With appropriate choice of the driving waveform we maximize the impulse field at the second focus. The focal waveform of a prolate-spheroidal IRA has been explained theoretically, verified experimentally and simulated using the CST-MWS (Microwave Studio) software. Finally, different lens design procedures are discussed for a prolate-spheroidal IRA for better concentrating the energy from an impulse.

TABLE OF CONTENTS

LIST OF FIGURES

LIST OF TABLES

1 INTRODUCTION

The Impulse Radiating Antenna (IRA) is a special kind of focused aperture antenna suited for radiating very fast pulses in a narrow beam. A fast-rising step-like signal into the antenna gives an approximate delta-function response. IRAs are composed of two main parts, a conical TEM transmission line and a focusing optic which is usually either a reflector or a lens. There are two types of IRAs according to the focusing optics used. Reflector IRAs use a paraboloidal reflector and lens IRAs use lenses for focusing the fields in the aperture.

For large antenna apertures fed by a single source (pulser) an efficient design uses a conical transmission line which feeds a paraboloidal reflector. An alternate design has a conical transmission line (TEM horn) feeding a lens with a special resistive termination in the rear of the antenna; for large antennas the lens can be quite massive, but for small antennas this type of design is quite practical. A third approach is a transient array involving many sources feeding an aperture.

In this dissertation we design a reflector IRA in which a prolate spheroid is used as a reflector for a biological application [1,2]. We feed our prolate-spheroidal IRA from the first focal point and concentrate the impulse at the second focal point [3,4].

IRAs have application as high-power pulse radiators, transient radars, and antennas capable of operating across many frequencies simultaneously. Several studies have been performed to improve the performance of IRAs. The basic development and research on IRAs has been carried out at the Air Force Research Laboratory (AFRL) at Kirtland Air Force Base. At first IRAs were designed for military applications. Now, they are finding applications in the civilian sector.

1.1 History of IRA

The wideband properties of the 2-N port Electron Scanning Radar (ESR) was observed at Lincoln Laboratory in the early 1960's, thus giving birth to Ultra-Wide-Band (UWB) technology. Several new theories have been proposed for UWB transmitters and receivers. UWB theory was improved to be used in communications, radar applications and coding schemes. In the early 1980's, UWB technology was used in ground penetrating radars, which was an initial step for other subsurface antennas. Finally, UWB technology has been implemented in military and civilian applications and a new antenna called the IRA was proposed by Baum [5]. The first IRA was built by Giri [6] and is presented in Figure 1.1.

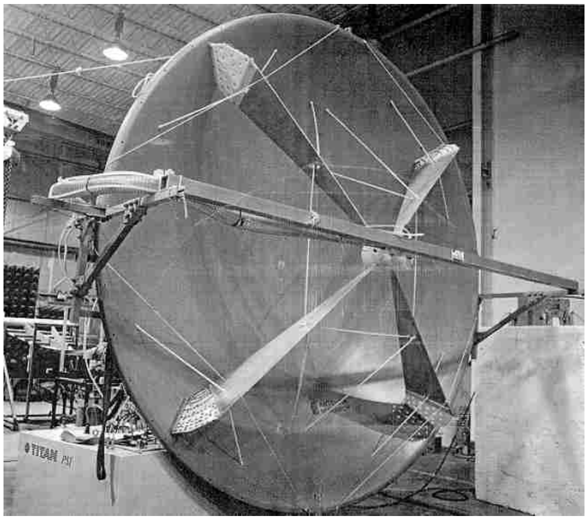

Figure 1.1: The 12-foot diameter reflector IRA built by Giri [6].

1.2 Motivation for IRAs and Applications

The basic motivation for developing IRA systems is to radiate large amplitude, large-band-ratio, undispersed pulses. In the remote-sensing arena such antennas are appropriate for transient radars, including for buried target recognition. Some consideration has also been given to their possible use in ionospheric research. The UWB technology can also be used in communication systems. The necessity of wider frequency bandwidth increases rapidly, so for high-quality data transfer and fast communication, the importance of UWB technology in communication systems increases.

Fast high-amplitude electric-field pulses can be used to kill skin cancer. This has been demonstrated by the insertion of electrodes near the tumor, with direct contact from a high-voltage pulse generator. Our motivation in this dissertation is to apply fast, high-electric-field pulses without direct contact for killing skin cancer, i.e., to irradiate them using a prolate-spheroidal IRA. This technique is much more convenient than inserting electrodes near the tumor [1].

1.3 Overview

In this dissertation, a new manifestation of an IRA, in which we use a prolate spheroid as a reflector instead of a paraboloid reflector and focus in the near-field region instead of the far-field region, was investigated. The focal waveform of the prolate-spheroidal IRA has been compared analytically, numerically and experimentally.

In Chapters 2-4, we present the theoretical background of IRAs that should be considered in the design and analysis of IRAs with their TEM feed sections. We use CST Microwave Studio to simulate our prolate-spheroidal IRA, and the numerical results are presented in Chapter 5. Chapter 6 is devoted to experiments which we performed at the University of New Mexico (UNM) Transient Antenna Laboratory in order to compare our experimental results with our analytical and numerical results. In Chapter 7, different lens design strategies are discussed for improved concentration of energy at the focal point. Finally, a brief summary of what has been explained in this dissertation and what should be done in future work is discussed.

2 BASICS OF IRAs

2.1 Introduction

In this chapter the IRA structure and components are discussed and the stereographic projection of aperture fields for TEM conical transmission lines is presented. Then, we illustrate the IRA waveform and the constituents of this waveform. The most important problem for broadband systems is creating a non-dispersive antenna so that the shape of the pulse is preserved. IRAs are an appropriate choice to accomplish this.

The theory of transformation from spherical wave to plane wave will be covered in the following sections. In order to obtain a planar phase front, the length of the antenna should be sufficiently large compared to the dimension of the aperture. This requires larger horns which are impractical to use. The idea of focusing the waves using a prolate spheroid is introduced, which provides a planar phase front without requiring large horn antennas.

2.2 Components and Waveform from a Reflector IRA

The reflector IRA is ideally composed of a conical-nondispersive TEM feed and a paraboloidal reflector which is a prolate spheroid in our case. IRAs can be better characterized as dispersionless, high band-ratio antennas. An IRA with a reflector and the idealized IRA waveform are depicted in Figure 2.1, where F is the focal length, D is the diameter of the reflector and c is the speed of light. The number of feed arms of reflector

IRAs are typically either two or four. Arms above the symmetry plane are at voltage $+V_0/2$ and arms below the symmetry plane are at voltage $-V_0/2$.

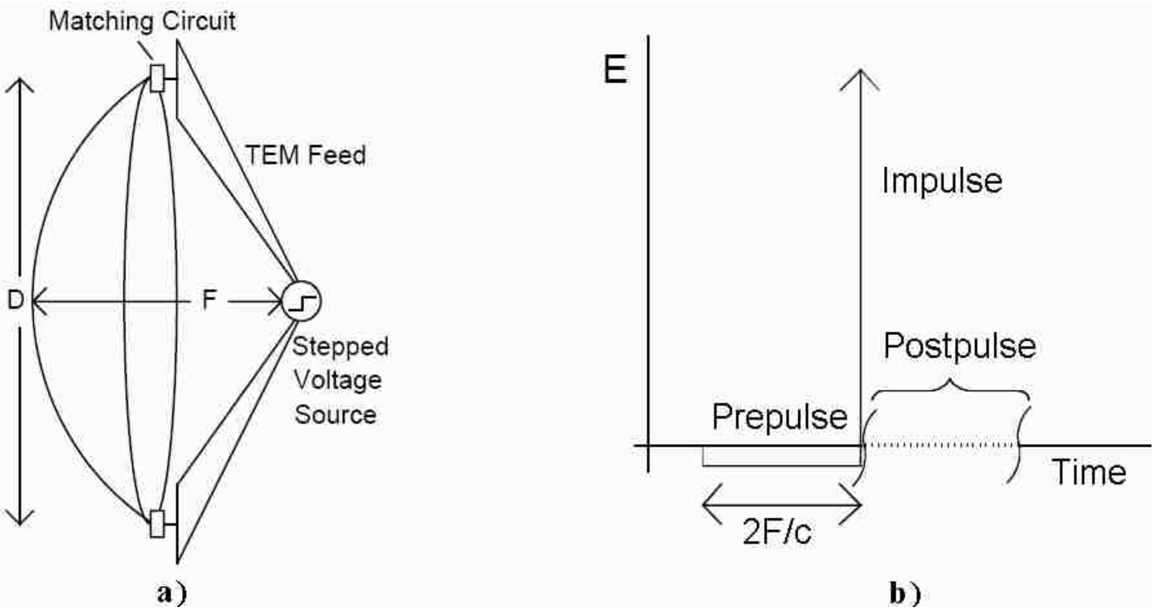

Figure 2.1: a) Paraboloidal reflector IRA; b)idealized IRA waveform [6].

The idealized IRA waveform on boresight has three main parts as depicted in Figure 2.1 b). The first of these is the prepulse, the direct radiation from the feed, which has a low magnitude and lasts a long duration (2F/c). When the apex of the TEM feed is first excited by the step-like function, the input wave travels a distance F towards the reflector and then another distance F backwards from the reflector, totaling a distance 2F in time t at the speed of light c in free space. Then we have an impulse which lasts for a short time and has a large amplitude. Finally, we have a postpulse expected after the impulse. Since radiating an impulse is the purpose of an IRA, we concentrate on the impulse part of the waveform. However, we also want to understand the behavior of the prepulse, since the areas under the prepulse and impulse are comparable. Under the assumption that the area under the postpulse curve is zero, the area of the prepulse and the area of the approximate delta function should be equal in order to satisfy the requirement that the total area under the step-response curve with the time axis should be zero because a finite antenna cannot radiate DC power.

The prepulse and impulse will dominate the early-time behavior of the IRAs, and the postpulse will inform us about the late-time behavior of the IRAs. Because of diffraction effects and the fields outside the aperture, the behavior of the postpulse will change according to the specifics of the design. Therefore, the behavior of the postpulse is as important as the behavior of the prepulse portion of the radiation, especially to find the exact matching circuits between the TEM feeds and the reflector.

We transform spherical geometry into cylindrical geometry to simplify the feed calculations and magnitude of the prepulse a calculation that is termed a stereographic projection in the literature [2,7]. Then the 2-D problem will be solved using conformal mapping.

2.3 Stereographic Projection

We can write Laplace's equation $\nabla^2 V = 0$, in 3D spherical coordinates as

$$\nabla^2 V = \frac{1}{r^2}\frac{d}{dr}\left[r^2 \frac{dV}{dr}\right] + \frac{1}{r^2\, sin\theta}\frac{d}{d\theta}\left[sin\theta \frac{d}{d\theta} V(\theta,\phi)\right] + \frac{1}{r^2\, sin^2\theta}\frac{d^2}{d^2\phi} V(\theta,\phi) = 0 . \tag{2.1}$$

Letting V be independent of r we have [7]

$$sin\theta\frac{d}{d\theta}\left[sin\theta\frac{d}{d\theta}V(\theta,\phi)\right]+\frac{d^2}{d^2\phi}V(\theta,\phi)=0\,. \tag{2.2}$$

We can decrease the dimensionality of the problem and simplify the calculations from 3-D to 2-D using a stereographic projection. The process of stereographic projection is basically representing every point on a spherical surface on an infinite plane while preserving angles. A tangent plane is taken at one end of the diameter of the sphere. Inhomogeneous TEM waves in a uniform, isotropic medium are exactly transformed by stereographic projection into a second set of such waves in the case of paraboloidal and hyperboloidal scatterers, provided the incident wave is centered on an appropriate focal point (including infinity) of these quadric surfaces [8,9]. In our case, we consider the prolate spheroid, which is a special case of an ellipsoid, as another quadric surface. One spherical or planar TEM wave can be transformed into another with an exact matching of the boundary conditions on the reflector. This gives exact solutions of the Maxwell equations, valid up until some time related to a signal arriving at the observer from some truncation of the reflector or the presence of the feed arms.

The stereographic transformation takes the form as

$$\theta=2\,arctan\left[\frac{\sqrt{x^2+y^2}}{2r}\right]\ ,\ \phi=arctan(y/x)\,. \tag{2.3}$$

(2.3) is the inverse of

$$x=2r\,tan(\theta/2)\,cos\,\phi\ ,\ y=2r\,tan(\theta/2)\,sin\,\phi\ . \tag{2.4}$$

We can simplify our problem by substituting (2.3) in (2.2) to obtain the 2-D Laplace's equation as

$$\frac{d^2}{dx^2}V(x,y)+\frac{d^2}{dy^2}V(x,y)=0\,. \tag{2.5}$$

Equation (2.5) is just the 2-D Laplace's equation in cylindrical coordinates. One can convert 3-D conical symmetry (conical plates) to longitudinal symmetry by stereographic projection. The 3-D geometrical demonstration of the stereographic projection is shown in Figure 2.2.

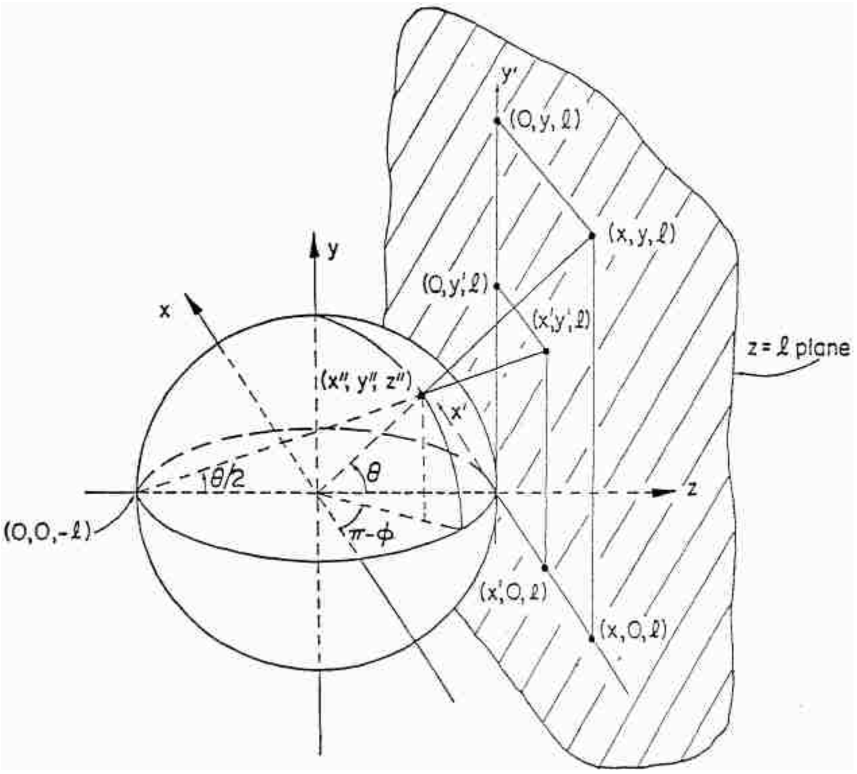

Figure 2.2: 3-D view of the stereographic projection can be used to decrease the dimensionality of the problem [6].

We have a little difficulty when one wants to know the fields at $\theta = \pi$. At that angle $tan(\pi / 2)$ approaches infinity and the transformation cannot be used for simplification. If we rotate the structure 180° about the y axis, then the angle that was formerly $\theta = \pi$ becomes $\theta = 0$. By carrying out the same transformation on the rotated structure, we can simply eliminate the singularity. A diagram of this is shown in Figure 2.2. In looking at the diagram, it is obvious that the field in the backward direction is much smaller than it is in the forward direction since the conductors in the projected plane are much further apart.

The procedure where we include the 180° rotation is called a reverse stereographic transformation. The net effect of the reverse stereographic transformation is to replace θ with $\theta - \pi$. Thus, after one has found the projection for the forward direction, it is straightforward to replace θ with $\theta - \pi$ to obtain the reverse transformation. This is illustrated in Figure 2.3.

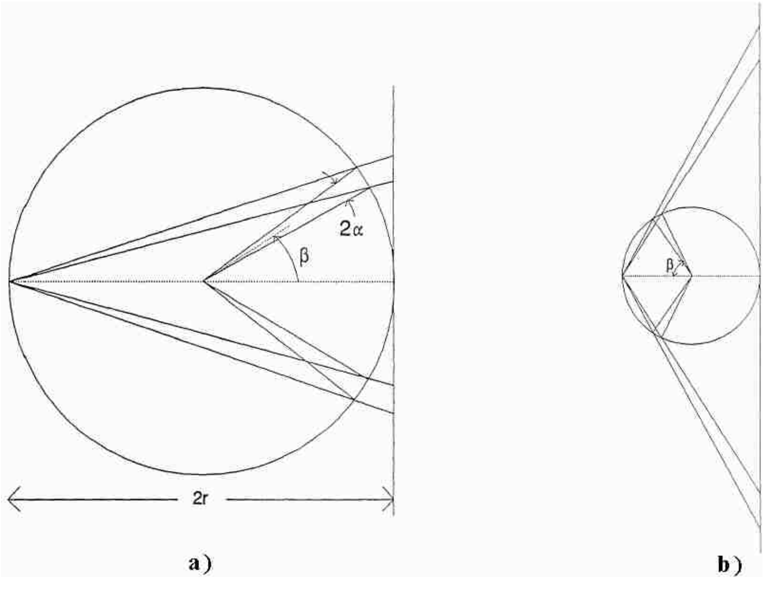

Figure 2.3: 2-D a) the stereographic projection; b)reverse stereographic projection [6].

3 PARAMETER STUDY FOR A PROLATE-SPHEROIDAL IRA

3.1 Introduction

This chapter presents the results from a parametric study of the focal waveform produced at the second focus of a prolate-spheroidal reflector due to a TEM wave launched from the first focus (Appendix A). We find the optimal dimensions and the *z*-coordinate of the truncation plane z_p for the reflector.

In order to find an optimal design we need to compare various designs on a common basis. For this purpose, we define a volume, based on a geometric shape that fills in some sense, to get the maximum performance. Consider a circular cylinder as in Figure 3.1 which has a length ℓ and radius of Ψ_0, where

$$\ell = a + z_0 = a + \left[a^2 - b^2\right]^{1/2} . \tag{3.1}$$

This is the distance from the back of the reflector (z = -a) to the target ($z = z_0$). This still leaves the radius Ψ_0 which we treat via the parameter Ψ_0 / ℓ. All distances are normalized to ℓ. The other parameters, *a* and *b*, are defined in Figure 3.1. Note that

for $z_p \geq 0$, $\Psi_0 = b$, (3.2)

for $z_p \leq 0$, $\Psi_0 = \Psi_p$.

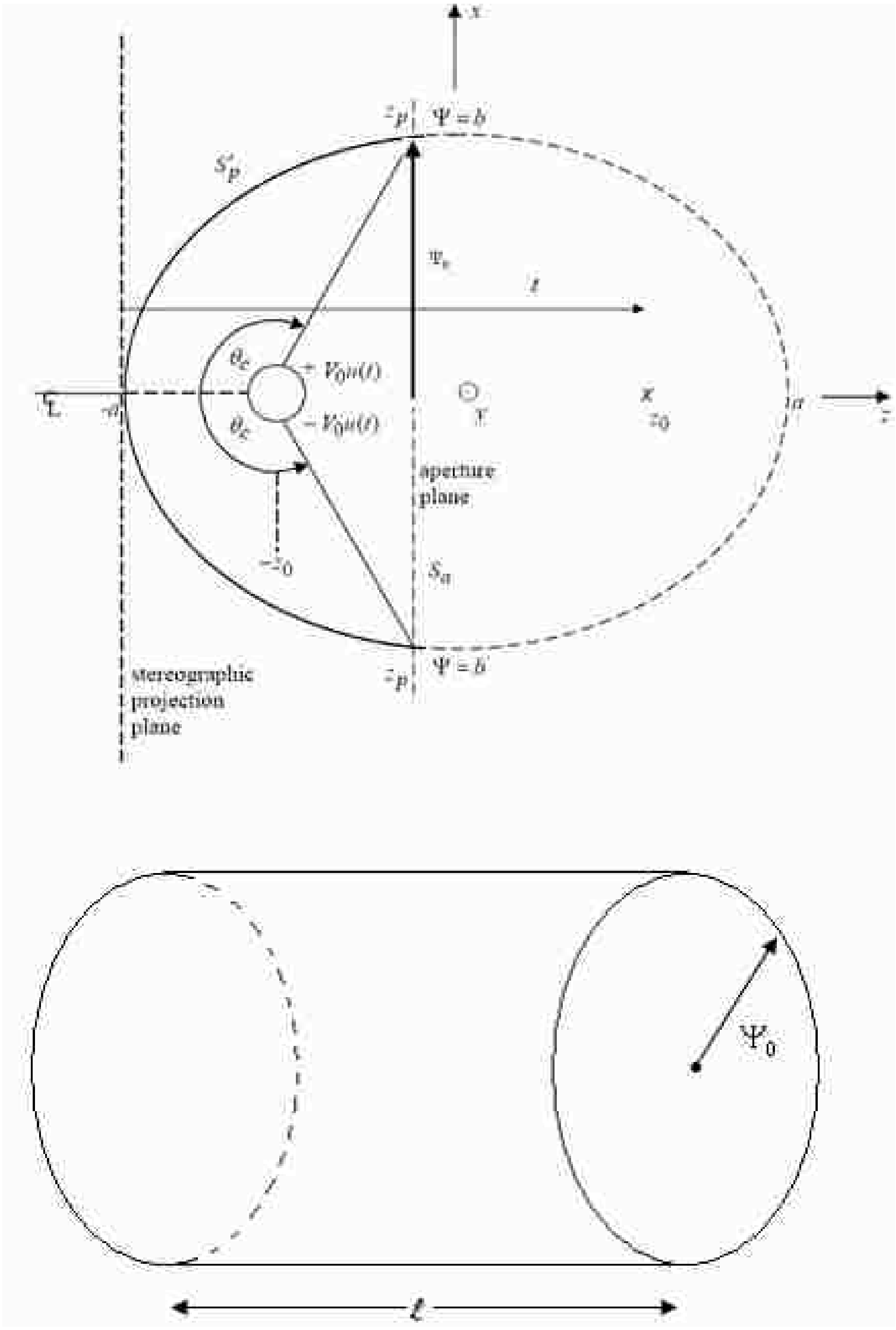

Figure 3.1: IRA and cylindrical geometry representation in which the IRA fits to get the maximum performance.

3.2 Normalized Parameters

All the geometrical parameters are normalized to ℓ as

$$\frac{a}{\ell}, \frac{b}{\ell}, \frac{z_0}{\ell}, \frac{\Psi_0}{\ell}, \frac{\Psi_p}{\ell}, \frac{z_p}{\ell}. \tag{3.3}$$

Normalized electromagnetic scaled parameters are:

$$e_\delta = E_\delta \frac{\pi f_g c}{V_0} \text{ impulse,} \tag{3.4}$$

$$e_p = E_p \frac{2\pi f_g \ell}{V_0} \text{ prepulse (step, negative),} \tag{3.5}$$

$$e_{pa} = E_p \Delta t_p \frac{2\pi f_g c}{V_0} \text{ prepulse integral (area), and} \tag{3.6}$$

$$e_s = E_s \frac{2\pi f_g \ell}{V_0} \text{ postpulse step.} \tag{3.7}$$

One can see that the impulse peak is the ratio of

$$E_i = E_\delta / t_\delta , \tag{3.8}$$

where t_δ is the "impulse width" or "rise time" of the source.

E_δ and E_s are the impulse and step terms from the reflection in the prolate sphere and E_p is the magnitude of the prepulse, z_p is the z-coordinate of the truncation plane, a and b are the two radii for the prolate spheroid, z_0 is the focal distance, $\Delta t_p = 2[a - z_0]/c$ is the length of the prepulse and $f_g = Z_c / Z_0$ is the transmission line parameter. These parameters are discussed in detail in Appendix A. We can find the ratio of impulse to prepulse as (should be large)

$$\frac{1}{E_p}\frac{E_\delta}{t_\delta} = \frac{2\ell}{ct_\delta}\frac{e_s}{e} . \tag{3.9}$$

The normalized geometric parameters $a/\ell, b/\ell, z_0/\ell, \Psi_p/\ell$ with respect to z_p/ℓ are presented in Figure 3.2 and 3.3.

The normalized electromagnetic parameters are presented in Figures 3.4-3.7. We want to obtain the largest impulse amplitude and the smallest prepulse and postpulse amplitudes. The Ψ_0/ℓ term determines the "fatness" of the reflector and z_p/ℓ term determines the truncation plane for the reflector. At the focal point e_δ is the dominant term and it is a constructive term for the impulse; however, e_p is a destructive term for the impulse. e_s is a constructive term for both the impulse and postpulse. Thus, we have a tradeoff among these terms, but our basic concern is the e_δ term**.** We should also consider the geometrical construction problem.

3.2.1 Normalized Geometric Parameters $a/\ell, b/\ell, z_0/\ell, \Psi_p/\ell$

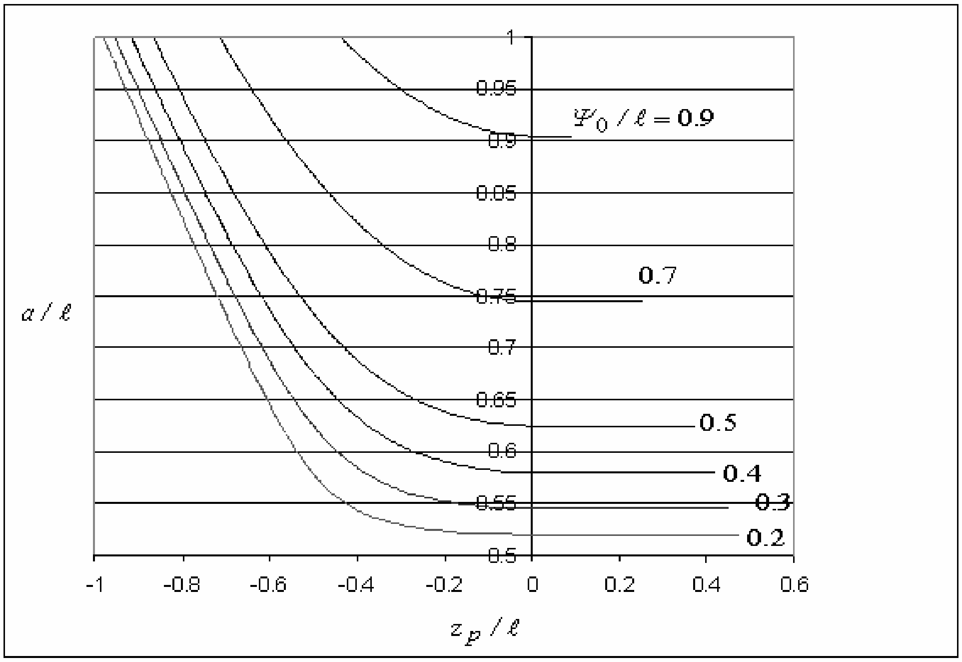

a)

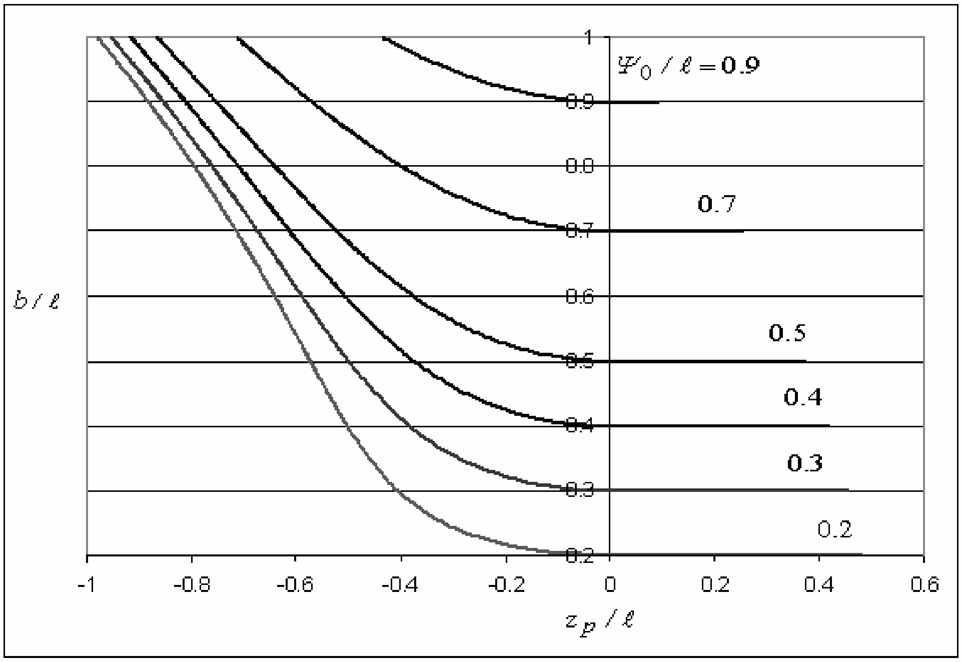

b)

Figure 3.2: The normalized geometric parameters of prolate-spheroidal IRA for different Ψ_0/ℓ; a) a/ℓ with respect to z_p/ℓ; b) b/ℓ with respect to z_p/ℓ.

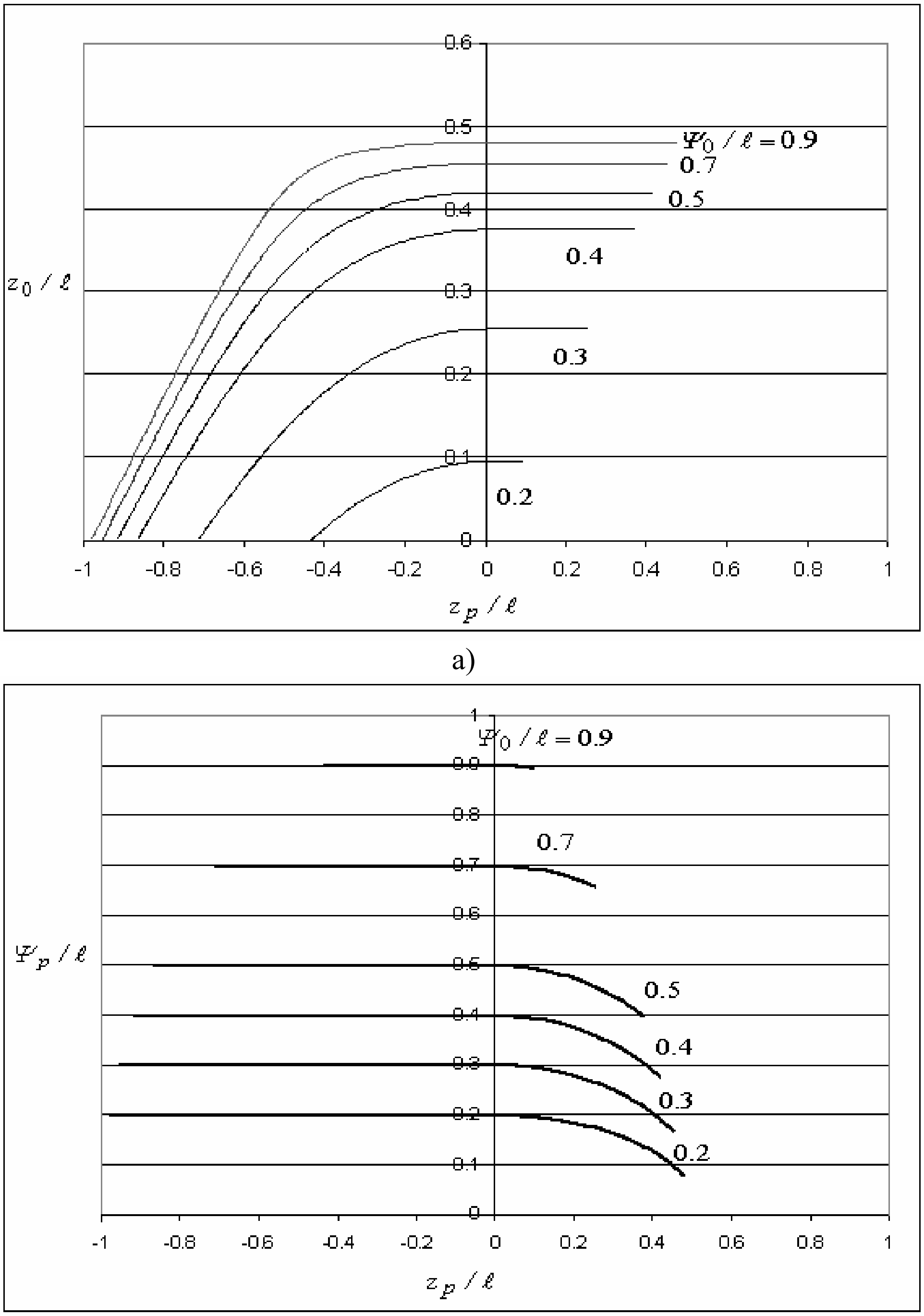

a)

b)

Figure 3.3: The normalized geometric parameters of prolate-spheroidal IRA for different Ψ_0/ℓ; a) z_0/ℓ with respect to z_p/ℓ; b) Ψ_p/ℓ with respect to z_p/ℓ.

3.2.2 Normalized Electromagnetic Parameters

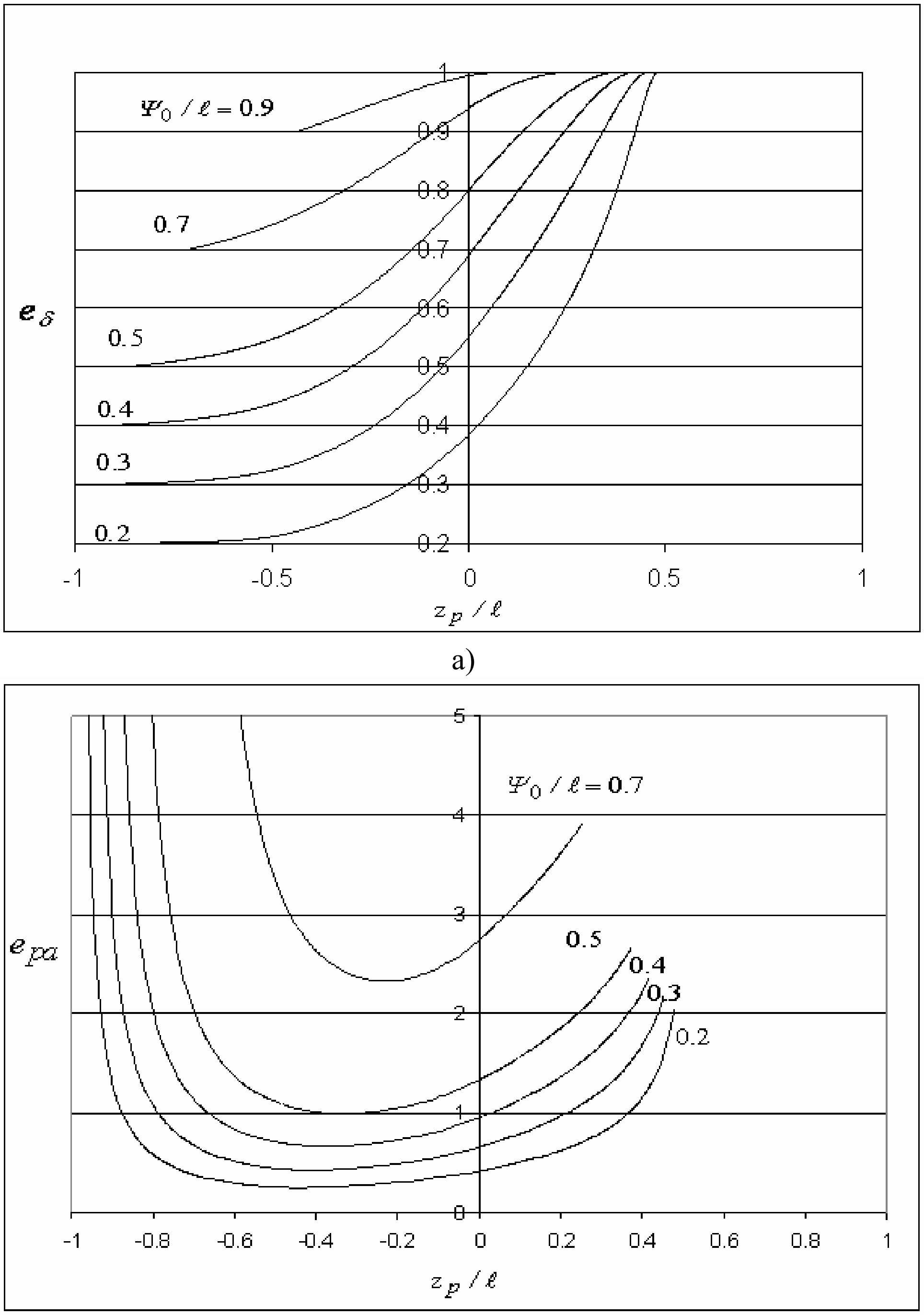

a)

b)

Figure 3.4: Normalized electromagnetic parameters of prolate-spheroidal IRA for different Ψ_0 / ℓ; a) e_δ with respect to z_p / ℓ; b) e_{pa} with respect to z_p / ℓ.

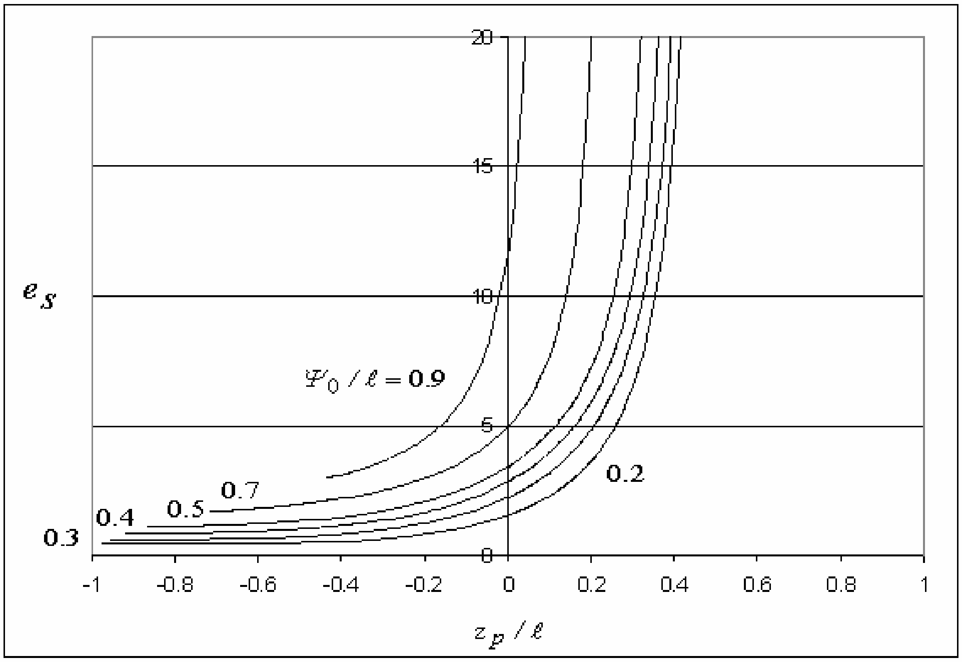

a)

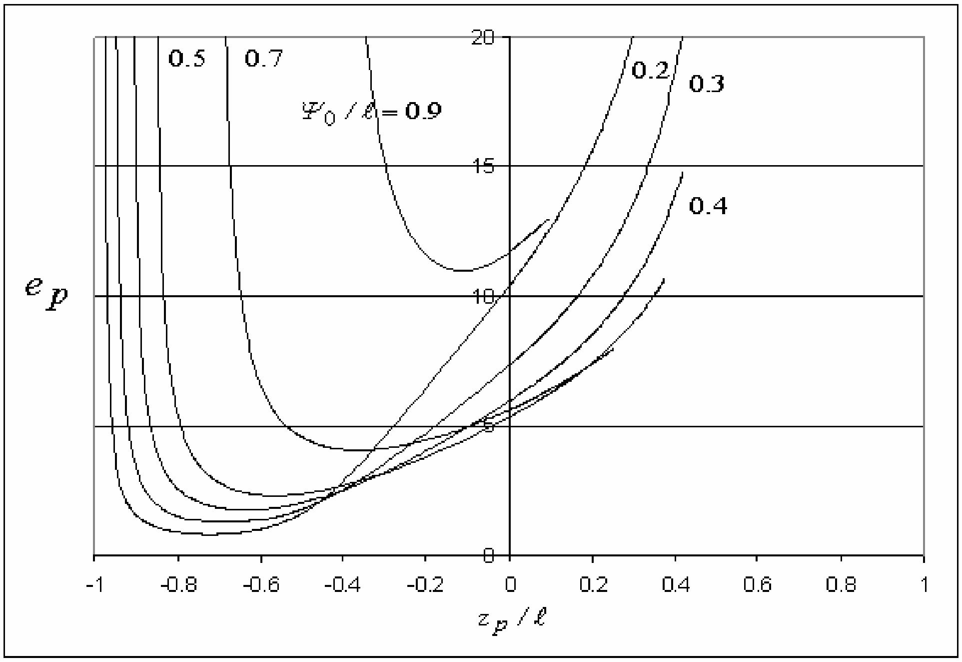

b)

Figure 3.5: Normalized electromagnetic parameters of prolate-spheroidal IRA for different Ψ_0 / ℓ; a) e_s with respect to z_p / ℓ; b) e_p with respect to z_p / ℓ.

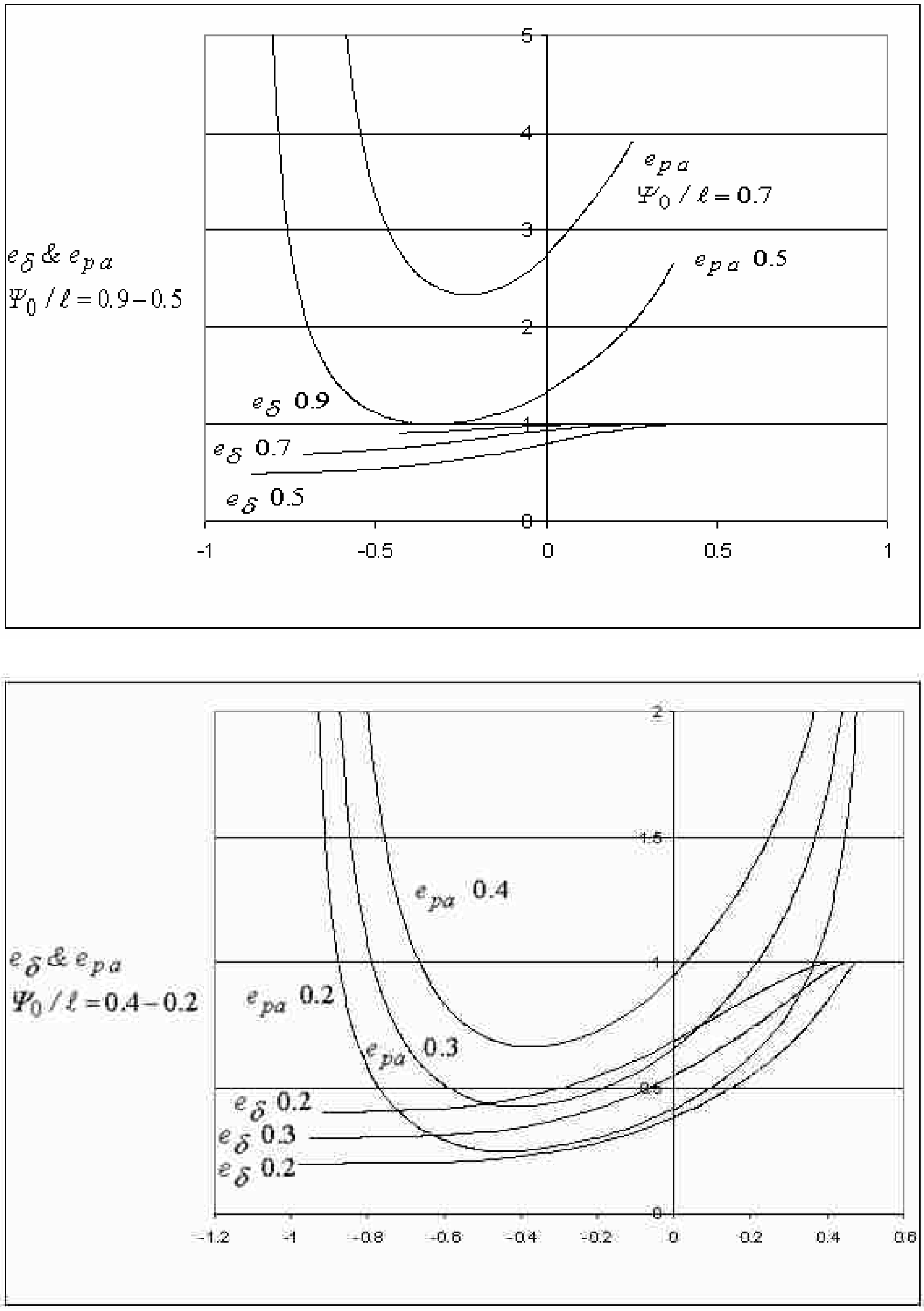

Figure 3.6: Normalized electromagnetic parameters of prolate-spheroidal IRA; e_δ *and* e_{pa} with respect to z_p/ℓ for different Ψ_0/ℓ.

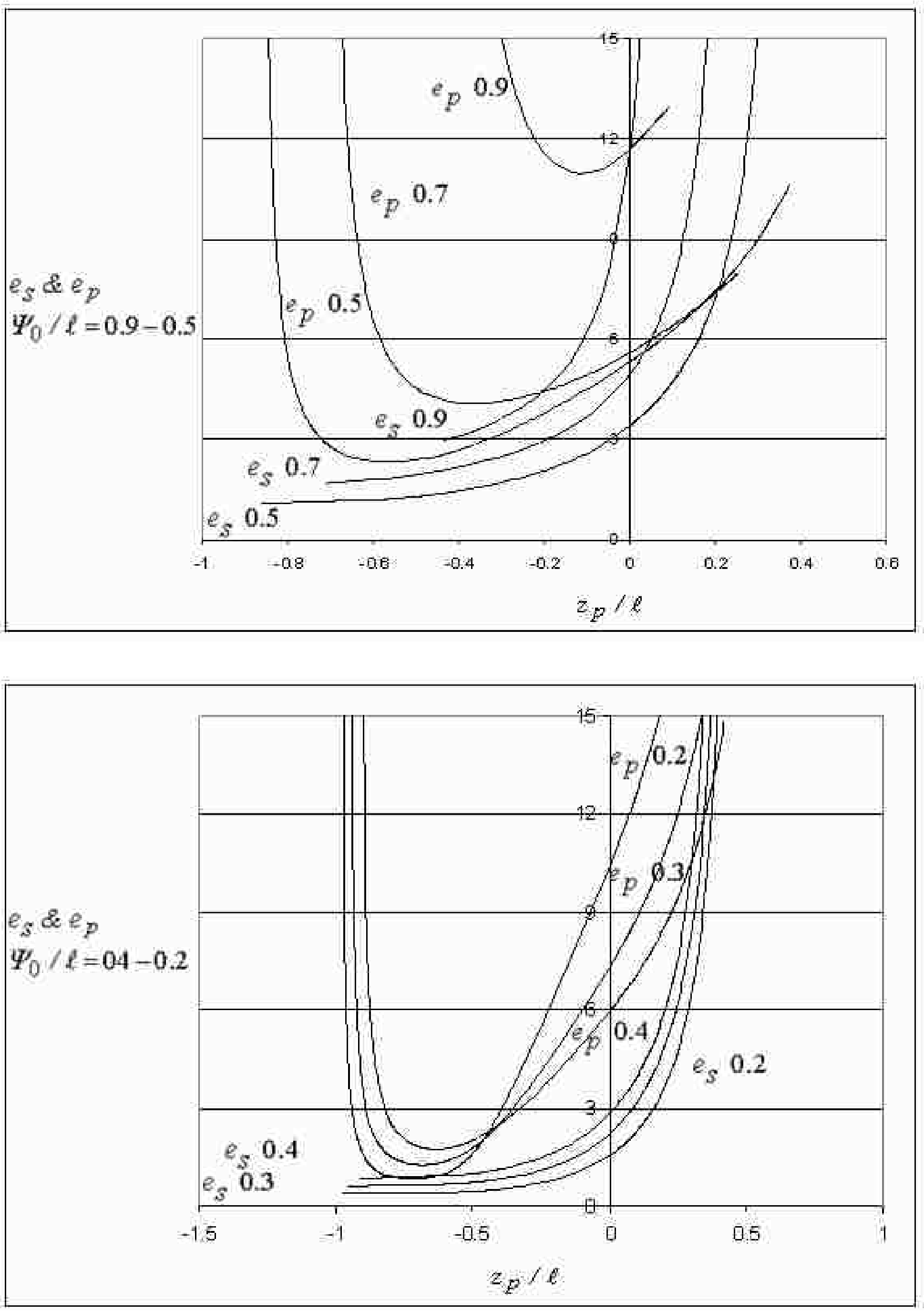

Figure 3.7: Normalized electromagnetic parameters of prolate-spheroidal IRA; e_s *and* e_p with respect to z_p / ℓ for different Ψ_0 / ℓ.

One can see from Figure 3.4 a) that e_δ has a maximum value for $\Psi_0 / \ell = 0.9$ and small z_p / ℓ values; for z_p / ℓ values greater then 0.4 all the e_δ values approach unity. From Figure 3.4 b) we can see that the e_{pa} prepulse integral (area) has the minimum value around $z_p / \ell = -0.25$ and for larger Ψ_0 / ℓ we have larger e_{pa}; it is decreasing the impulse amplitude. From Figure 3.5 the behavior of e_s and e_p can be analyzed; for $\Psi_0 / \ell = 0.9$ both e_s and e_p have the largest values for smaller Ψ_0 / ℓ; e_s and e_p values do not change that much. In Figure 3.7 we compare e_s *and* e_p values we can analyze the postpulse characteristics.

We have different parameters to determine the fatness of the reflector Ψ_0 / ℓ and the truncation plane z-coordinate z_p / ℓ. Our basic concern is the impulse term. We have analyzed the electromagnetic parameters and we decide to have

$$\begin{aligned} \Psi_0 / \ell &= 0.5 \\ z_p / \ell &= 0. \end{aligned} \tag{3.10}$$

For this case (3.10) the reflector can be easily constructed and we can use the symmetry of our geometry.

3.3 Example Case

3.3.1 Feed-Point Lens

We can use the feed-point lens to increase (bump up) the field as illustrated in Figure 3.8.

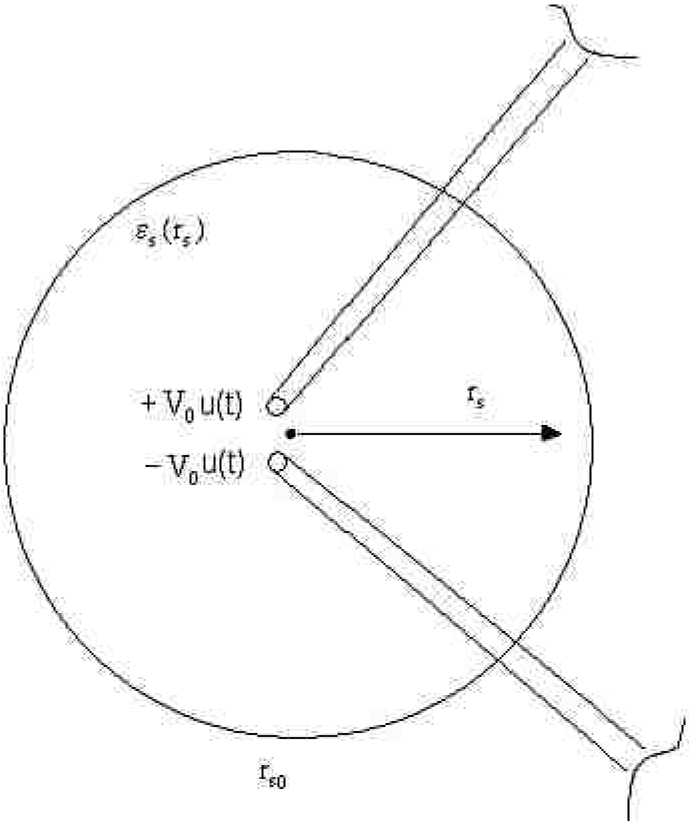

Figure 3.8: Feed-point lens geometry which can be used to increase the field.

3.3.2 Spherical Example

$$\text{Let } \varepsilon_{rs} = \frac{\varepsilon_s}{\varepsilon_0} \quad , \quad \varepsilon_{rs}(0) \geq \varepsilon_{rs}(r_s) \geq 1 \; (air) . \tag{3.11}$$

A typical value of the relative dielectric constant of transformer oil for the feed-point lens is $\varepsilon_{rs} = 2.25$ (transformer oil).

For uniform transmission in air we have

$$T = \frac{2}{1+\varepsilon_{rs}^{-1/2}} = 1.2 . \tag{3.12}$$

This requires a graded lens like a transmission-line transformer

$$T = \varepsilon_{rs}^{1/4}(0) = 1.22 \text{ (for example not much improvement).} \tag{3.13}$$

3.3.3 Example Case Parameters

We use a special case, (3.10) and (3.14), for our reflector:

$$\frac{b}{\ell} = 0.5 \quad , \quad \frac{a}{\ell} = 0.625 \quad , \quad \frac{z_0}{\ell} = 0.375 \quad , \quad \frac{b}{a} = \frac{4}{5} \quad , \quad \frac{z_0}{a} = \frac{3}{5} . \tag{3.14}$$

This parameters are illustrated in Figure 3.9.

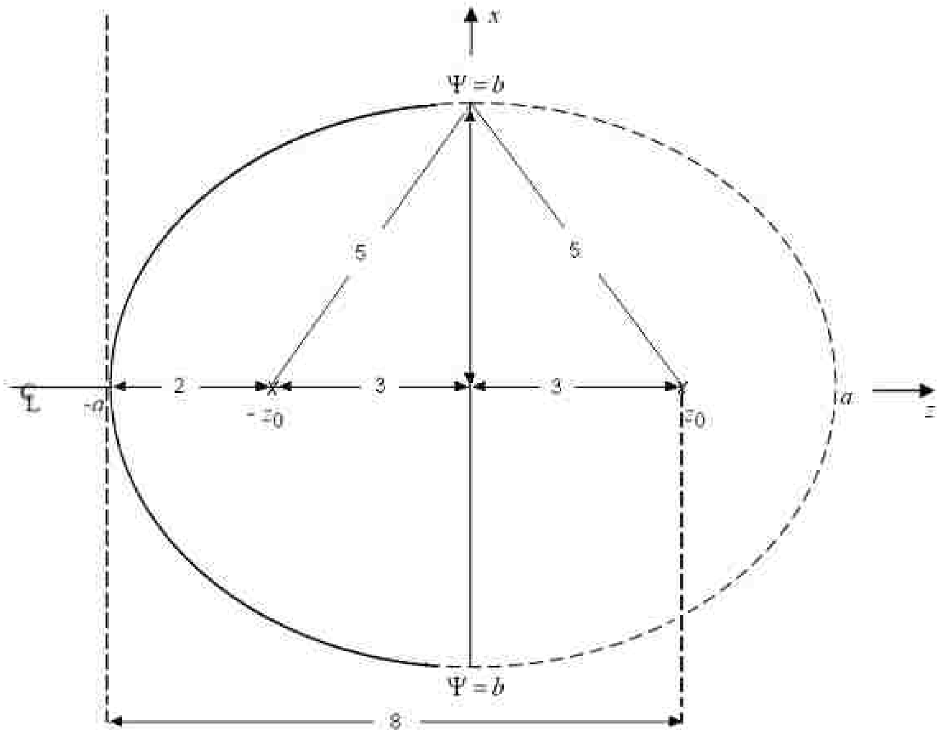

Figure 3.9: Geometrical dimensions for the example case given in (3.14).

Let us assume we have a source voltage (pulse rising in time t_δ) that may be used as a source for later experiments:

$$V_0 = 10^5\ V \quad (2\text{x}10^5 \text{ differential}). \tag{3.15}$$

The other parameters can be assumed as

$$t_\delta = 100\, ps\ ,\ f_g = 1.06\,. \tag{3.16}$$

One can find the normalized impulse and prepulse terms from Figure 3.4 and 3.5 for

$\Psi_0 / \ell = 0.5$ and $z_p / \ell = 0$ as

$$e_\delta = 0.8\ ,\ e_p = 5.4\ . \tag{3.17}$$

Thus, for this specific example we have an impulse term at the second focal point as

$$E_i = \frac{E_\delta}{t_\delta} T = \frac{V_0 e_\delta}{\pi f_g c t_\delta} T = 0.96\, MV / m\ .$$

The ratio of impulse peak to prepulse amplitude can be found as

$$\frac{1}{E_p} \frac{E_\delta}{t_\delta} = \frac{2\ell}{c t_\delta} \frac{e_\delta}{e_p} = 9.9\,\ell\ . \tag{3.18}$$

If we use $\ell = 1$ meter as the normalization length, we will have a 9.9 ratio of impulse peak to prepulse amplitude.

This modest study has found some curves useful for estimating the focal waveforms and focal spot size for the two-arm prolate-spheroidal IRA. Considering the sophisticated design papers which followed the introduction of the IRA concept, there is much yet to be done for the prolate-spheroidal version. This is adequate for designing experiments to demonstrate and validate the design concept.

4 EXTENSION OF ANALYTICAL CALCULATIONS FOR THE FOCAL WAVEFORM OF A PROLATE-SPHEROIDAL IRA

4.1 Introduction

This chapter presents the development of the field waveform at the second focus of a prolate-spheroidal reflector and it is an extension of Appendix A [3]. We explore the analytic behavior of the waveforms near the second focal region. With appropriate choice of the driving waveform we can maximize the impulse field at the second focus. IRAs have been developed for the transient far-field region [6] and are recognized as a significant advance in antenna technology [10]. Related experimental and numerical aspects of this problem can be found in [11,12]. In this chapter we focus mainly on the near fields that can be used in some biological applications [1].

First of all, we calculate the focal waveform analytically. We analyze the behavior of the waveform near the second focus and show that the impulse part of the waveform at the second focus can be described by a delta-like pulse forming for $z < z_0$ and in the limit as $z \to z_0$ gives the required true delta function. This is a physical example of the formation of a delta function. Then, the aperture integral gives the same result (at early time) as the exact incident wave before truncation. This gives confidence in the aperture integration. We can see that the area of the $\delta - like$ pulse is the same for both before and after z_0. We illustrate these results with a graphical example. We continue the analytical evaluation of the prepulse term E_{p_2} after the impulse, when the aperture integral is truncated by the aperture edge. From previous and present results, the actual analytical waveform is illustrated, including all the terms. These analytical calculations are for a two-arm prolate-spheroidal IRA; however, we can easily extend these calculations to four 45^o and 60^o TEM feed arm cases.

Finally, the time domain characteristics of some analytic source waveforms used for determining the waveform characteristic of a prolate- spheroidal IRA at the second focus are discussed.

4.2 Description of Geometry

Using the prolate-spheroidal IRA given in Appendix A and [3], we choose a special case with the following geometric parameters (see Figure 4.1):

$$z_p = 0,\, b = \Psi_0 = .5m,\, a = .625\ m\ ,\, z_0 = .375m, \ell = 1m, \tag{4.1}$$

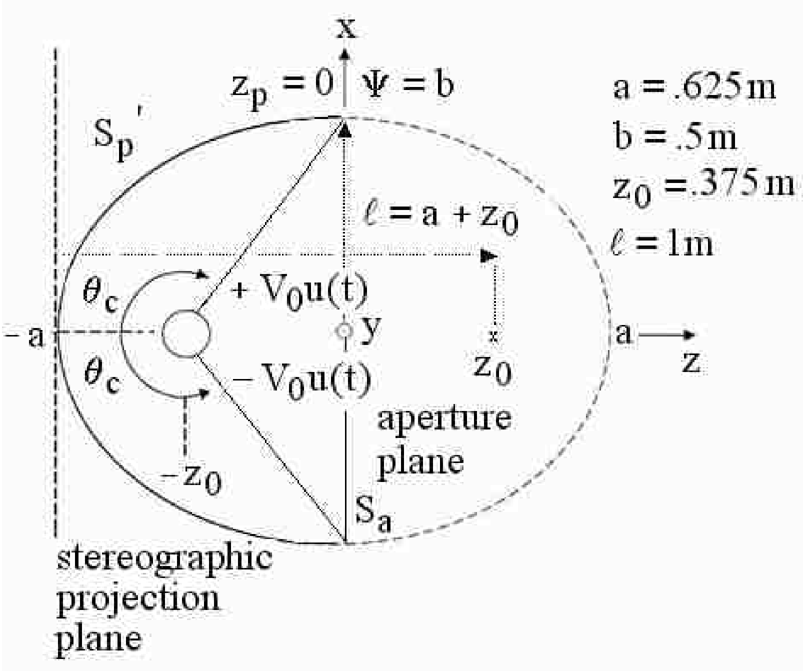

Figure 4.1: Schematic diagram of a prolate-spheroidal IRA with special geometric parameters defined in (4.1).

where z_p is the z-coordinate of the truncation plane, a and b are the two radii for the prolate spheroid, z_0 is the focal distance and ℓ is the distance that can be used for normalization.

For our later example calculations, our design has two TEM feed arms and the dimensions of these arms are determined by a $400\ \Omega$ pulse impedance ($\phi_0 = 90^o$). This design considers the two-arm case, but analytical results can be simply extended to the four-arm case [13,14].

The feed-arm parameters have been previously calculated in the stereographic projection plane as [15]

$$\begin{aligned} &{b_0}^2 = b_1 b_2 \\ &(b_1 - b_2)/b_0 = 0.275. \end{aligned} \tag{4.2}$$

b_0, b_1 and b_2 are the stereographic projections of the feed arms, from which we find the angles for the two-feed arms as

$$\begin{aligned} &\beta_0 = arctan(.5/.375) \cong 53.1^o \\ &\beta_1 = 2\,arctan\left[\sqrt{b_1/b_2}\,tan(\beta_0/2)\right] = 47^o \\ &\beta_2 = 2\,arctan\left[\sqrt{b_1/b_2}\,tan(\beta_1/2)\right] = 59.6^o\,. \end{aligned} \tag{4.3}$$

$\beta_0, \beta_1, \beta_2$ are the angles from the *z*-axis to the electrical center, the first edge and the second edge of the feed arms as in Figure 4.2.

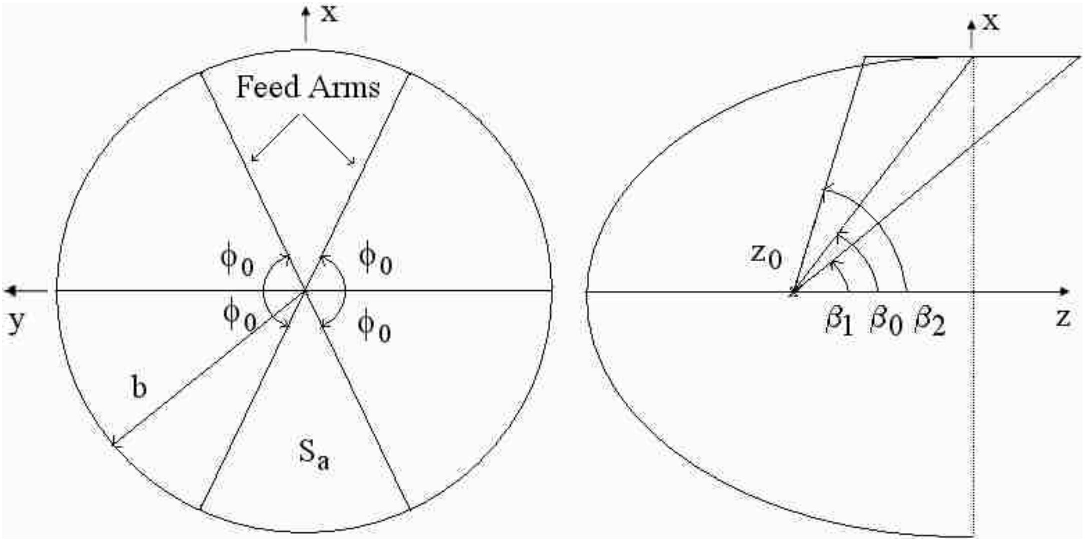

Figure 4.2: Prolate-spheroidal IRA feed arm geometry for four-arm case.

From equations (4.1)-(4.3) and [15], one can find the locations and dimensions of the feed arms. The feed arms are symmetric and the upper feed arm has three corners, whose locations are summarized in Table 4.1

Table 4.1: Upper feed arm's corner locations for two feed-arm case (cm).

x	y	z
0	0	-37.5
50	0	-8.2
50	0	8.99

For our later example calculations, our design has four TEM feed arms and the dimensions of these arms are determined by a $200\ \Omega$ pulse impedance ($\phi_0 = 45^o,\ 60^o$). The feed-arm parameters, b_0, b_1, b_2, have been previously calculated in the stereographic projection plane for $\phi_0 = 60^o$ [15] as

$$b_0{}^2 = b_1 b_2 \ , \ (b_1 - b_2)/b_0 = 0.521, \tag{4.4}$$

from which we find the angles for the four-feed arms as

$$\begin{aligned} &\beta_0 = arctan(.5/.375) \cong 53.1^o \ , \ \beta_1 = 2\,arctan\left[\sqrt{b_1/b_2}\,tan(\beta_0/2)\right] = 42.23^o \\ &\beta_2 = 2\,arctan\left[\sqrt{b_2/b_1}\,tan(\beta_0/2)\right] = 65.77^o \,. \end{aligned} \tag{4.5}$$

From (4.4), (4.5) and Table 1 [15], we can find the locations and dimensions of the feed arms. The feed arms are symmetric and the upper fed arms have three corners, whose locations are summarized in Table 4.2.

Table 4.2: Upper feed arms' corner locations for 60^o four-TEM-feed-arm (cm).

Right			Left		
x_1	y_1	z_1	x_2	y_2	z_2
0	0	-37.5	0	0	-37.5
43.3	25	-15	43.3	-25	-15
43.3	25	18	43.3	-25	18

In this chapter, we concentrate on three different types of feed-arm geometry based on the choice of ϕ_0, the feed arm angle. The first feed design has two 90^o TEM feed arms and the dimensions of these arms are determined by a 400 Ω pulse impedance. The second and third designs use 45^o *and* 60^o TEM feed arms and the dimensions of these arms are determined by a 200 Ω pulse impedance. The 45^o case has the same dimensions as the two-arm case, by symmetry.

Farr introduced the voltage normalized gain as $G_v = h_a / f_g$ [16,17], and this can be used to compare with the radiation from two different antennas that have the same input voltage. Here h_a is the aperture height and $f_g = Z_c / Z_0$ is the impedance factor which relates the transmission-line impedance to the free space impedance. From Table 1 of [15] we can easily define

$$\begin{aligned} G_{v_1} &= \frac{.736}{200/377} = 1.387 \\ G_{v_2} &= \frac{.648}{200/377} = 1.221. \end{aligned} \tag{4.6}$$

G_{v_1} and G_{v_2} are the voltage gain for four 60^o feed-arm and 45^o (times .707 for the two-arm, $400\ \Omega$, case by symmetry) TEM-feed-arm case. If we divide G_{v_1} by G_{v_2}, we can determine the increase in the field if we use the 60^o feed-arm instead of 45^o feed-arm. Thus, we have $G_{v_1} / G_{v_2} = 1.135$. We know that we will have a $\sqrt{2}$ increase in the field values if we have four 45^o TEM feed arms instead of two arms, due to symmetry. We should have a $\left[G_{v_1} / G_{v_2}\right] \sqrt{2} = 1.606$ increase in the fields using the 60^o TEM-feed-arm case as compared with the two-arm case. In our design we used 60^o feed-arm because the voltage gain is nearly maximum [15] and it was easy to construct this geometrically.

4.3 The Actual Analytical Focal Waveform

The analytical focal fields in Appendix A and [3] are

$$E_\delta = \frac{V_0}{\pi f_g c} \frac{a+c}{a-c} cot\left(\frac{\theta_c}{2}\right) \left[1 - \left[1 + \left[\frac{\Psi_p}{z_0 - z_p} \right]^2 \right]^{-1/2} \right]$$

$$E_s = \frac{V_0}{2\pi f_g} \frac{1}{z_0 - z_p} \frac{a+z_0}{a-z_0} cot\left(\frac{\theta_c}{2}\right) \left[1 + \left[\frac{z_0 - z_p}{\Psi_p} \right]^2 \right]^{-1} \text{, and} \tag{4.7}$$

$$E_p = \frac{V_0}{2\pi f_g z_0} tan\left(\frac{\theta_c}{2}\right).$$

4.3.1 Calculating $tan(\theta_c / 2)$

We have a simpler form for $tan(\theta_c / 2)$ than in [3]. θ_c is bounded as $0 \le \theta_c \le \pi$.

By the geometric construction from Figure 4.1 we have

$$tan(\theta_c / 2) = sin^{-1}(\theta_c)\left[1 - cos(\theta_c)\right], \tag{4.8}$$

$$sin(\theta_c) = \Psi_p \left[{\Psi_p}^2 + \left[z_p + z_o \right]^2 \right]^{-1/2}, \tag{4.9}$$

$$cos(\theta_c) = -\left[z_p + z_o \right] \left[{\Psi_p}^2 + \left[z_p + z_o \right]^2 \right]^{-1/2}. \tag{4.10}$$

We have

$$tan(\frac{\theta_c}{2}) = \frac{1}{\Psi_p} \left[{\Psi_p}^2 + \left[z_p + z_o \right]^2 \right]^{1/2} \frac{\lfloor z_p + z_o \rfloor}{\Psi_p}. \tag{4.11}$$

Let us try to find $\left[{\Psi_p}^2 + \left[z_p + z_o \right]^2 \right]^{1/2}$ in terms of a, z_0, z_p.

$$\Psi_p = b\left[1-\left[z_p / z_o\right]^2\right]^{1/2}. \tag{4.12}$$

Substituting (4.12) in (4.11) we have

$$\left[\Psi_p{}^2 + \left[z_p + z_0\right]^2\right]^{1/2} = \frac{1}{a}\left[a^2 + z_0\, z_p\right]. \tag{4.13}$$

Substituting this in (4.8) we obtain

$$tan(\frac{\theta_c}{2}) = \left[\frac{a+z_p}{a-z_p}\right]^{1/2} \frac{a+z_0}{b}, \tag{4.14}$$

which is a simpler result compared with the result in [3].

4.3.2 Prepulse Term E_{p2} After the Impulse

What happens to the prepulse term after the impulse, i.e., after the truncation at the aperture boundary ($\Psi = \Psi_p$, or b for special case)? Before the aperture truncation the prepulse is given by (4.7).

Let E_{pt} = tangential E field (x component) on S_a due to the prepulse wave.

Then we have [3,18]

$$E_{p1} = \frac{1}{2\pi c}\frac{\partial}{\partial t}\int_{S_a} \frac{z_0 - z_p}{r_2{}^2} E_{pt}\, dS = 0 \quad \text{after wave passes}$$

$$E_{p2} = \frac{1}{2\pi}\int_{S_a} \frac{z_0 - z_p}{r_2{}^2} E_{pt}\, dS = \text{step wave left after the wave passes the aperture plane.} \tag{4.15}$$

These are both integrals of the r^{-1} fields from the first focus on the aperture plane. After we see the edge of S_a, neglecting diffraction terms from this edge and approximating E_{pt} by the negative of the TEM prepulse wave out to this edge (for a positive parameter as in [3]) we have, for step-function excitation, a time-independent prepulse field on S_a,

$E_{p_1} = 0$ the derivative being zero after the aperture edge is seen (4.16)

$E_{p_2} = \frac{1}{2\pi} \int \frac{z_0 - z_p}{r_2^{\,3}} E_{pt}\, dS$ = constant, i.e. a step term.

Next we require the static E_{pt}. As before, since we are confining ourselves to the z-axis we can use a uniform field on the projection plane to give E_{pt} in the above integral. From (2.11) of [3] at $r_1 = z_0$ (aperture plane center)

$$E_{pa0} \cong \frac{V_0}{z_0 \pi f_g} tan\left(\frac{\theta_c}{2}\right). \tag{4.17}$$

We need this extended over S_a since, as we have seen before, for the z axis only the uniform field terms (on the projection plane) need be considered (by symmetry). On the projection plane at $z = -a$ (2.7) in [3]

$$V(x_0,y_0)=\frac{V_0}{2}arccos\,h^{-1}\left(\frac{\Psi_{c0}}{r_{w0}}\right)ln\left(\frac{\left(\frac{\Psi_{c0}}{r_{w0}}\right)^2+2\frac{\Psi_{c0}}{r_{w0}}cos(\theta_1)+1}{\left(\frac{\Psi_{c0}}{r_{w0}}\right)^2-2\frac{\Psi_{c0}}{r_{w0}}cos(\theta_1)+1}\right), \tag{4.18}$$

$$\Psi_0=2[a-z_0]tan\left(\frac{\theta_1}{2}\right).$$

On the projection plane at $\Psi_0=0$ we need the uniform field component (x-directed)

$$V\cong\frac{V_0}{2}arccosh^{-1}\left(\frac{\Psi_{c0}}{r_{w0}}\right)ln\frac{2\frac{x}{\Psi_{c0}}+1}{-2\frac{x}{\Psi_{c0}}+1}\cong\frac{V_0}{2}arccosh^{-1}\left(\frac{\Psi_{c0}}{r_{w0}}\right)2\frac{x}{\Psi_{c0}}. \tag{4.18}$$

$$E_{4,0}=\frac{2V_0}{\Psi_{c0}}arccosh^{-1}\left(\frac{\Psi_{c0}}{r_{w0}}\right)=\frac{2V_0}{\pi f_g}\frac{1}{\Psi_{c0}}\ (taken\ as\ positive\ in\ our\ convention[1]).$$

Choose a potential (uniform)

$$V=E_{4,0}\,x=-\frac{2V_0}{\Psi_{c0}}arccos\,h^{-1}\left(\frac{\Psi_{c0}}{r_{w0}}\right)\Psi_0\,cos(\Phi_0)=-E_{40}\,\Psi_0\,cos(\Phi_0). \tag{4.19}$$

Map this back onto the $\overset{\rightarrow}{r_1}$ system

$$V=E_0\,2[a-z_0]tan\left(\frac{\theta_1}{2}\right)cos(\phi),$$

$$\Psi_{c0}=2[a-z_0]tan\left(\frac{\theta_c}{2}\right)=2[a-z_0]\left[\frac{a+z_p}{a-z_p}\right]^{1/2}\frac{a+z_0}{b}, \tag{4.20}$$

$$V=E_{4,0}\,2[a-z_0]tan\left(\frac{\theta_1}{2}\right)cos(\phi).$$

Now on S_a we have

$$\vec{E}_4 = \frac{1}{r_1}\nabla_{\theta_1,\phi_1} V = -E_{4,0}\,2\frac{[a-z_0]}{r_1}\left(\sec^2\left(\frac{\theta_1}{2}\right)\frac{1}{2}\cos(\phi)\,\vec{1}_{\theta_1} - \frac{\tan\left(\frac{\theta_1}{2}\right)}{\sin(\theta_1)}\sin(\phi)\,\vec{1}_{\phi_1}\right). \tag{4.21}$$

The tangential part and $cos(\theta_1)$ are

$$\begin{aligned} \vec{E}_{4t} &= E_{4,0}\frac{[a-z_0]}{r_1}\left(\sec^2\left(\frac{\theta_1}{2}\right)\frac{1}{2}\cos(\theta_1)\cos(\phi_1)\,\vec{1}_{\Psi} - 2\frac{\tan\left(\frac{\theta_1}{2}\right)}{\sin(\theta_1)}\sin(\phi)\,\vec{1}_{\phi_1}\right) \\ &= E_{4,0}\frac{[a-z_0]}{r_1}\left(\frac{2\cos(\theta_1)\cos(\phi_1)}{1+\cos(\theta_1)}\vec{1}_{\Psi} - 2\frac{\sin(\phi_1)}{1+\cos(\theta_1)}\vec{1}_{\phi_1}\right), \end{aligned} \tag{4.22}$$

$$r_1\left[1+\cos(\theta_1)\right] = r_1 + z_0 + z_p\,,$$

$$r_1 = \left[\Psi_0{}^2 + \left[z_0 + z_p\right]^2\right]^{1/2},$$

$$\cos(\theta_1) = \frac{z_0+z_p}{r_1}.$$

The x component is

$$\begin{aligned} E_{4x} &= E_{4,0}\frac{[a-z_0]}{r_1+z_0+z_p}\left[2\frac{z_0+z_p}{r_1}\cos^2(\theta_a) + 2\sin^2(\phi_a)\right], \\ E_{p2} &= E_{40}\left[z_0 - z_p\right]\left[a-z_0\right]\int_0^{\Psi_p}\frac{1}{r_2{}^3\,r_1}\,d\Psi . \end{aligned} \tag{4.23}$$

To solve this integral consider the special case $z_p = 0, \Psi_p = b, r_1 = r_2$. Then from (4.2) and (4.3) of [3]

$$E_{p2} = \frac{V_0}{\pi f_g} \frac{1}{\Psi_{c0}} \frac{[a - z_0]}{z_0} \left[1 + \left[\frac{z_0}{b} \right]^2 \right]^{-1} \text{ and}$$

$$\Psi_{c0} = 2[a - z_0] tan\left(\frac{\theta_c}{2} \right) = 2[a - z_0] \frac{[a + z_0]}{b}. \tag{4.24}$$

In the end we obtain

$$E_{p2} = \frac{V_0}{2\pi f_g} \frac{1}{z_0} \frac{b}{a + z_0} \left[1 + \left[\frac{z_0}{b} \right]^2 \right]^{-1}. \tag{4.25}$$

The normalized e_{p2} is

$$e_{p2} = \frac{2\pi f_g \ell}{V_0} E_{p2} = \frac{\ell}{z_0} \frac{b}{a + z_0} \left[1 + \left[\frac{z_0}{b} \right]^2 \right]^{-1}. \tag{4.26}$$

Note that this is actually the negative of the prepulse (to give a positive parameter) by convention in [3]. Let us find the ratio of $\frac{e_{p2}}{e_p}$ from (4.5) and (4.26)

$$\frac{e_{p2}}{e_p} = \left(\frac{b}{a + z_0} \right)^2 \left[1 + \left[\frac{z_0}{b} \right]^2 \right]^{-1} \left[\frac{a - z_p}{a + z_p} \right]^{1/2}. \tag{4.27}$$

For our case (4.1)

$$\frac{e_{p2}}{e_p} = \left(\frac{b}{a + z_0} \right)^2 \left[1 + \left[\frac{z_0}{b} \right]^2 \right]^{-1} = 0.16 < 1, \tag{4.28}$$

as expected, we have almost an 85% decrease in the prepulse.

4.3.3 The Graphical Illustration of the Actual Analytical Focal Waveform

We take the simple example case in (4.1) to illustrate the analytical waveform. The excitation is a 1 Volt ($V_0 = .5$ Volt) step, rising as a ramp function lasting 100 ps. One can calculate the analytical focal fields of a two-arm prolate-spheroidal IRA from (4.7) and (4.25) as

$$\begin{aligned} &E_p = 0.4 V/m \ \mathit{(negative\ prepulse)}, \\ &E_i = \frac{E_\delta}{t_\delta} = 4 V/m, \\ &E_s = 0.26 V/m, \\ &E_{p_2} = 0.06 V/m \ \mathit{(negative\ prepulse)}. \end{aligned} \tag{4.29}$$

We present this graphical illustration in Figure 4.3. We can easily extend this result for the four 45^o and 60^o TEM feed arms by multiplying all the values with $\sqrt{2}$ and 1.606. We present these results in Figure 4.4.

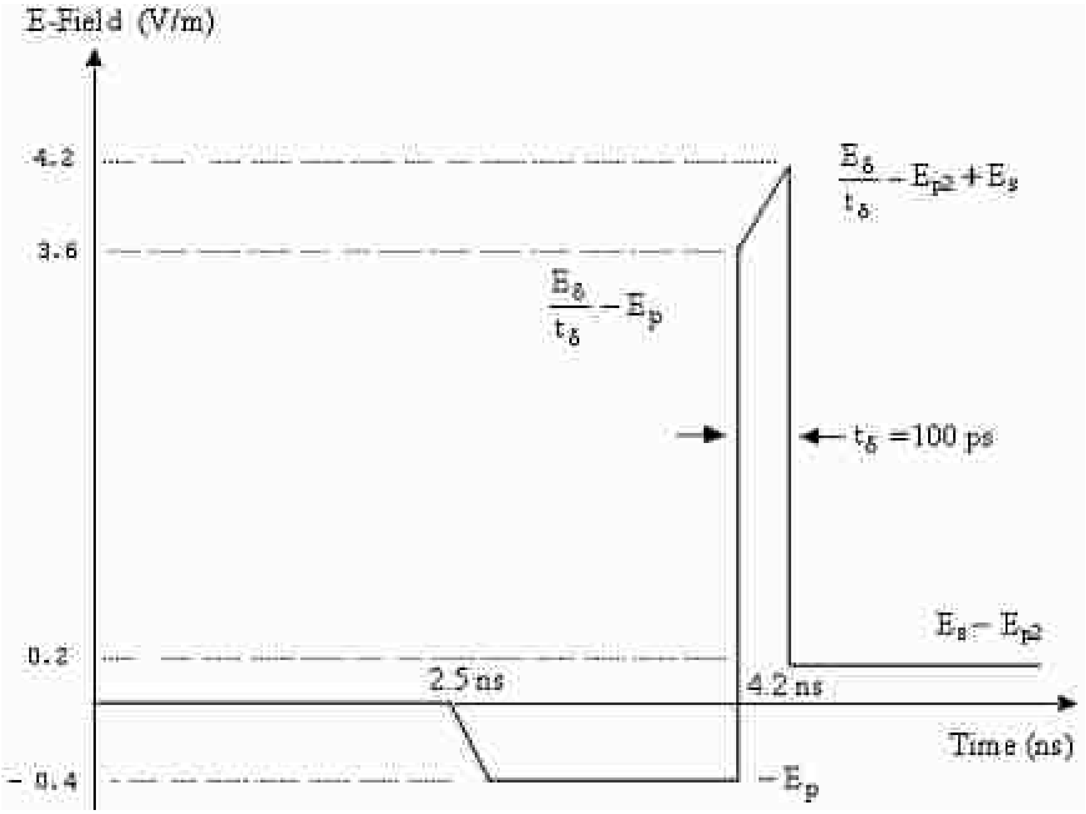

Figure 4.3: Analytic focal waveform at the second focus for a two-arm prolate-spheroidal IRA.

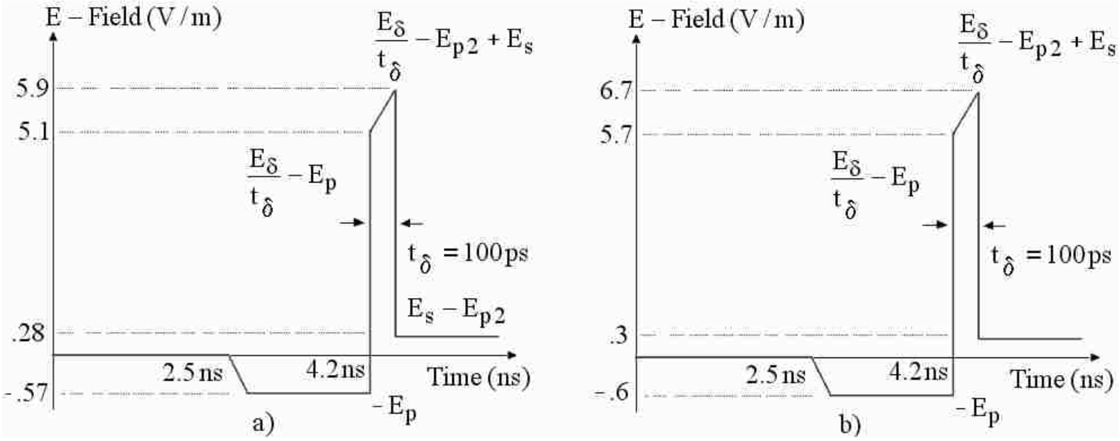

Figure 4.4: Analytic focal waveforms at the second focus a) 45^o b) 60^o four feed-arm prolate-spheroidal IRA.

4.4 Electric Field Variation Near Second Focus

4.4.1 Introduction

The electric field variation near the second focus is analyzed and with this analysis we prove that the impulse part of the waveform at the second focus can be described by a delta-like pulse forming for $z < z_0$ and in the limit as $z \rightarrow z_0$ gives the required true delta function. Then, the aperture integral gives the same result (at early time) as the exact incident wave before truncation. This gives confidence in the aperture integration. We can see that the area of the δ-like pulse is the same for both before and after z_0.

4.4.2 Exact Solution of the Impulse Term for $z < z_0$ up to Aperture Truncation of Signal

First, we will find the exact electric field E_3 for $z < z_0$ (as in Figure 4.5) for times after the pulse arrival when the solution no longer goes to 0.

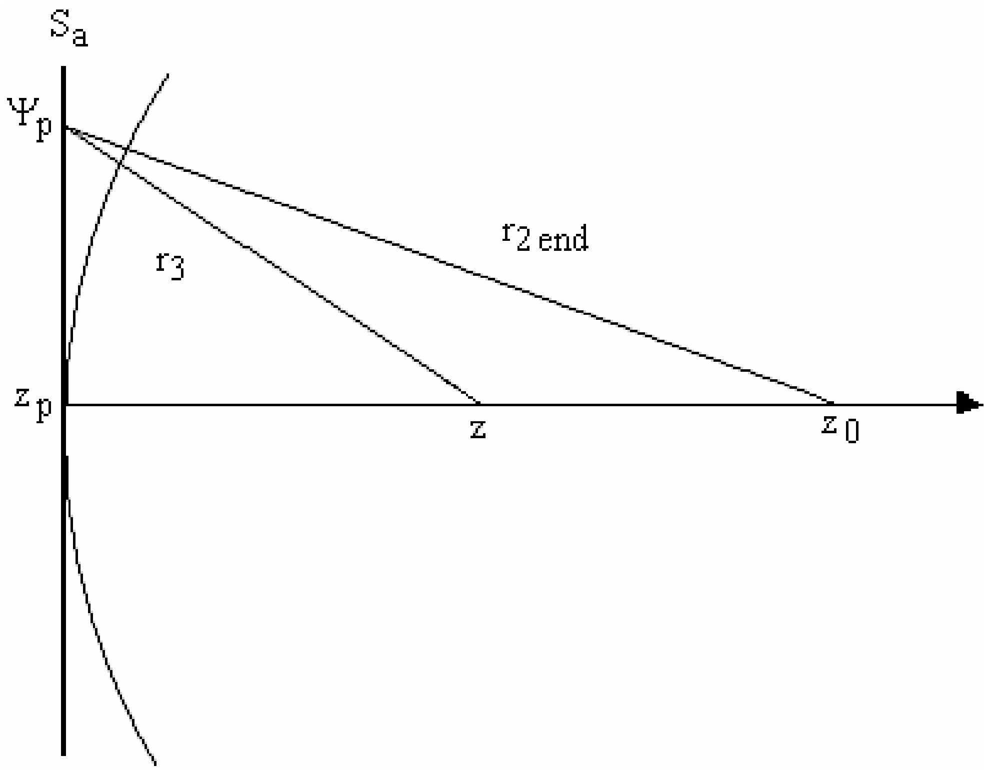

Figure 4.5: Graphical illustration of z values for $z < z_0$ used to calculate the retarded time for the field from $\Psi = \Psi_p$.

We can write (3.13) and (3.10) in [3] as

$$\vec{E}_2 = E_0 \frac{a+z_0}{r_2}\left[\frac{2\cos(\phi_2)}{1+\cos(\theta_2)}\vec{1}_{\theta_2} - \frac{2\sin(\phi_2)}{1+\cos(\theta_2)}\vec{1}_{\theta_2}\right] u\left(t+\frac{r_2}{c}-2\frac{a}{c}\right), \tag{4.30}$$

which is the tangential electric field on the aperture S_a from the reflection due to the prolate sphere.

On the z-axis $\theta_2 = 0$, ϕ_2 is arbitrary, let us take $\phi_2 = 0$, giving

$$\begin{aligned} &r_2 = z_0 - z, \\ &E_3 = E_0 \frac{a+z_0}{z_0 - z} u\left(t + \frac{r_2}{c} - 2\frac{a}{c}\right) \quad \text{(oriented in the } x\text{-direction).} \end{aligned} \tag{4.31}$$

Substitute E_0 *and* $\cot(\theta_c / 2)$ in E_3 to obtain

$$E_3 = \frac{V_0}{\pi f_g} \frac{1}{z_0 - z} \left[\frac{a - z_p}{a + z_p}\right]^{1/2} \frac{b}{a - z_0} u\left(t + \frac{z_0 - z}{c} - 2\frac{a}{c}\right). \tag{4.32}$$

We can normalize E_3 as

$$\begin{aligned} e_3 = \frac{\pi f_g \ell}{V_0} E_3 &= \frac{\ell}{z_0 - z} \left[\frac{a - z_p}{a + z_p}\right]^{1/2} \frac{b}{a - z_0} u\left(t + \frac{z_0 - z}{c} - 2\frac{a}{c}\right) \\ &= e_\delta' u\left(t + \frac{z_0 - z}{c} - 2\frac{a}{c}\right), \end{aligned} \tag{4.33}$$

$$e_\delta' = \frac{\ell}{z_0 - z} \left[\frac{a - z_p}{a + z_p}\right]^{1/2} \frac{b}{a - z_0}. \qquad 4.34)$$

This result applies for the time up until the signal from the truncation of the aperture is observed.

For convenience we define a retarded time t_r such that $t_r = 0$ is the time of arrival of the direct ray along the z-axis. The field from Ψ_p, the aperture truncation, then arrives at the observer on the *z*-axis in a retarded time

$$\begin{aligned} ct_{r\,\mathrm{end}} &= -r_{2\,\mathrm{end}} + r_3 + [z_0 - z] \\ &= -\left[\Psi_p{}^2 + [z_0 - z_p]^2\right]^{1/2} + \left[\Psi_p{}^2 + [z - z_p]^2\right]^{1/2} + [z_0 - z], \end{aligned} \tag{4.35}$$

where $r_{2\,\mathrm{end}}$ *and* r_3 are illustrated in Figure 4.5. For z near z_0 this is approximately

$$\begin{aligned} r_3 - r_{2\,\mathrm{end}} &= \left[\Psi_p{}^2 + [z - z_p]^2\right]^{1/2} - \left[\Psi_p{}^2 + [z_0 - z_p]^2\right]^{1/2} \\ &= \frac{[z_0 - z_p][z - z_0]}{\left[\Psi_p{}^2 + [z_0 - z_p]^2\right]^{1/2}} + O\left([z - z_0]^2\right), \text{ where} \end{aligned} \tag{4.36}$$

$r_{2\,\mathrm{end}}$ is the r_2 value where $\Psi = \Psi_p$. We can find

$$r_3 - r_{2\,\mathrm{end}} = \left[[z_0 - z_p][z - z_0]\right] \Big/ \left[\Psi_p{}^2 + [z_0 - z_p]^2\right]^{1/2} \tag{4.37}$$

$$\begin{aligned} ct_{r\,\mathrm{end}} &= [z_0 - z]\left[1 - [z_0 - z_p] \Big/ \left[\Psi_p{}^2 + [z_0 - z_p]^2\right]^{1/2}\right] \\ &= [z_0 - z]\left[\left(r_{2\,\mathrm{end}} - z_0 + z_p\right) \Big/ r_{2\,\mathrm{end}}\right]. \end{aligned} \tag{4.38}$$

We notice that e_3 is proportional to $[z - z_0]^{-1}$ and ct_r is proportional to $[z - z_0]$. The product gives the “area” under the pulse as

$$E_{3\,\mathrm{mag}}\, t_{r\,\mathrm{end}} = \frac{V_0}{\pi f_g c}\left[\frac{a - z_p}{a + z_p}\right]^{1/2} \frac{b}{a - z_0}\left(1 - \left(1 + \left(\frac{\Psi_p}{z_0 - z_p}\right)^2\right)^{-1/2}\right). \tag{4.39}$$

This is like an impulse going to zero width as $z \to z_0$. Let us compare this with (5.1) in

[3]. They are exactly the same! This shows that the impulse part of the waveform at the second focus can be described by a delta-like pulse forming for $z < z_0$ and in the limit as $z \to z_0$ gives the required true delta function.

We can find the normalized value of the "area" in (4.39) from (4.33) and (4.38) as

$$e_{3\,\mathrm{mag}}\, t_{r\ \mathrm{end}} = \frac{b\ell}{c(a - z_0)} \left[\frac{a - z_p}{a + z_p} \right]^{1/2} \left[\frac{r_2 - z_0 + z_p}{r_2} \right]. \tag{4.40}$$

4.4.3 Approximate Solution for $z < z_0$ by Aperture Integration for Early Time with z Near z_0

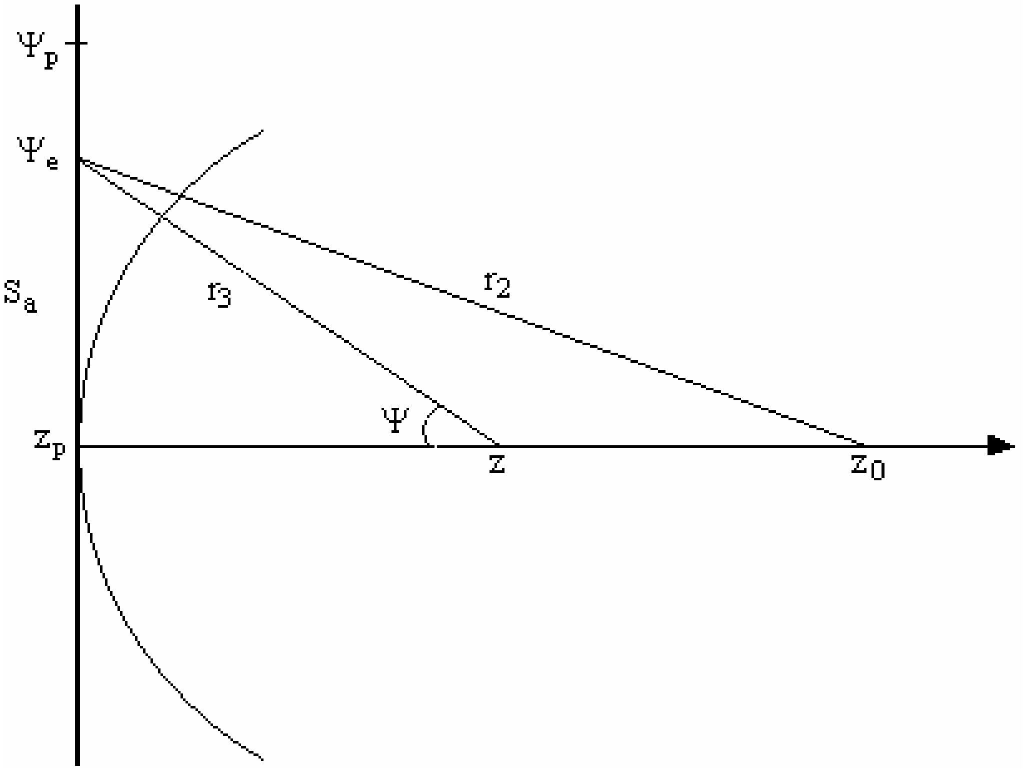

Figure 4.6: Graphical illustration of z values for $z < z_0$ used to calculate the retarded time for the field from $\Psi = \Psi_e$.

An observer at $z \, \vec{1}_z$ can see the field from $\Psi = \Psi_e$ on the aperture at a later retarded time, as illustrated in Figure 4.6

$$
\begin{aligned}
ct_r &= \left[r_3 - \left[z - z_p\right]\right] - \left[r_2 - \left[z_0 - z_p\right]\right] \\
r_3 &= \left[\Psi_e{}^2 + \left[z - z_p\right]^2\right]^{1/2}, \quad r_2 = \left[\Psi_e{}^2 + \left[z_0 - z_p\right]^2\right]^{1/2} \\
ct_r &= \left[\left[\Psi_e{}^2 + \left[z - z_p\right]^2\right]^{1/2} - \left[z - z_p\right]\right] - \left[\left[\Psi_e{}^2 + \left[z_0 - z_p\right]^2\right]^{1/2} - \left[z_0 - z_p\right]\right].
\end{aligned}
\tag{4.41}
$$

For small Ψ_e we have

$$\begin{aligned} ct_r &= \frac{1}{2}\Psi_e^{2}\left[1/(z-z_p)-1/(z_0-z_p)\right] \text{ and} \\ \Psi_e &= \left[2ct_r/\left(1/(z-z_p)-1/(z_0-z_p)\right)\right]^{1/2}. \end{aligned} \tag{4.42}$$

If $|z_0 - z|$ is small we have

$$\begin{aligned} ct_r &= [r_3 - r_2] + z_0 - z, \\ ct_r - [z_0 - z] &= r_3 - r_2, \text{ and} \\ r_3 - r_2 &= \left[\Psi_e^{2} + z^{2}\right]^{1/2} - \left[\Psi_e^{2} + z_0^{2}\right]^{1/2} \\ &\cong \frac{[z_0 + z]}{2}\frac{[z_0 - z]}{\Psi_e^{2} + z_0^{2}}. \end{aligned} \tag{4.43}$$

Thus, we have

$$\begin{aligned} ct_r - [z_0 - z] &\approx +\frac{[z_0 + z]}{2}\frac{[z_0 - z]}{\Psi_e^{2} + z_0^{2}} \text{ and} \\ \Psi_e^{2} &= z_0^{2} + \frac{1}{2}\left((z_0 + z)/\left(\frac{ct_r}{z_0 - z} - 1\right)\right). \end{aligned} \tag{4.44}$$

We want to take the surface integral (4.2 in [3]) to find a new form for E_δ. It does not involve a step-function from S_a. It is now dispersed such that the integration limits can be functions of time, giving

$$\begin{aligned} E_\delta &= \frac{E_0}{\pi c}\frac{d}{dt}\int_0^{\Psi_e}\int_0^{2\pi}\frac{z - z_p}{r_3^{2}}\frac{a + z_0}{r_2 + z_0 + z_p}\left[\frac{z_0 - z_p}{r_2}cos^{2}(\phi) + sin^{2}(\phi)\right]\Psi\, d\theta\, d\Psi \\ &= \frac{E_0}{c}\frac{d}{dt}\int_0^{\Psi_e}\frac{z - z_p}{r_3^{2}}\frac{a + z_0}{r_2}\Psi d\Psi. \end{aligned} \tag{4.45}$$

Let us take the time derivative of the integral

$$E_\delta = \frac{d\Psi_e}{dt}\frac{E_0}{c}\frac{z-z_p}{r_3{}^2}\frac{a+z_0}{r_2}\Psi \; . \tag{4.46}$$

We can find $d\Psi_e / dt$ from (4.44)

$$\frac{d\Psi_e}{c\,dt_r} = \Psi_e{}^{-1}\left(1/\left(z-z_p\right)-1/\left(z_0-z_p\right)\right)^{-1} . \tag{4.47}$$

Thus, (4.45) becomes

$$E_\delta = \Psi_e{}^{-1}\left[1/\left(z-z_p\right)-1/\left(z_0-z_p\right)\right]^{-1}\frac{E_0}{c}\frac{z-z_p}{r_3{}^2}\frac{a+z_0}{r_2}\Psi_e , \tag{4.48}$$

$$E_\delta = \frac{V_0}{\pi f_g}\frac{1}{z_0-z}\left[\frac{a-z_p}{a+z_p}\right]^{1/2}\frac{b}{a-z_0} . \tag{4.49}$$

As we can see it is the same as E_3 in (4.32). This shows that the aperture integral gives the same result (at early time) as the exact incident wave before truncation. This gives confidence in the aperture integration. The reader can note that, since the above gives a pulse width greater than zero, one can add a correction term (zero at zero retarded time) from E_s, also dispersed as E_δ.

4.4.4 Approximate Solution for $z > z_0$ by Aperture Integration for Early time with z Near z_0

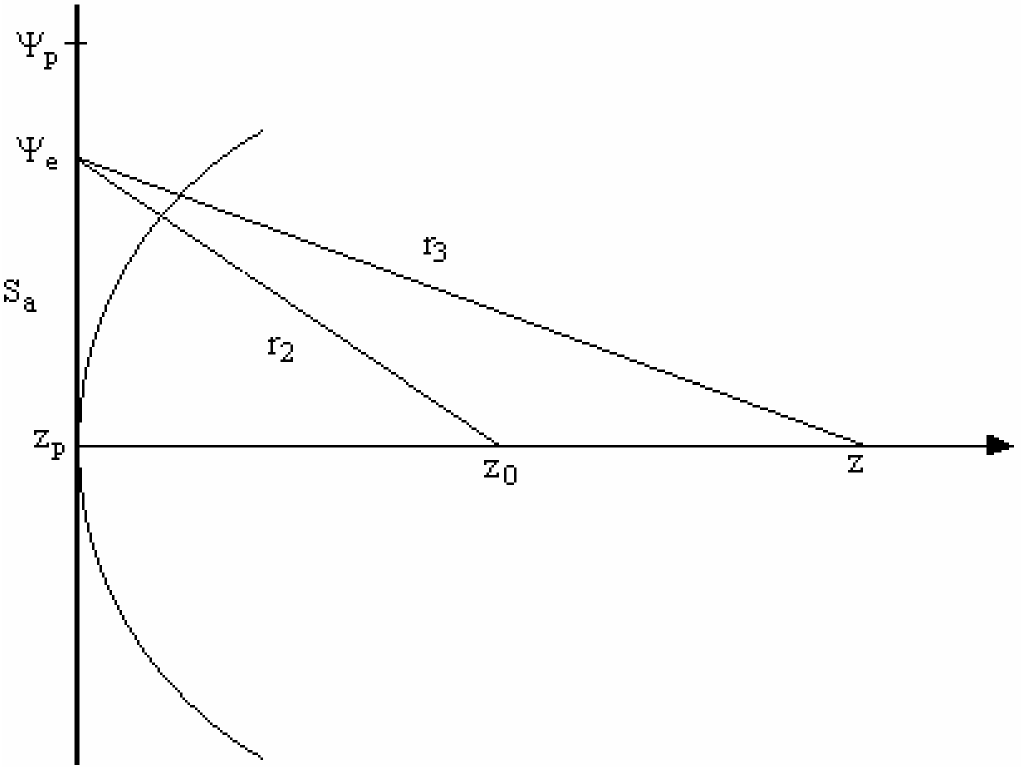

Figure 4.7: Graphical illustration of z values for $z > z_0$ used to calculate the retarded time for the field from $\Psi = \Psi_e$.

Let Ψ_e be close to Ψ_p as shown in Figure 4.7 for which

$$\begin{aligned} r_3 &= \left[\Psi_e{}^2 + \left[z - z_p\right]^2\right]^{1/2} \\ r_2 &= \left[\Psi_e{}^2 + \left[z_0 - z_p\right]^2\right]^{1/2}. \end{aligned} \tag{4.50}$$

The fields arrive on S_a at time

$$ct_{r\,a} = \left[z_0 - z_p\right] - \left[\Psi_e{}^2 + \left[z_0 - z_p\right]^2\right]^{1/2} \tag{4.51}$$

which sets $ct_{r\,a} = 0$ on the aperture center. Fields arrive at z in the retarded time

$$ct_{r\,a} + r_3 \,. \tag{4.52}$$

The first fields at z are from $\Psi = \Psi_p$, in the retarded time

$$ct_{r\,\mathrm{first}} = \left[z_0 - z_p\right] - \left[\Psi_p{}^2 + \left[z_0 - z_p\right]^2\right]^{1/2} + \left[\Psi_p{}^2 + \left[z - z_p\right]^2\right]^{1/2} . \tag{4.53}$$

The last fields come along the z axis in

$$ct_{r\,\mathrm{last}} = \left[z_0 - z_p\right] - \left[z_0 - z_p\right] + z - z_p = z - z_p \,. \tag{4.54}$$

Define a new retarded time by subtracting $z - z_p$; the pulse stops at zero but begins at

$$ct_{r\,\mathrm{begin}} = \left[z - z_p\right] - \left[\Psi_p{}^2 + \left[z_0 - z_p\right]^2\right]^{1/2} + \left[\Psi_p{}^2 + \left[z - z_p\right]^2\right] < 0 \,. \tag{4.55}$$

From an arbitrary point on S_a

$$ct_r = \left[z_0 - z\right] - \left[\Psi^2 + \left[z_0 - z_p\right]^2\right]^{1/2} + \left[\Psi^2 + \left[z - z_p\right]^2\right]^{1/2} . \tag{4.56}$$

We can take the derivative of this retarded time, giving

$$c\frac{dt_r}{d\Psi_e} = -\frac{\Psi_e}{\left[\Psi_e{}^2 + \left[z_0 - z_p\right]^2\right]^{1/2}} + \frac{\Psi_e}{\left[\Psi_e{}^2 + \left[z - z_p\right]^2\right]^{1/2}} , \tag{4.57}$$

$$c\frac{dt_r}{d\Psi_e}\bigg|_{\Psi_e=\Psi_p} = -\frac{\Psi_p}{\left[\Psi_p{}^2+\left[z_0-z_p\right]^2\right]^{1/2}} + \frac{\Psi_p}{\left[\Psi_p{}^2+\left[z-z_p\right]^2\right]^{1/2}}. \tag{4.58}$$

E_δ can be found as,

$$E_\delta = \frac{E_0}{c}\frac{d\Psi_e}{dt}\bigg|_{\Psi_p}\frac{z-z_p}{r_3^2}\frac{a+z_0}{r_2}\Psi_p \quad = \frac{V_0\ell}{\pi f_g\ell}\frac{1}{a-z_0}cot\left(\frac{\theta_c}{2}\right)\frac{d\Psi_e}{dt}\bigg|_{\Psi_p}\frac{z-z_p}{r_3^2}\frac{a+z_0}{r_2}\Psi_p. \tag{4.59}$$

E_δ can be normalized as,

$$e_\delta{}' = \frac{\pi f_g\ell}{V_0}E_\delta = \frac{\ell b}{a-z_0}\left[\frac{a-z_p}{a+z_p}\right]\frac{z-z_p}{r_3}\left[r_3-r_2\right]^{-1}. \tag{4.60}$$

We need to expand $r_3 - r_2$ for small $z - z_0$, yielding

$$\begin{aligned} r_3 &= \left[\Psi_p{}^2+\left[\left[z-z_0\right]+\left[z_0-z_p\right]\right]^2\right]^{1/2} \\ &= \left[\Psi_p{}^2+\left[z_0-z_p\right]^2\right]^{1/2}\left[1+\frac{2\left[z-z_0\right]\left[z_0-z_p\right]+\left[z-z_0\right]}{\left[\Psi_p{}^2+\left[z_0-z_p\right]^2\right]}+O(\left[z-z_0\right])^2\right]^{1/2} \quad , \end{aligned} \tag{4.61}$$

$$r_2 = \left[\Psi_p{}^2+\left[z_0-z_p\right]^2\right]^{1/2}, \tag{4.62}$$

$$r_3 - r_2 = \frac{\left[z-z_0\right]\left[z-z_p\right]}{r_2}, \tag{4.63}$$

as $\Psi_e \to \Psi_p$ and

$$\frac{r_2}{r_3} = 1 + O(\left[z-z_0\right]) \cong 1. \tag{4.64}$$

The normalized field is

$$e_{\delta}' = \frac{\ell b}{a - z_0}\left[\frac{a - z_p}{a + z_p}\right]^{1/2}\frac{1}{z - z_0}. \tag{4.65}$$

This is the same as (4.34). The asymptotic form of $ct_{r\,begin}$ for small $z - z_0$ is

$$\begin{aligned} ct_{r\,begin} &= [z_0 - z]\left[\frac{r_2 - z_0 + z_p}{r_2}\right] \text{ (negative)} \\ &= -ct_{r\,end}. \end{aligned} \tag{4.66}$$

The integral (or area) of the pulse is

$$E_{\delta}\ t_{r\ \text{begin}} = \frac{1}{c}\frac{\ell b}{a - z_0}\left[\frac{a - z_p}{a + z_p}\right]^{1/2}\left[\frac{-r_2 + z_0 - z_p}{r_3}\right]. \tag{4.67}$$

One can see by comparing (4.67) and (4.38), the area of E_{δ} is the same for both z before and after z_0.

4.4.5 Graphical Illustration

In order to illustrate what our results show, let us plot the normalized pulse shape for various $z - z_0$ as one goes from negative values through the second focal point to positive values. For negative values the pulse follows after zero retarded time. For positive values the pulse precedes the zero retarded time. For our example we take the simple case from (4.1), which is related to a 3,4,5 right triangle.

One can see from Figure 4.8 the compression of the pulse as $z \to z_0$ and the expansion of the pulse for $z > z_0$ as z increases away from z_0.

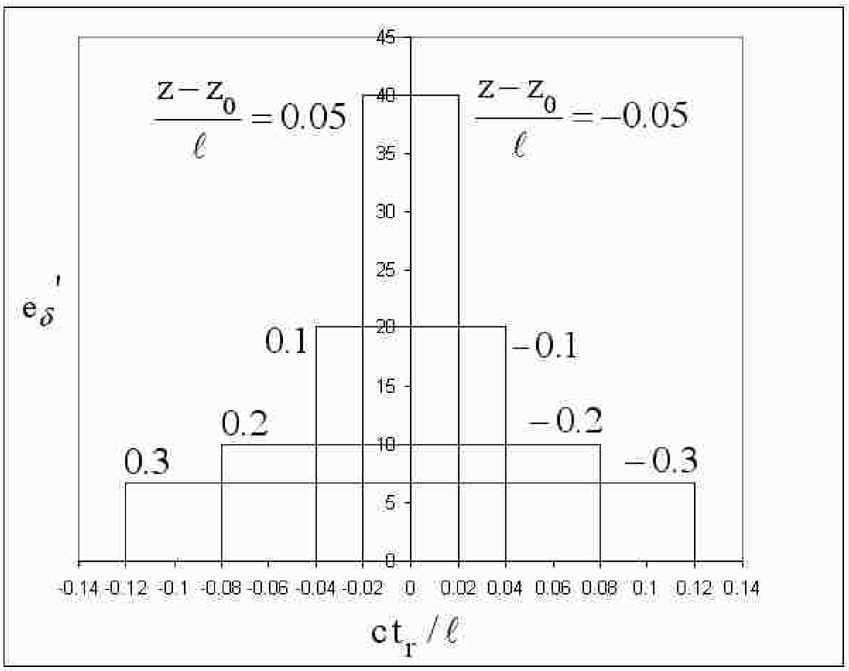

Figure 4.8: Normalized pulse shape for various $\frac{z - z_0}{\ell}$ to demonstrate the compression and expansion of the pulse.

4.5 Analytical Focal Waveforms for Various Source Waveforms Driving a Prolate- Spheroidal IRA

This section considers the time domain characteristics of some analytic source waveforms used for determining the waveform characteristic of a prolate-spheroidal IRA at the second focus. This is an analytical calculation of a prolate-spheroidal IRA that is based on [3,5,17,19]. The analytical waveforms for 2-TEM-feed-arm, 45^o 4-TEM-feed-arm and 60^o 4-TEM-feed-arm cases at the second focus are calculated. We analyze the analytical focal waveform behavior for two different source waveforms.

4.5.1 Double Exponential Excitation (DEE)

Let us use the commonly used waveform which is the difference between two exponentials times a unit step function instead of a unit step function. Our excitation is

$$\begin{aligned} &V(t) = V_0\, f(t)\ ,\ \ f(t) = \left[e^{-\beta t} - e^{-\alpha t}\right]\ u(t), \\ &\alpha = {t_\delta}^{-1},\ t_\delta = 100\, ps\ ,\ 50\, ps, \quad \beta = {t_d}^{-1},\ t_d = 1\, ns,\ 2\, ns, \end{aligned} \tag{4.68}$$

where t_δ is the rise and t_d is the decay time constant. The peak of the waveform is given by (2.14) in [20] as

$$\begin{aligned} &f_{max} = \frac{max}{t}\left(f(t)\right) = \zeta^{\frac{1}{1-\zeta}}\left[\frac{1}{\zeta} - 1\right] = f(t_{max}), \\ &\zeta = \beta / \alpha, \end{aligned} \tag{4.69}$$

where $t_{\max}$ is the time when the maximum occurs and can be found by taking the derivative of (4.68)

$$t_{\max} = \frac{1}{\alpha - \beta} ln\left(\frac{\alpha}{\beta}\right). \tag{4.70}$$

We present the $f(t)/f_{\max}$ values for different α *and* β in Figure 4.9. $f_{\max}$ and the $t_{\max}$ values for different α *and* β are presented in Table 4.3

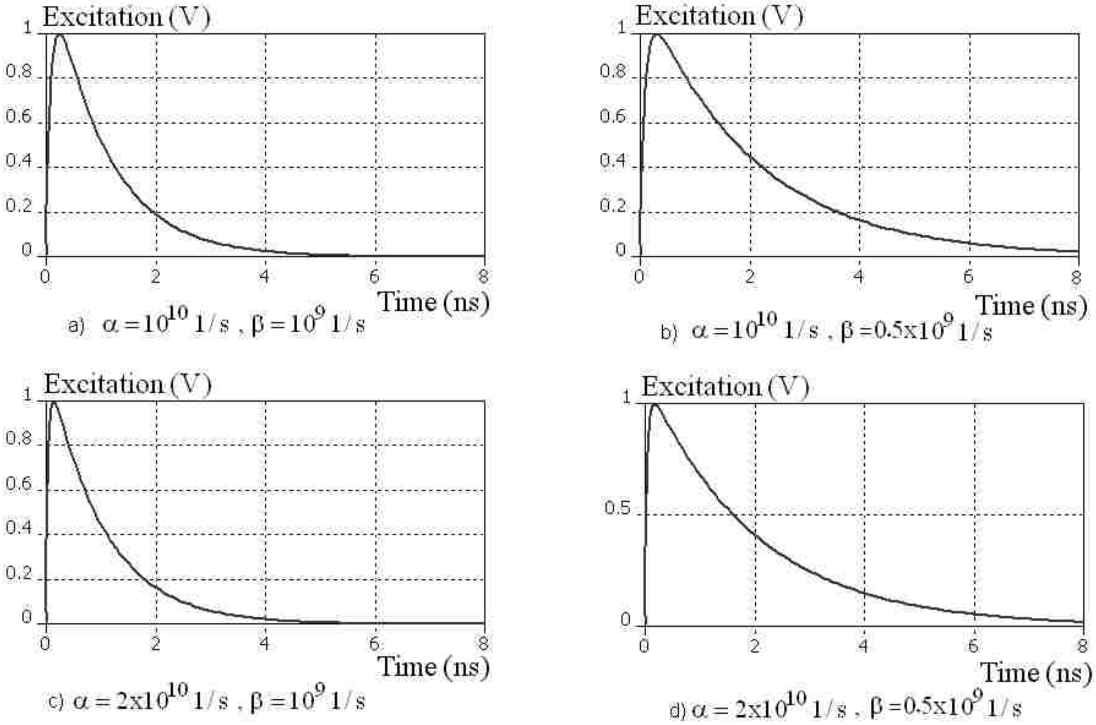

a) $\alpha = 10^{10}$ 1/s , $\beta = 10^{9}$ 1/s

b) $\alpha = 10^{10}$ 1/s , $\beta = 0.5\text{x}10^{9}$ 1/s

c) $\alpha = 2\text{x}10^{10}$ 1/s , $\beta = 10^{9}$ 1/s

d) $\alpha = 2\text{x}10^{10}$ 1/s , $\beta = 0.5\text{x}10^{9}$ 1/s

Figure 4.9: Double exponential excitation for $f(t)/f_{\max}$ for different α and β.

Table 4.3: $f_{\max}$ and $t_{\max}$ values for different α and β.

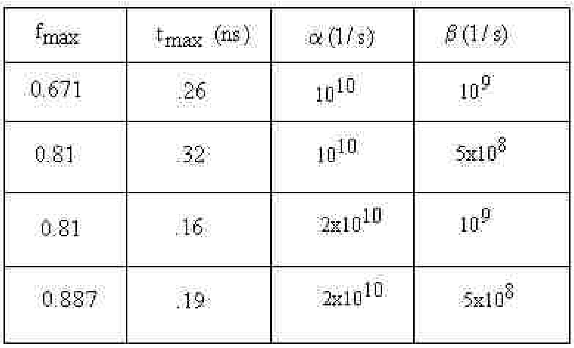

$f_{\max}$	$t_{\max}$ (ns)	α (1/s)	β (1/s)
0.671	.26	10^{10}	10^{9}
0.81	.32	10^{10}	$5\text{x}10^{8}$
0.81	.16	$2\text{x}10^{10}$	10^{9}
0.887	.19	$2\text{x}10^{10}$	$5\text{x}10^{8}$

4.5.2 Analytical Focal Waveforms

The analytical focal waveforms for ramp rising step excitation are from [16]. The excitation is a 1 Volt $(\mathrm{V}_0 = .5\ \mathrm{Volt})$ step, rising as a ramp function lasting 100 ps. One can see the ramp rising step excitation in Figure 4.10 and the focal waveforms for this excitation in Figure 4.11.

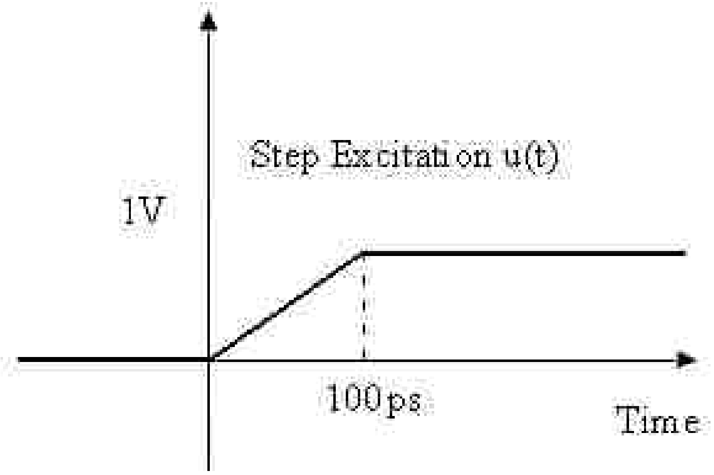

Figure 4.10: Ramp rising step excitation u(t).

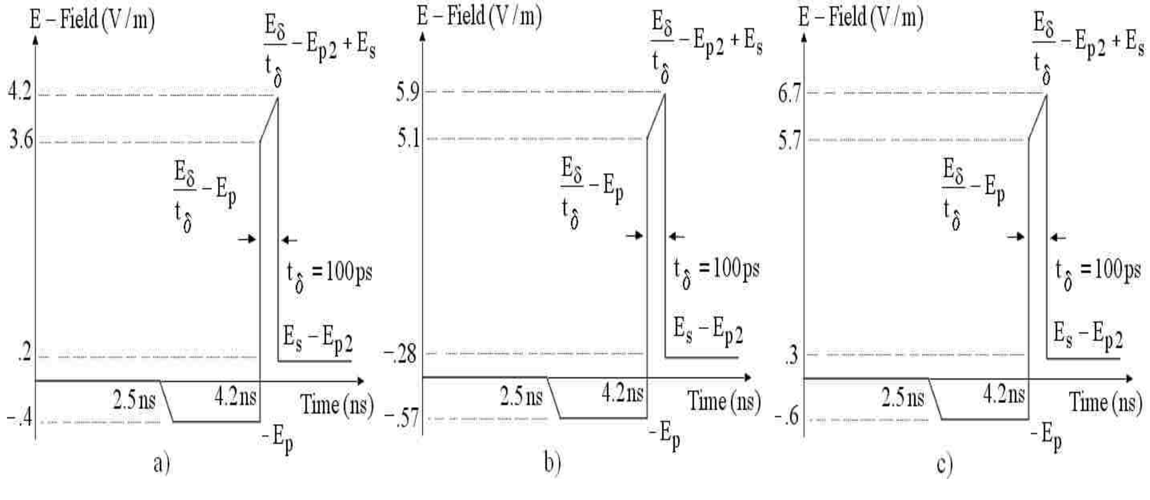

Figure 4.11: Analytical focal waveforms for ramp rising step excitation
a) two-arm 400 Ω b) 45^{o} four-arm 200 Ω c) 60^{o} four-arm 200 Ω.

From a step excitation u(t) we obtain a focal waveform as in Figure 4.12.

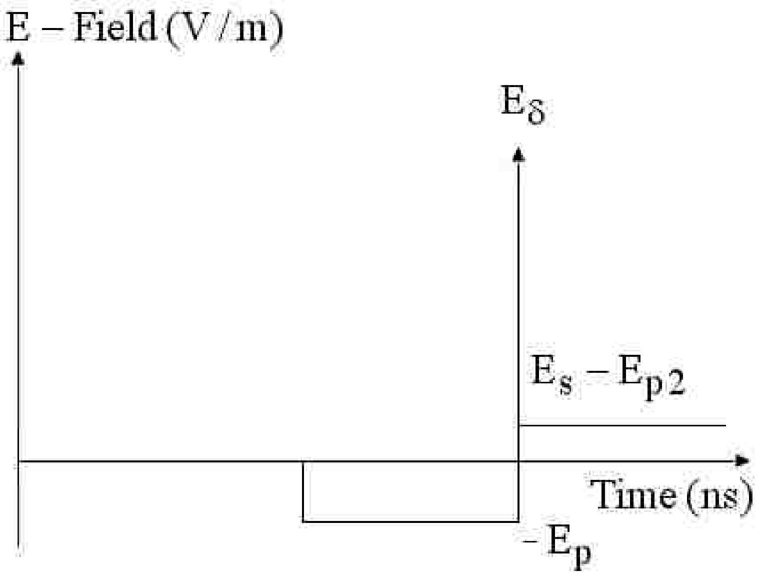

Figure 4.12: Step response of a prolate-spheroidal IRA at the second focal point.

Considering the decomposition of the focal waveform, the prepulse, impulse and postpulse can be presented separately as in Figure 4.13.

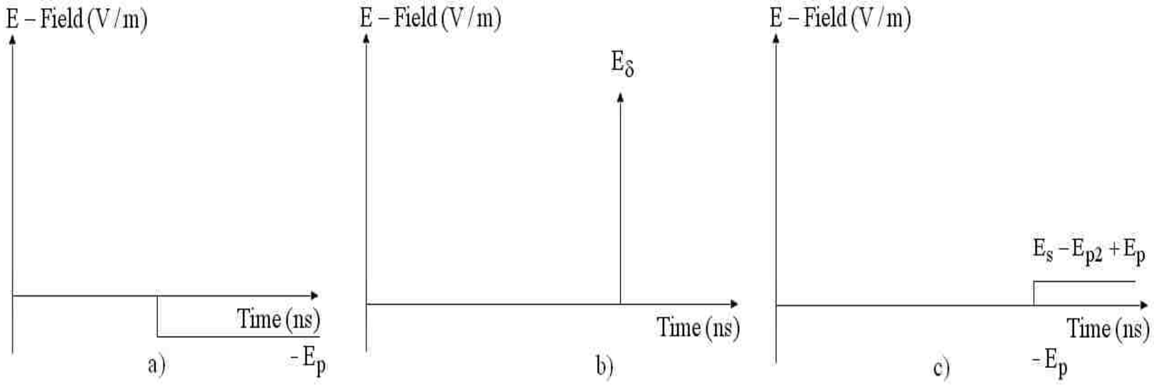

Figure 4.13: Decomposition of step response of Figure 4.12 a)prepulse, b)impulse, c)postpulse.

If we use the double exponential excitation function (4.67) instead of a step function, we will have a response as in Figure 4.14.

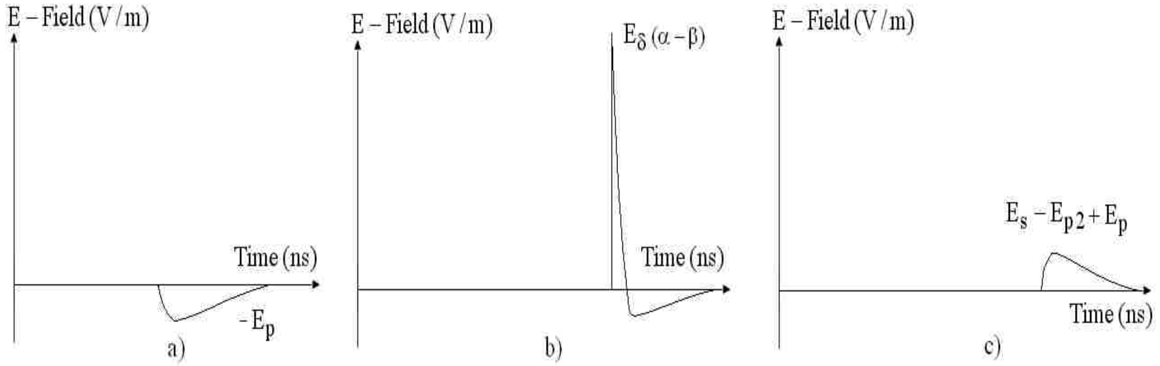

Figure 4.14: Decomposition of DEE response a)prepulse, b)impulse, c)postpulse.

One can see from Figures 4.13 and 4.14 that if we use a DEE instead of a step excitation we have a decrease in the amplitude of the prepulse, an increase in the amplitude of the impulse and postpulse goes to zero.

The impulse part of the double exponential excitation can be defined as

$$\frac{E_\delta}{f_{\max}}\frac{dV(t-t_2)}{dt}=\frac{E_\delta}{f_{\max}}\left[-\beta e^{-\beta(t-t_2)}+\alpha e^{-\alpha(t-t_2)}\right]u(t-t_2) \qquad (4.71)$$

and the peak value is $E_\delta(\alpha-\beta)$, where $t_2 = 4.2\,ns$ is the time when the impulse arrives at the second focus. Finally, we obtain response waveforms from (4.68) in Figure 4.15, where $E_{p\delta}$ is the value of E_p at the time the impulse starts

$$E_{p\delta} = \frac{E_p}{f_{max}} \left[e^{-\beta(t_2 - t_1)} - e^{-\alpha(t_2 - t_1)} \right] \tag{4.72}$$

where $t_1 = 2.5\ ns$ is the time that prepulse arrives at the second focus. The calculated $E_{p\delta}$ values for different α and β are presented in Table 4.4. 45^o four-arm 200 Ω and 60^o four-arm 200 Ω case are just $\sqrt{2}$ *and* 1.606 times these waveforms, as discussed in Chapter 3.

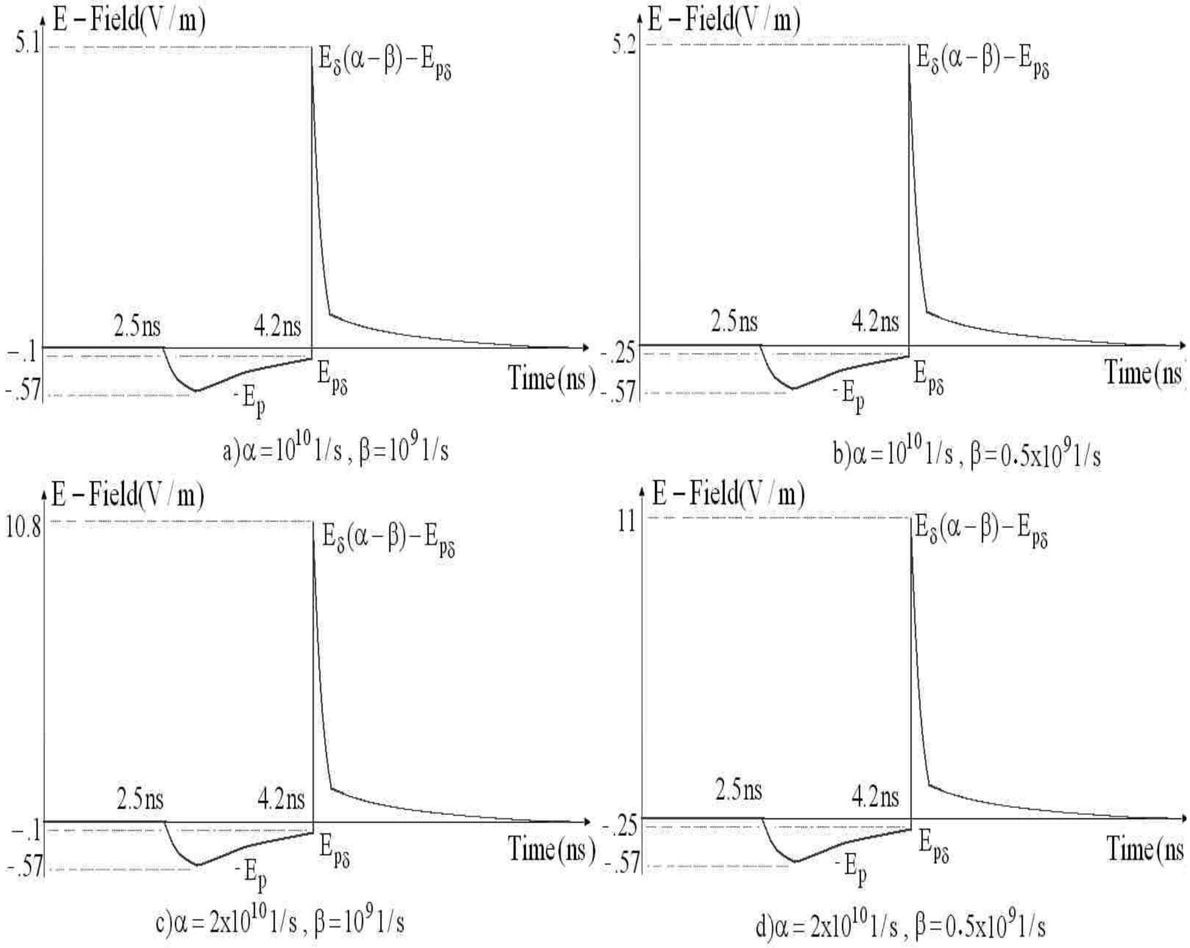

a) $\alpha = 10^{10}\ 1/s$, $\beta = 10^9\ 1/s$

b) $\alpha = 10^{10}\ 1/s$, $\beta = 0.5x10^9\ 1/s$

c) $\alpha = 2x10^{10}\ 1/s$, $\beta = 10^9\ 1/s$

d) $\alpha = 2x10^{10}\ 1/s$, $\beta = 0.5x10^9\ 1/s$

Figure 4.15: Double exponential excitation responses for different α and β.

Table 4.4: The prepulse, $E_{p\delta}$, values for different α and β .

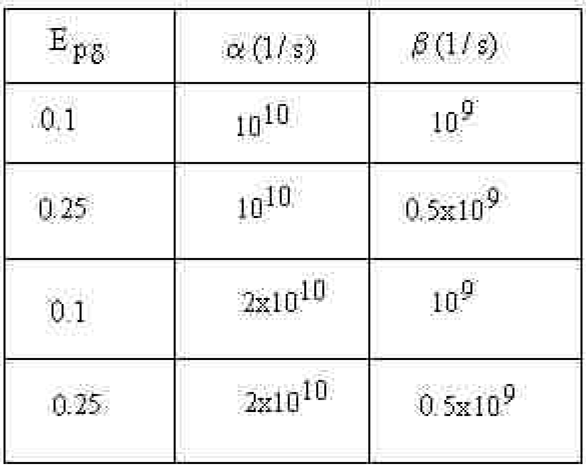

$E_{p\delta}$	$\alpha (1/s)$	$\beta (1/s)$
0.1	10^{10}	10^{9}
0.25	10^{10}	$0.5x10^{9}$
0.1	$2x10^{10}$	10^{9}
0.25	$2x10^{10}$	$0.5x10^{9}$

4.5.3 Conclusion for Ramp-Rising Excitation and DEE

We obtain higher impulse values for the double exponential excitation because the prepulse value $E_{p\delta}$ is less than the regular E_p value that we have from the step excitation at the time that the impulse arrives. One can see in Figure 4.11b) that we have a decrease from $-0.57\,\mathrm{V/m}$ to $-0.1\,\mathrm{V/m}$, an 82% decrease. If we compare $E_{p\delta}$ with the E_p value for step excitation with Figure 4.11a), we have a decrease from $-0.4\,\mathrm{V/m}$ to $-0.1\,\mathrm{V/m}$, a 75% decrease. If we look at the impulse for step and double exponential excitation and compare Figure 4.11a) with Figure 4.15a), one can see that we have an increase from $4.2\,\mathrm{V/m}$ to $5.1\,\mathrm{V/m}$, a 22% increase in the peak focal field. The postpulse also decays toward zero. This type of waveform is convenient because of its simplicity and it may better model the pulser output.

4.6 Analytical Errors

Analytical errors can be classified into two groups. First of all, the analytical calculation does not account for feed arm width, and it is a little different from [5]. Secondly, when calculating the aperture integrals, we have used the uniform-field part all the way to $\Psi = \Psi_p$ but the feed arms intersect partly into S_a for $\Psi < \Psi_p$. The aperture integrals are correct up to some radius less than Ψ_p. Note that the 60^0 arms are much wider than the 45^0 arms for the same $200\ \Omega$ impedance. The analytical waveform, while simple, is still good, but not perfect.

5 NUMERICAL SIMULATIONS

5.1 Introduction

This chapter presents computational electromagnetics results to compare with the analytical results for the waveform from a prolate-spheroidal IRA. The numerical results for the waveforms near the second focus are discussed for spot size analysis.

We use CST MICROWAVE STUDIO (CST MWS) for the 3D Electromagnetic simulation. CST MWS is based on the finite integration technique (FIT). This numerical method provides a universal spatial discretization scheme, applicable to various electromagnetic problems ranging from static field calculations to high frequency applications in time or frequency domain. CST MWS applications include the expanding areas of: Mobile Communication, Wireless Design, Signal Integrity, and EMC. The broadly applicable time domain solver and the frequency domain solver simulate on hexahedral as well as on tetrahedral grids [21].

We are dealing with a computationally difficult problem that causes inaccurate results in our numerical simulations. We want greater concentration of energy at the second focus; for this reason we plan to use a medium that has a higher relative dielectric constant ε_r placed nearby the target. This also increases the complexity of our problem; however, our experimental results show that the wave propagation medium which has the highest ε_r (in our case it is water with $\varepsilon_r = 81$ [1]) is dispersive.

In this chapter we describe simulation results of two-arm $400\ \Omega$, 45^o four-arm $200\ \Omega$, and 60^o four-arm $200\ \Omega$ prolate-spheroidal IRAs to obtain the focal waveforms. The spot size is analyzed for the two-arm case, along the *x-, y-* and *z*-axis.

We compare our numerical results with analytical results. For future work, we present an equivalent geometry that can be used as an equivalent source to simplify the problem.

5.2 Comparison of Analytical and Numerical Focal Waveforms for a Prolate-Spheroidal IRA

This section presents the numerical and analytical results for the focal waveform from a prolate-spheroidal IRA. Both numerical and analytical calculations are discussed for IRAs with different feed arms. In both cases the comparisons between the numerical and analytical results are presented and discussed.

Analytical focal waveforms for ramp rising step excitation for two-arm $400\ \Omega$, 45^o four-arm $200\ \Omega$ and 60^o four-arm $200\ \Omega$ were presented in Figure 4.10. We want to compare the numerical focal waveforms with analytical focal waveforms for each case. One can see the comparison of the focal waveforms and zoom in on the impulse for analytical and numerical focal waveforms in Figures 5.1-5.3.

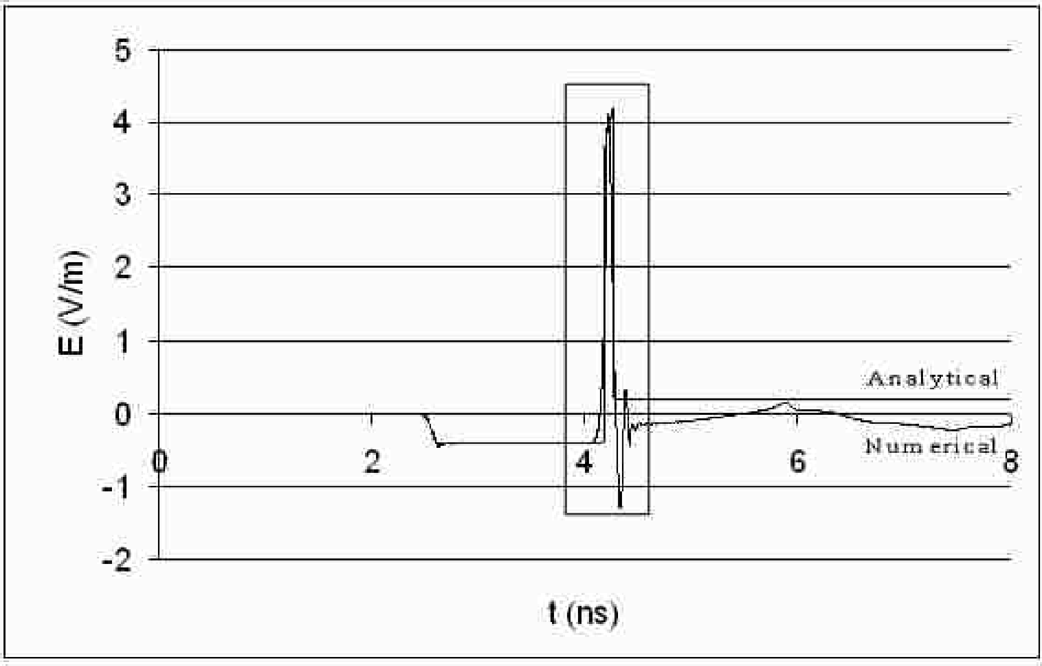

a)

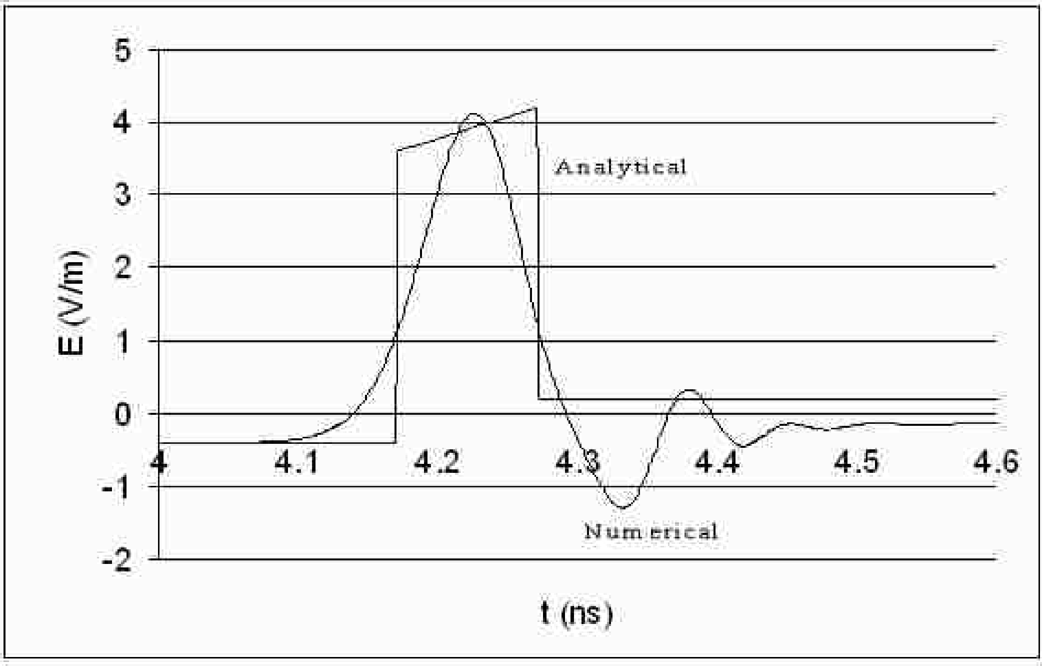

b)

Figure 5.1: Focal waveforms for the two-arm case: a)analytical and numerical, b)expanding the impulse.

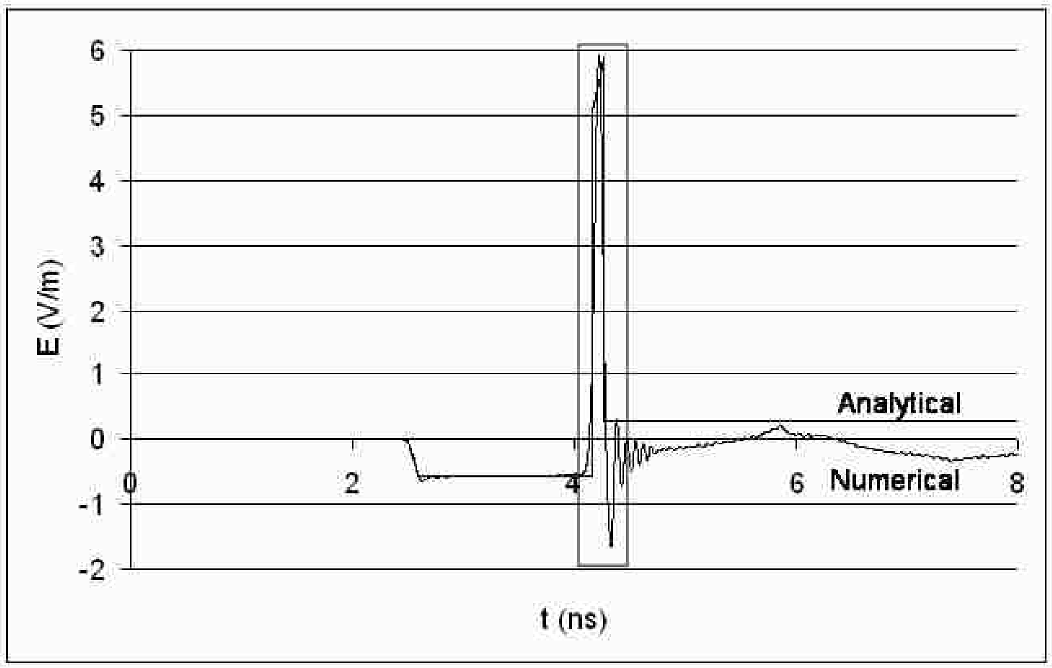

a)

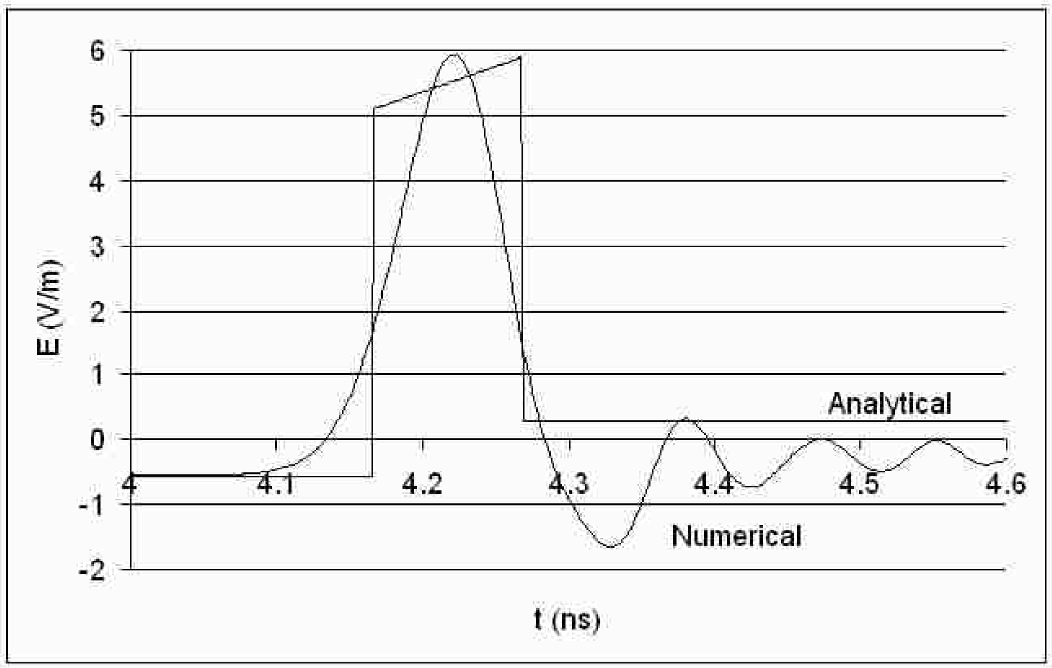

b)

Figure 5.2: Focal waveforms for 45^o four-arm case: a)analytical and numerical, b) expanding the impulse.

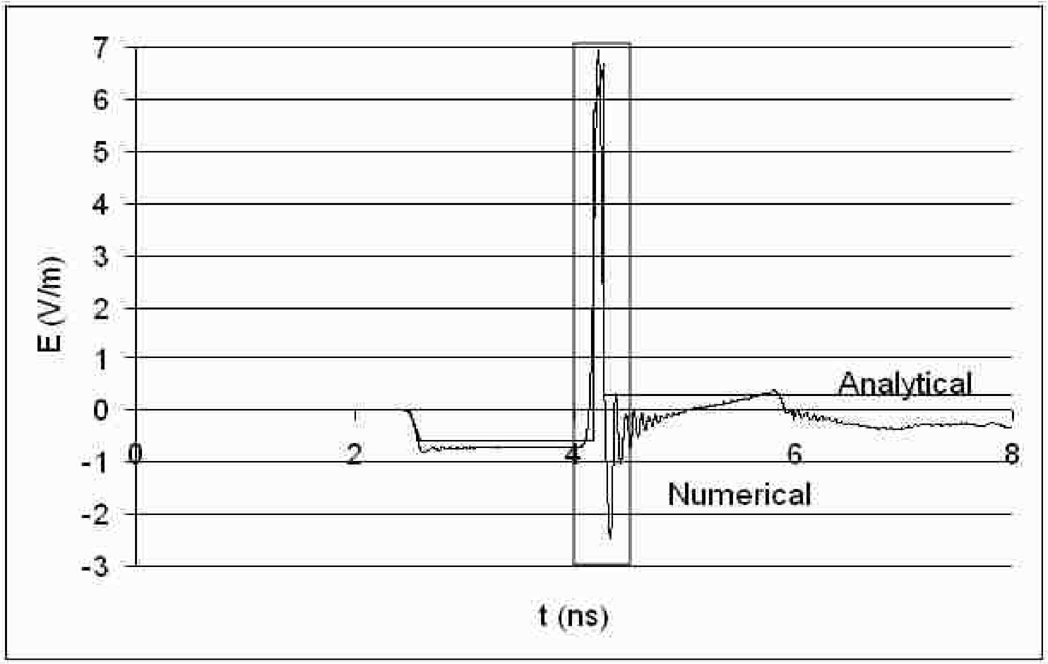

a)

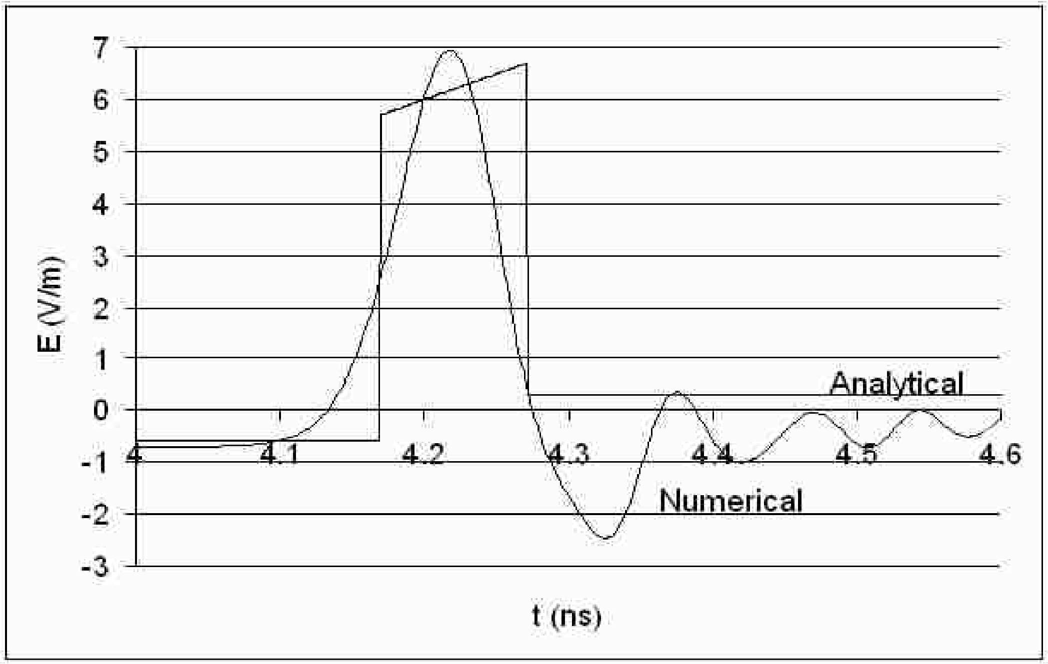

b)

Figure 5.3: Focal waveforms for 60^o four-arm case: a)analytical and numerical, b)expanding the impulse.

The excitation is a 1 Volt $(V_0 = .5 \text{ Volt})$ step, rising as a ramp function lasting 100 ps. Comparing the analytical results with the numerical results, one can see the differences in the postpulse. The prepulse comparison is rather good and the impulse is trying to approach the analytical shape and value, but the postpulse has no relation to the analytical result.

For the two-arm and 45° four-arm cases the prepulse of –0.4 V/m and -0.6 V/m agree very closely between the analytical and numerical cases. For the 60° four-arm case the analytic prepulse is -0.6 while the numerical case is -0.7 (some error). The impulse part shows great agreement between analytical and numerical, approaching the analytical value from below, likely due to the high-frequencies which are truncated from the numerical solutions.

We have ringing in the postpulse and a detailed discussion on the postpulse ringing for the experimental results is presented in Chapter 6. The analytical waveform, while simple, is still good, but not perfect. The analytical errors that were discussed in section 4.7 may cause this inconsistency. In our analytical calculations we assume we have infinitely thin feed arms and reflector, but CST MWS does not allow this. One source of this ringing is the feed. In CST MWS a voltage source was used for excitation and we have a 0.5 cm distance between the feed arms; however, in our analytical calculations we do not account for this. The numerical computations may be inadequate, perhaps due to mesh size and frequency limitation.

5.3 Numerical Focal Waveforms for Various Source Waveforms Driving a Prolate-Spheroidal IRA

5.3.1 Numerical Focal Waveform with Smoother Rise for Excitation

The discontinuity in the ramp-rising step excitation can cause oscillations in the postpulse and a smoother waveform can be used to check this. The smoother waveform has the same t_{mr} (based on maximum rate of rise) with the ramp-rising step (normal) waveform. For a step like $f(t)$, the t_{mr} is

$$t_{mr} = \frac{f_{max}}{\left.\frac{df}{dt}\right|_{max}} . \tag{5.1}$$

We have the same t_{mr} but no discontinuities in the slope (derivative) to reduce the required high frequencies. We use an arbitrary waveform that is smoother and is presented in Figure 5.4 and can be defined as

$$f(t) = \left(1 - cos(2t / t_{\delta})\right) / 2 . \tag{5.2}$$

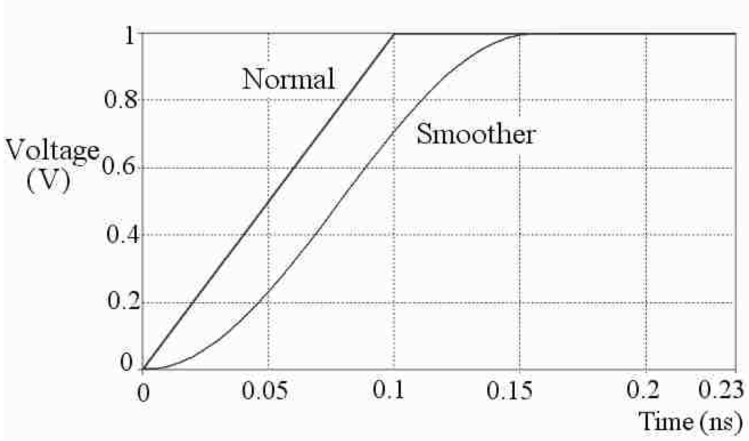

Figure 5.4: Ramp-rising (normal) and smoother excitation functions.

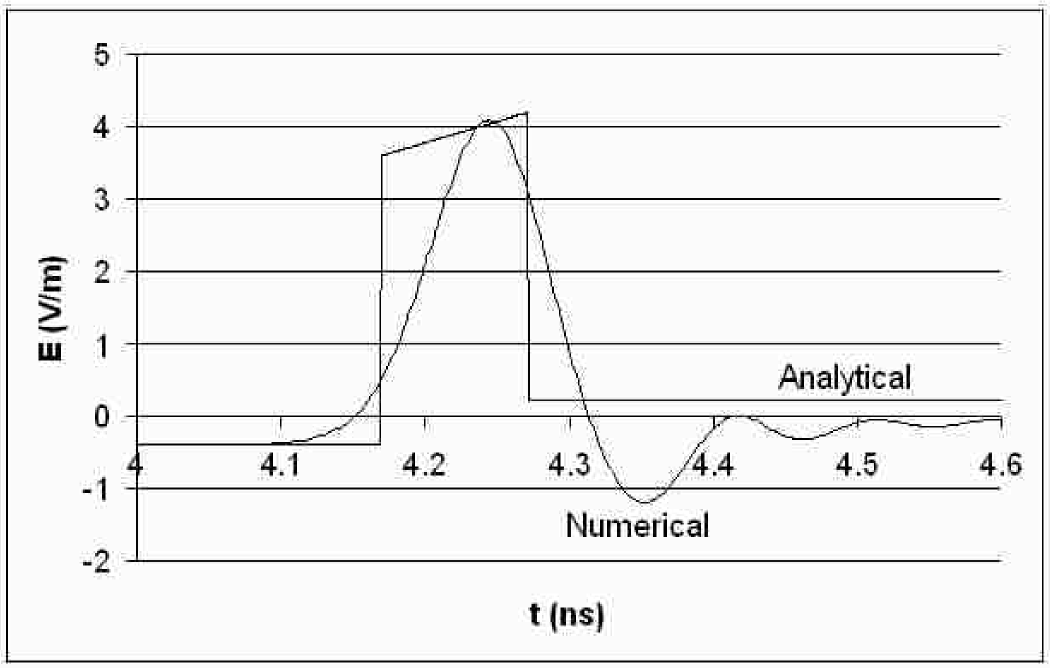

a)

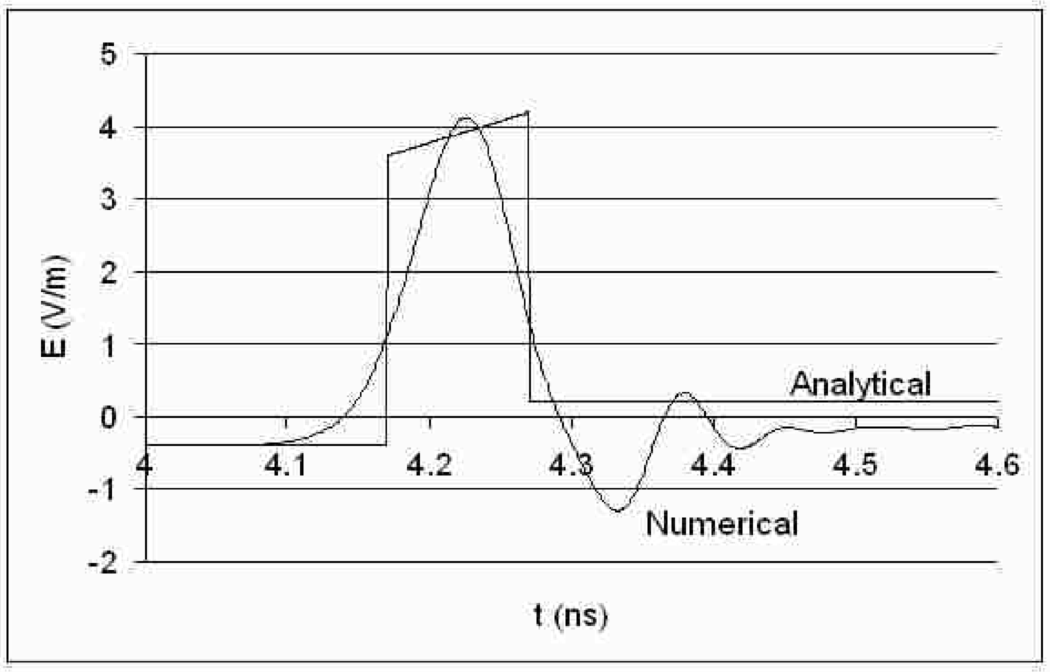

b)

Figure 5.5: Analytical and numerical waveform for a)smoother, b)ramp step excitation.

One can see by comparing Figure 5.5 a and b that we still have oscillations in the prepulse, but we have smaller late-time oscillation amplitude.

5.3.2 Numerical Focal Waveforms for Double-Exponential Excitation Waveforms Driving a Prolate-Spheroidal IRA

The detailed analytical calculations for the DEE were discussed in section 4.6. This subsection considers the time domain characteristics of the numerical waveform of a prolate-spheroidal IRA near the second focus when it is driven by a double-exponential excitation.

We use double-exponential excitation waveforms to drive our prolate-spheroidal IRA where $t_\delta = 100\,ps$, $t_d = 1\,ns$, t_δ is the rise, and t_d is the decay time. DEE analytical responses for $t_\delta = 100\ ps,\ \ t_d = 1\,ns$ two arm, 45^{o} four arm and 60^{o} four arm are presented in Figure 5.6.

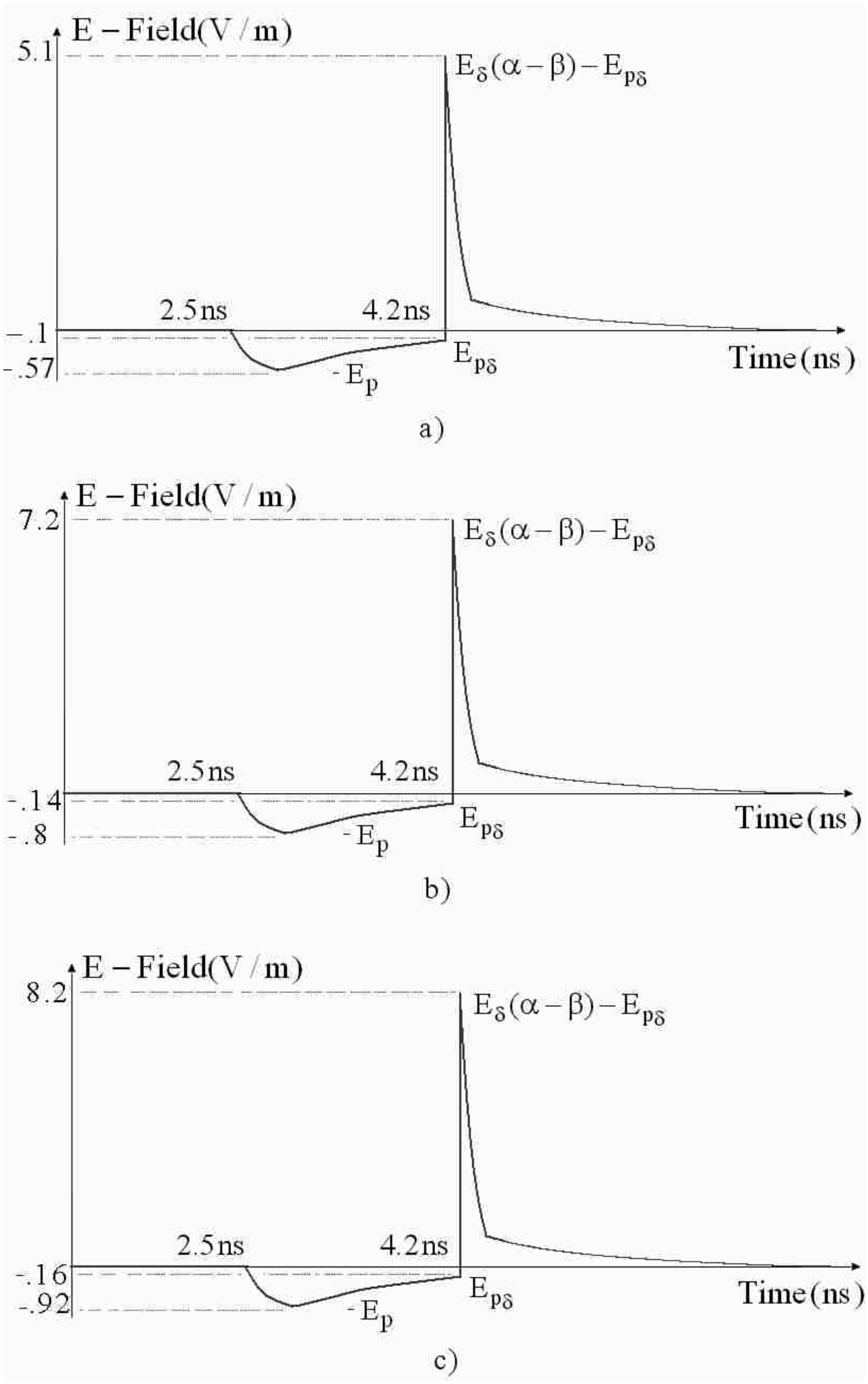

Figure 5.6: DEE analytical responses for $t_\delta = 100$ ps, $t_d = 1ns$ a) two arm, b) 45^o four arm, c) 60^o four arm.

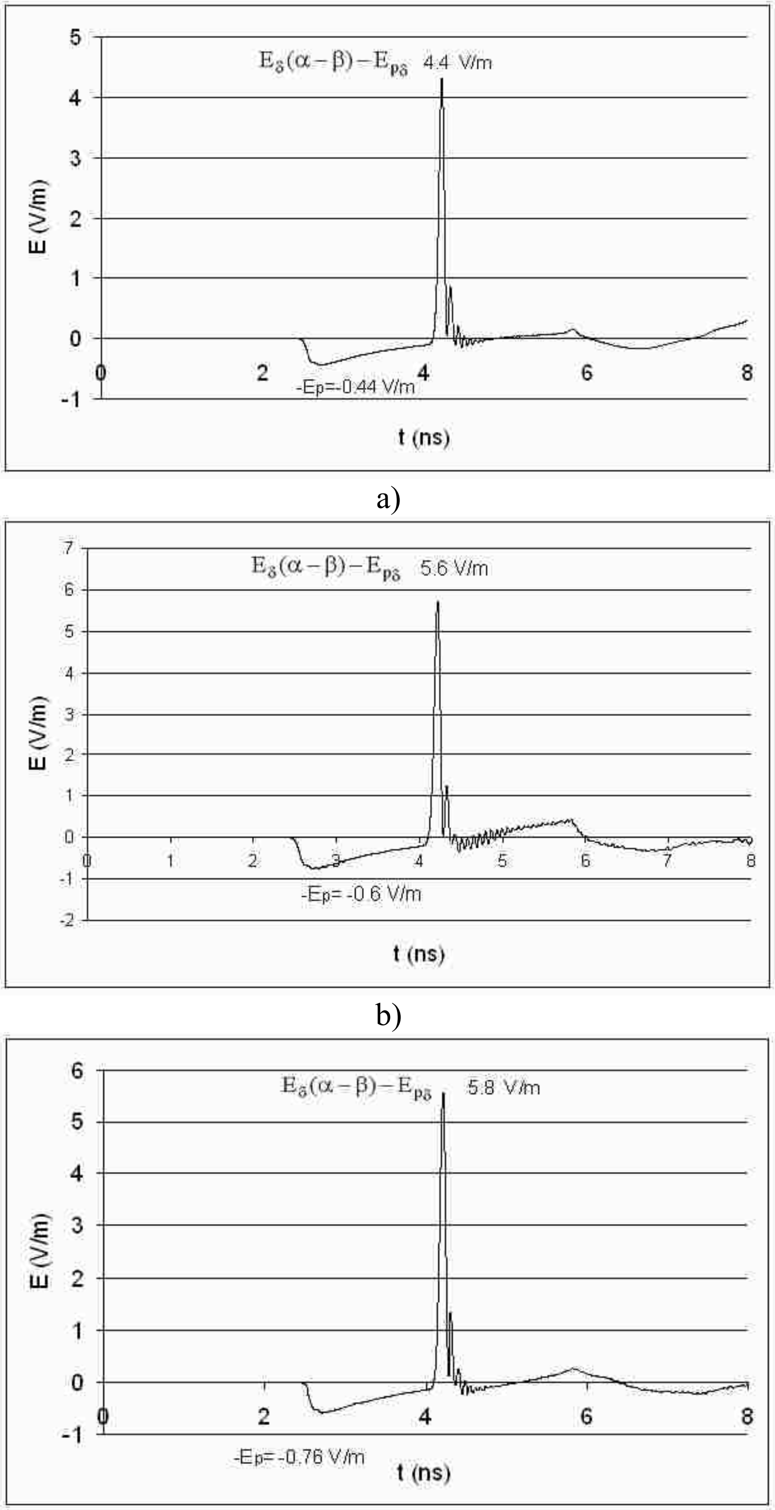

a)

b)

c)

Figure 5.7: DEE numerical responses for $t_\delta = 100\,\text{ps}$, $t_d = 1\,ns$ a) two arm, b) 45^o four arms, c) 60^o four arms.

DEE numerical focal waveforms are presented in Figure 5.7. If we compare Figures 5.6 and 5.7 we obtain numerical waveforms which are really close to the analytical waveforms. However, we have lower prepulse and impulse amplitude, and these inconsistencies are based on the limitations of the idealized analytical assumptions and numerical errors.

5.4 Numerical Calculation for the Waveforms Near the Second Focus of a Prolate-Spheroidal IRA

This section discusses the numerical results for the waveforms near the second focus of a prolate-spheroidal IRA. Both numerical and analytical calculations are for IRAs with different feed arms. Variations of the waveforms for *x*, *y* and *z*-axis variations near the second focus are found for two-TEM-feed-arm IRAs.

Given that the impulse has some small pulse width $t_\delta = 100\,\mathrm{ps}$, the maximum fields will exist in some small region around z_0. We can make a rough estimate of spot size [3] as follows. The pulse width is used to define the spot boundary with respect to Ψ and z:

$$t_\Psi = t_z = 2t_\delta = 200\,ps\,. \tag{5.3}$$

Therefore, the spot size from (A.23) are

$$\begin{aligned} |\Delta z| &= 2\,[1 - z_0 / a]^{-1} ct_\delta = 15\,cm\,, \\ \Delta\Psi &= \frac{a}{b} ct_\delta = 3.75\,cm\,. \end{aligned} \tag{5.4}$$

5.4.1 Numerical Waveforms for Two-Feed Arms

$x = 0$ is one of the symmetry planes of our design. One can see from Figure 5.8 that at $x = \pm 4cm$ the waveform begins to disperse as expected from (5.4), $y = 0$ is also one of the symmetry planes of our design. The dispersion starts at $y = \pm 4cm$ from Figure 5.9. If we compare the waveform for $x = \pm 4cm$ and $y = \pm 4cm$, we can see that we have a larger amplitude for *x*- axis variation. This is expected because if we move along the y-axis we are moving away from the feed arms. But for the x-axis we are getting closer to one of the feed arms while we are getting farther away from the other one.

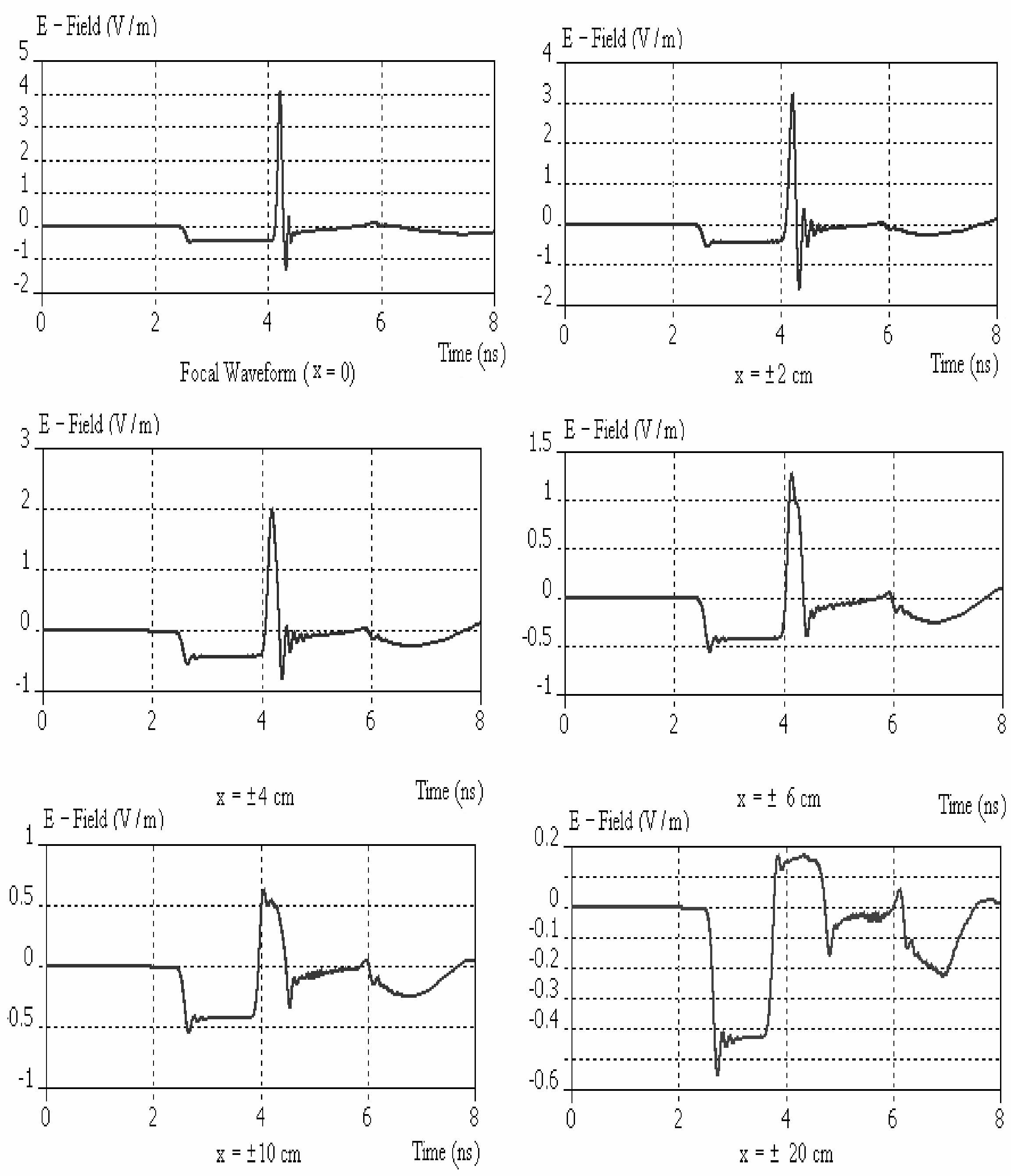

Figure 5.8: Numerical waveforms for various *x*-axis variations.

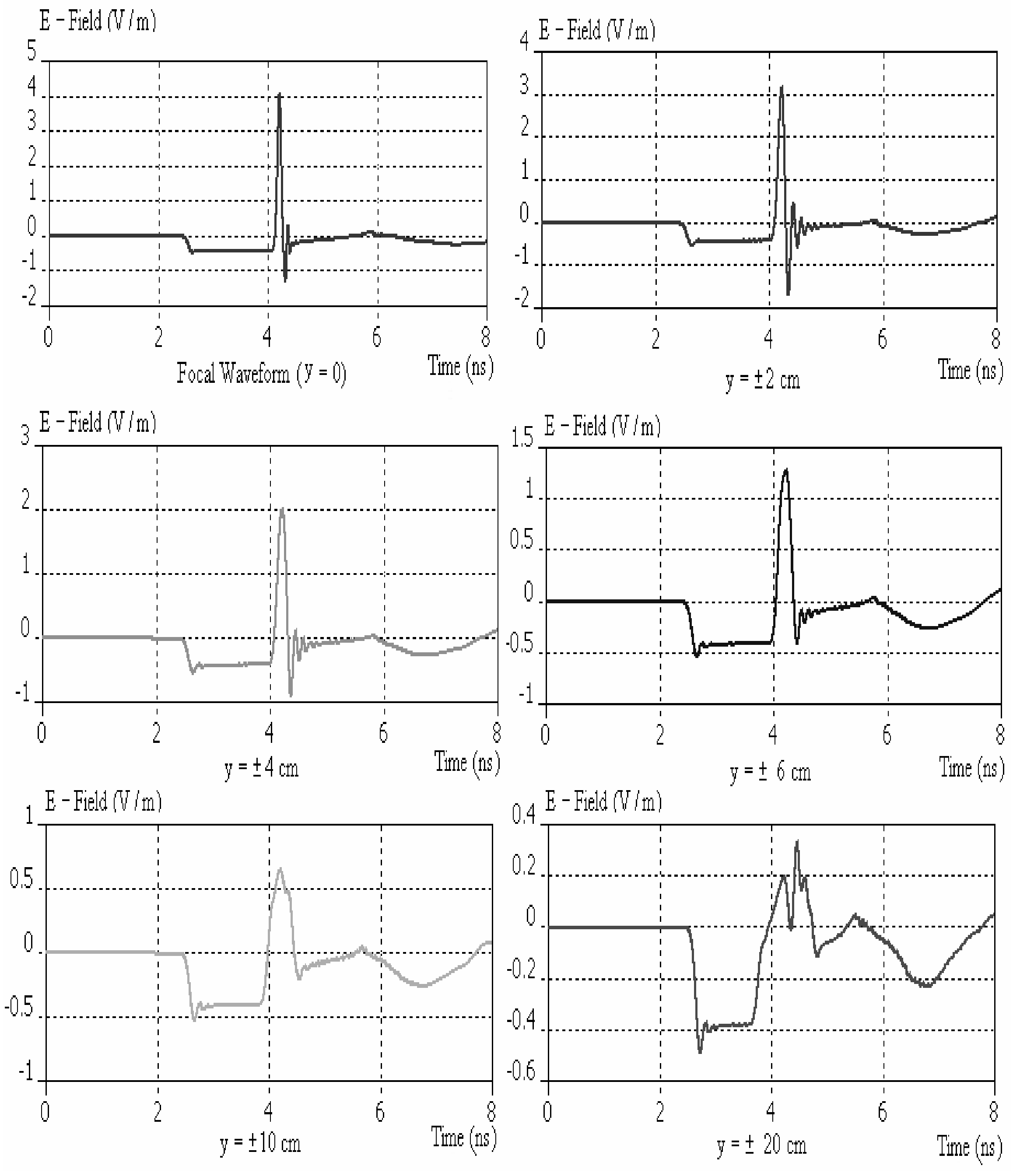

Figure 5.9: Numerical waveforms for various y-axis variations for 2-TEM-feed-arms.

Figure 5.10 presents the electric field vectors for different rays. One can see from Figure 5.11 the waveforms are not symmetric with respect to the $z = z_0$ plane (which is not a symmetry plane). We have competing factors. As we move away from S_a this gives lower fields due to the inverse distance scaling in the integrals. However, the wave from S_a is not oriented in the x-direction, but is tilted, this being more evident the closer you are to S_a.

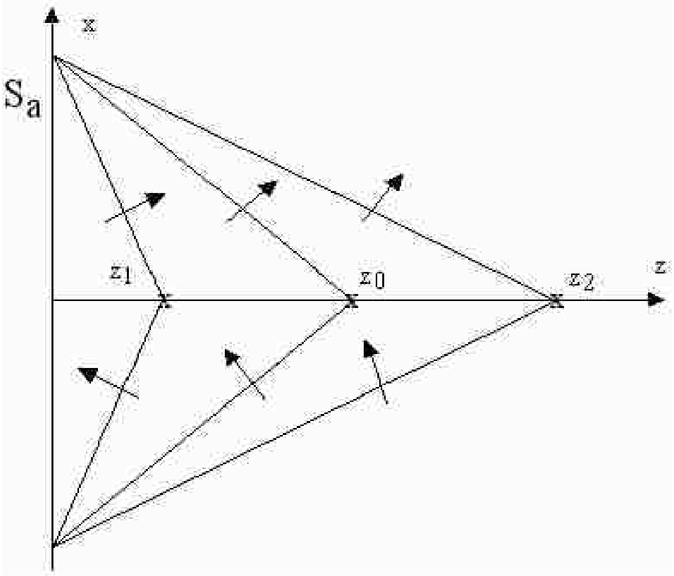

Figure 5.10: Depiction of electric field vectors for different rays.

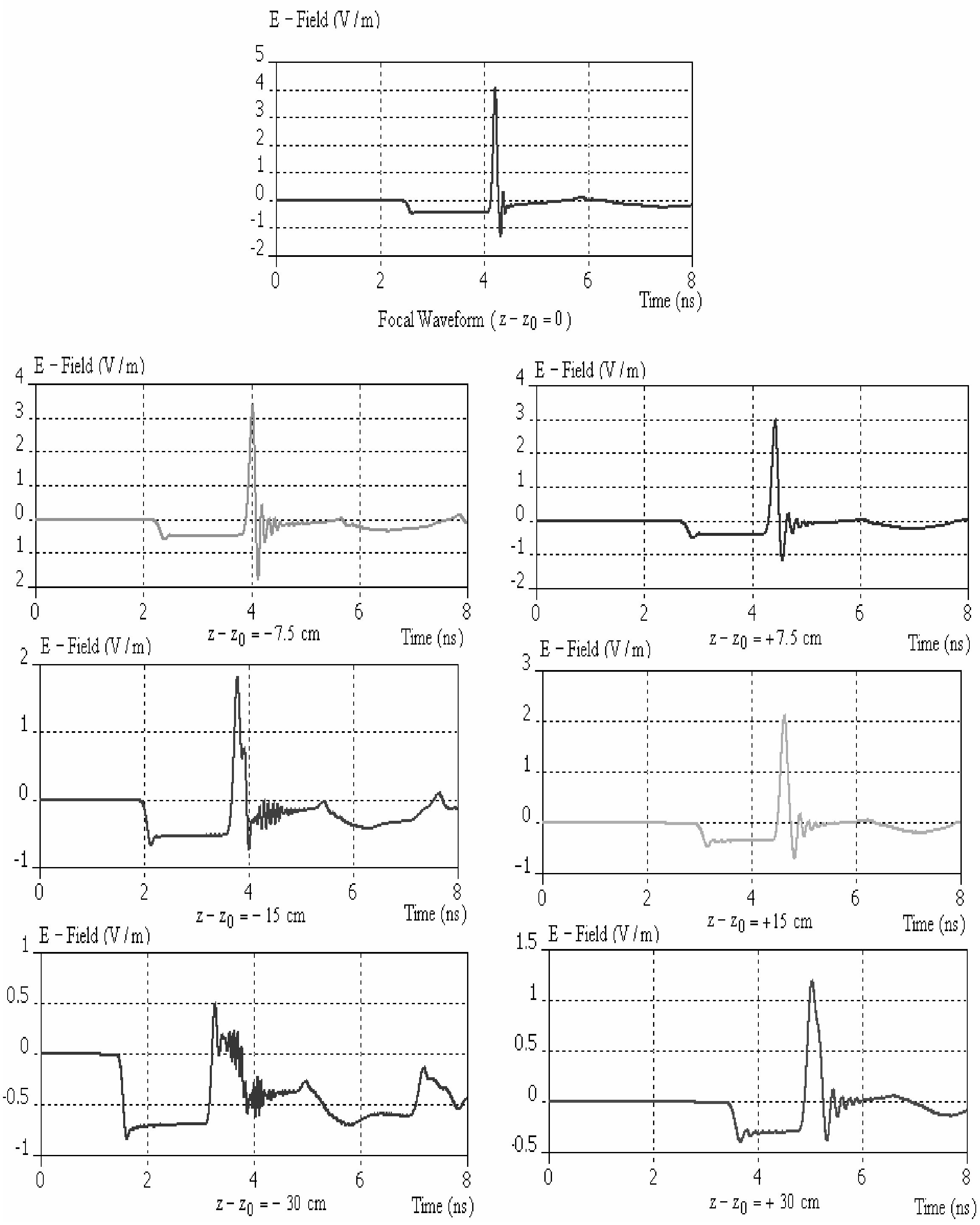

Figure 5.11: Numerical waveforms for 45^{o} four-TEM-feed-arm for various *x*-axis variations.

5.5 Replacing the Prolate-Spheroidal Reflector by an Equivalent Source

In this section, we use an equivalent source on a sphere for separating the target-focusing-lens problem from that of the prolate-spheroidal reflector in order to simplify our problem numerically. Two different electric field variations are imposed on this spherical surface.

5.5.1 Introduction

We have to deal with two different problems to find the focal waveform characteristics of our spheroidal IRA's geometry. First of all our geometry is large compared to the wavelength, and we want to use large dielectric constant materials to obtain better focusing. For numerical simulation we use shells to implement the increase in permittivity. This leads us to simplify the antenna geometry. We use two approaches for simplification. We use a spherical array as an equivalent geometry which is presented in Figure 5.12. Then we impose two different types of electric field variation.

θ , θ_2 , ϕ_2 angles range from

$$0 < \theta < \pi / 2 \ , 0 < \theta_2 < \pi / 2 \ , 0 < \phi_2 < \pi / 2 \ . \tag{5.5}$$

One can see that, for fixed ϕ_2 and constant θ_2, if we let fields vary along r_2 toward 0, the beam edge is around θ_c'.

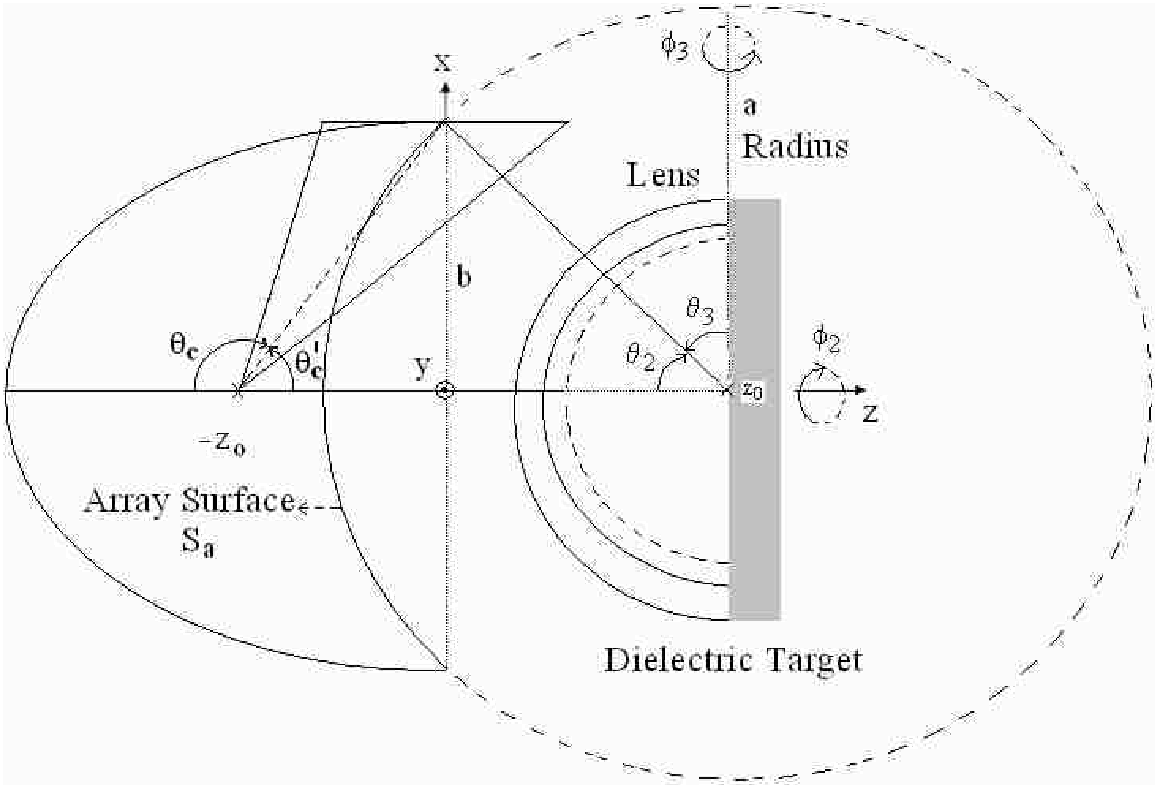

Figure 5.12: IRA and equivalent geometry.

5.5.2 Design Considerations

We impose two different kinds of electric field variation on the S_a surface. These imposed electric field variations are based on (3.13) in [3] and (2.2) in [4]. Thus the imposed field is

$$E_1 = \frac{V_0 b}{\pi f_g a(a - z_0)} \left[\frac{2 cos(\phi_2)}{1 + cos(\theta_2)} \vec{1}_{\theta_2} - \frac{2 sin(\phi_2)}{1 + cos(\theta_2)} \vec{1}_{\theta_2} \right] \begin{cases} u(t) \ \ arrive \ \ center \ \ at \ \ t = a/c \\ u(t + a/c) \ arrive \ center \ at \ t = 0 \end{cases}. \tag{5.6}$$

This is replaced by the leading term in an expansion around the *z*-axis, giving the same field there. The higher order terms ($cos(m\phi), sin(m\phi) > 1$) integrate to zero on (and sufficiently near) the *z*-axis, including the focal point.

$$E_2 = \frac{V_0}{\pi f_g}\frac{b}{a^2 - z_0^2}\sin(\theta_3)\;\vec{1}_{\theta_3}\begin{cases} u(t) & arrive\,center\,at\,t = a/c \\ u(t+a/c) & arrive\,center\,at\,t = 0 \end{cases}. \tag{5.7}$$

Let us write (5.7) in the same coordinate system of (5.6), to obtain (see Figure 5.13)

$$E_2 = \frac{V_0}{\pi f_g}\frac{b}{a^2 - z_0^2}\cos(\theta_2)\left(-\vec{1}_{\theta_2}\cos(\theta_2)\cos(\phi_2) - \vec{1}_{\phi_2}\sin(\theta_2) + \vec{1}_r\cos(\theta_2)\sin(\phi_2)\right). \tag{5.8}$$
$$\begin{cases} u(t) & arrive\;center\;\;at\;\;t = a/c \\ u(t+a/c) & arrive\;center\;\;at\;\;t = 0 \end{cases}$$

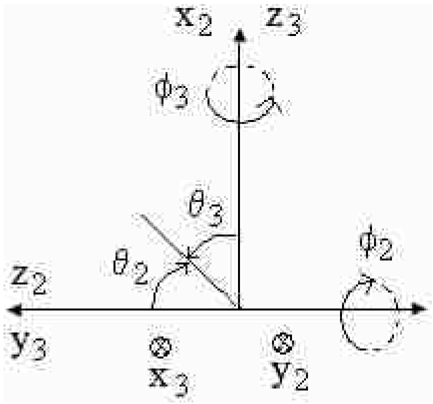

Figure 5.13: Coordinates used in Figure 5.12.

An equivalent source on a sphere is proposed and two different types of electric field variations on this array surface array are imposed. This technique can be used for numerical design; however, it is difficult to impose electric field variation on the surface of a sphere numerically.

6 EXPERIMENTS

6.1 Introduction

Experimental setups using two-arm and 60^o four-arm prolate-spheroidal IRAs are used to obtain better focusing for a prolate-spheroidal IRA and these results are compared with analytical results from Appendix A and Chapter 4 for comparison. This chapter presents a summary of the experimental setup and the dimensions of these experiments are based on [3, 16]. These setups were motivated by a biological application [1].

6.2 Experiments

We feed our IRA using a $V_0 = 0.5\,V$ (peak-peak 1 V) and $t_\delta = 100\,ps$, rise time ramp-rising step. The analytical focal waveforms are presented in Figure 6.1 for this excitation.

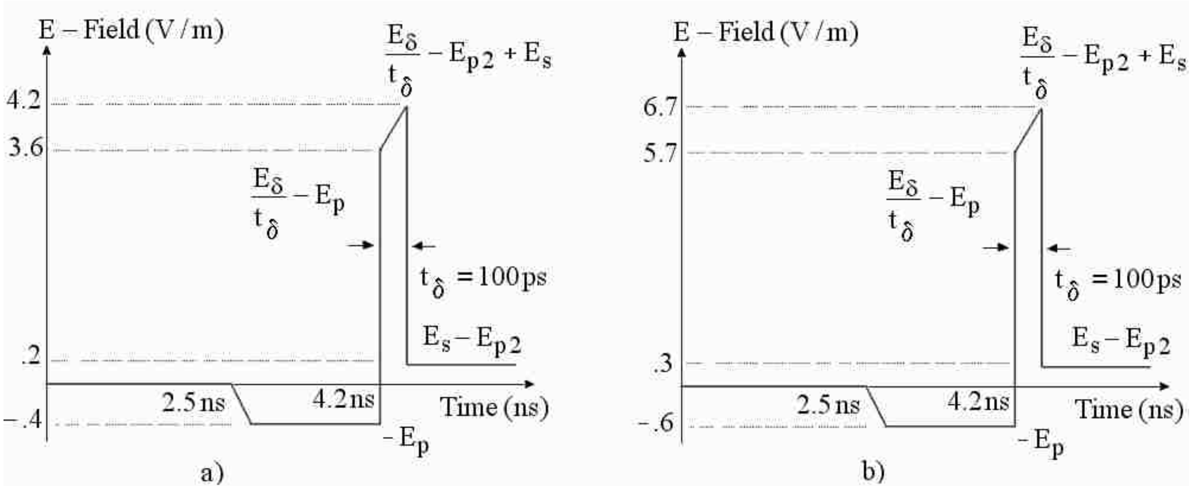

Figure 6.1: Analytical focal waveforms a) two-arms, b) 60^o four-arms.

We use maximum t_{mr} (based on maximum rate of rise) as t_δ to compare our experimental results with analytical results.

6.2.1 Experimental Setup and Data Analysis Technique

The experimental setup basically includes three components. These are a prolate-spheroidal reflector with feed arms, a sampling-oscilloscope, and a pulse generator. They are presented in Figures 6.2 and 6.3.

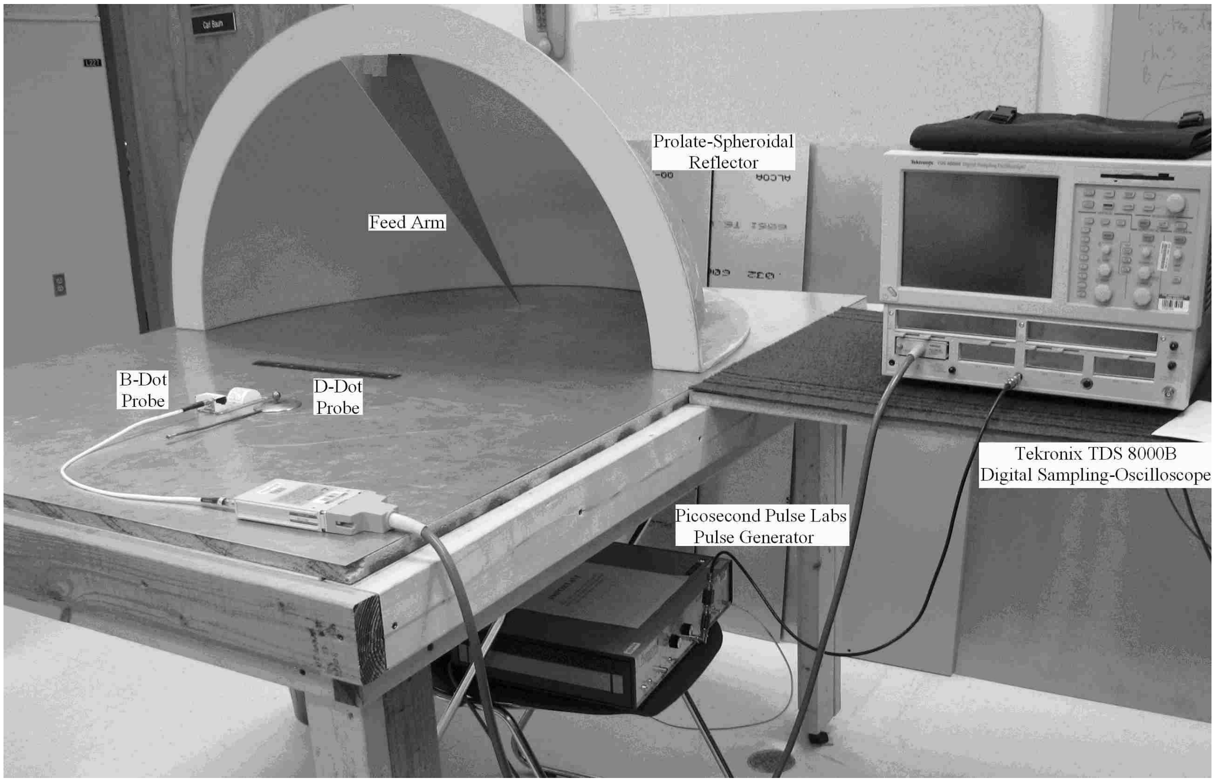

Figure 6.2: Experimental setup for a two-feed arm prolate-spheroidal IRA.

Figure 6.3: Experimental setup for a 60^{o} four-feed arm prolate-spheroidal IRA.

As seen from Figure 6.4, we use a Tektronix TDS 8000B Digital Sampling-Oscilloscope to measure the waveform at the second focal point. A Picosecond Pulse Labs pulser with a PSPL 4050 RPH fast pulser head generator is used for excitation. The output of the step generator is a 45-ps rise time, 10 V amplitude. We have also used a 10 dB attenuator to decrease the voltage level for safety reasons. Two nano-second and three nano-second long cables are used to connect the pulser to the feed arms and sensors to the sampling oscilloscope.

Figure 6.4: Sampling-oscilloscope and pulse generator.

The feed arms' dimensions are calculated in Chapter 4 (Table 4.1 and 4.2) and they are presented in Figure 6.5. The feed arms are 0.8 cm thick.

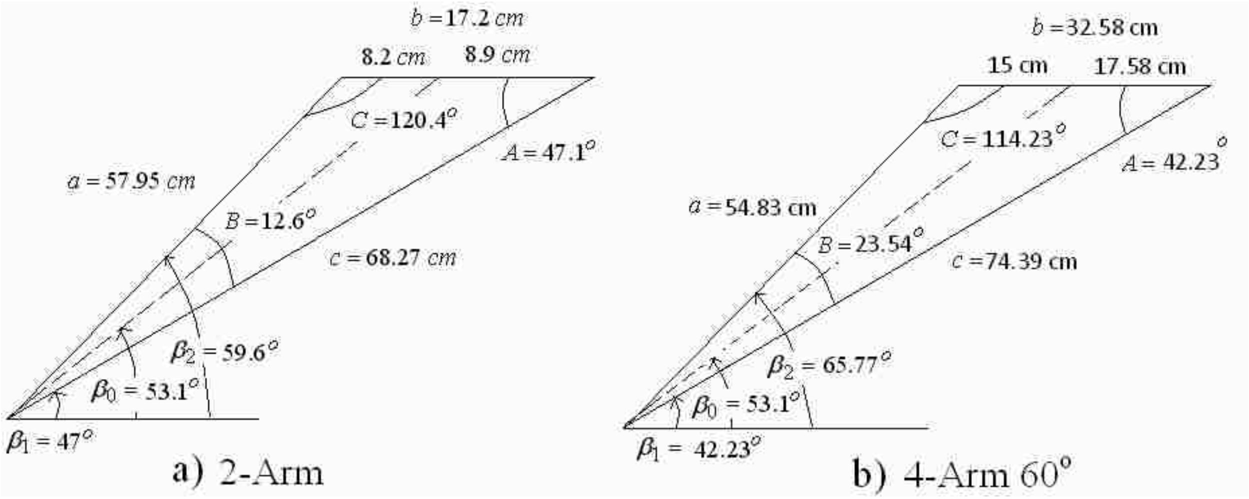

a) 2-Arm

b) 4-Arm 60°

Figure 6.5: Two-feed arms and 60^o four-feed arms dimensions and angles.

One can see the 60^o four-feed arms IRA in Figure 6.6 and how it is inserted in the reflector. We use foam with a relative dielectric constant $\varepsilon_r = 1.013$ to maintain the feed arms angle at 60^o.

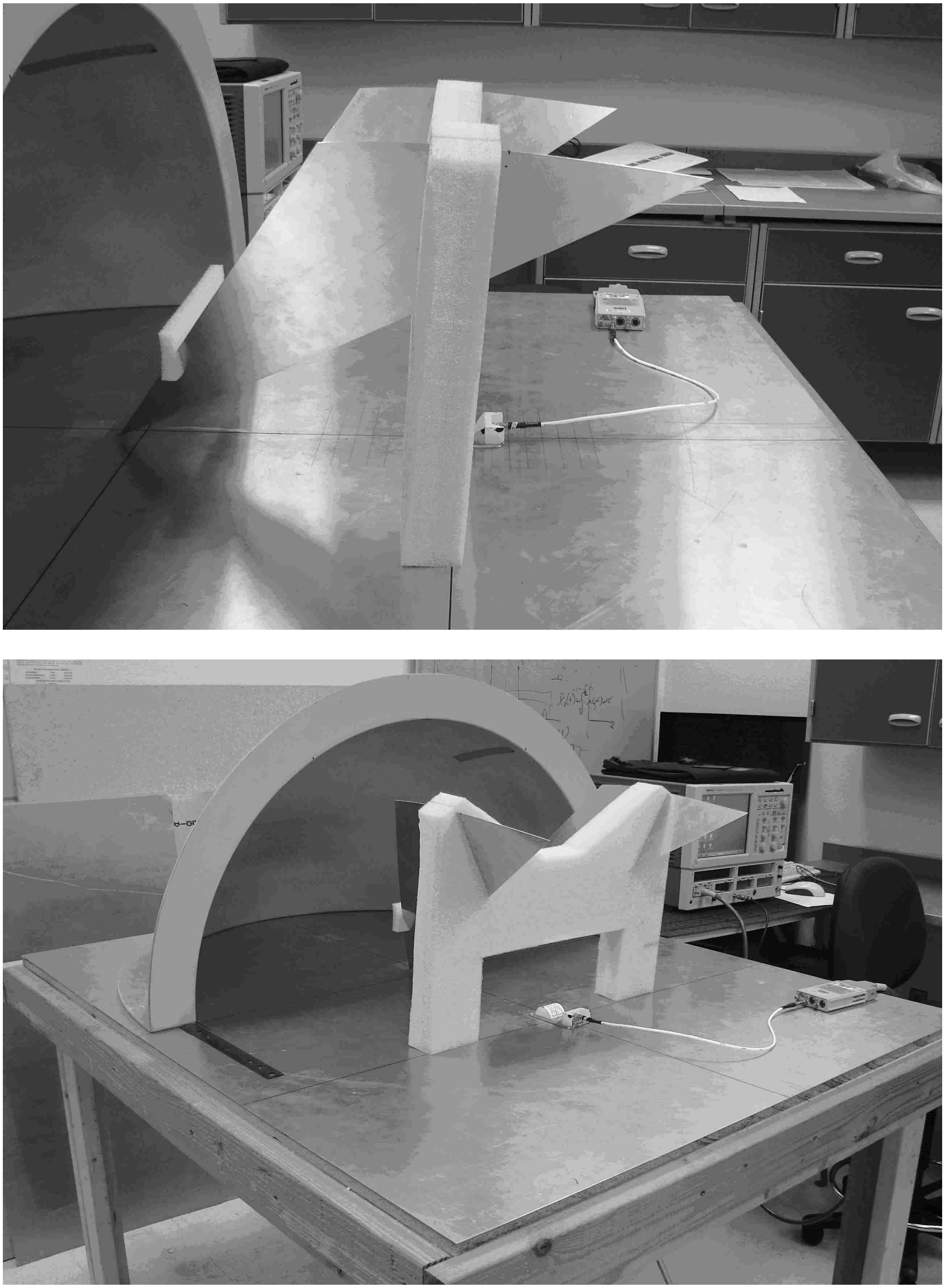

Figure 6.6: 60° four-feed arms used in one of the IRAs.

Fast D-Dot, slow D-Dot and B-Dot probes are used for field measurements and are presented in Figure 6.7. We use the B-Dot probe to obtain the magnetic field and also use the prepulse data of the B-Dot probe to calibrate the slow D-Dot probe data. We use the data from the B-dot probe which has an equivalent area $A_{eq} = 1\ cm^2$ and analyze the data as follows:

$$\begin{aligned} V &= A_{eq}\frac{dB}{dt}, \text{ and} \\ B &= \frac{1}{A_{eq}}\int_{-\infty}^{t} V(t')\,dt'. \end{aligned} \tag{6.1}$$

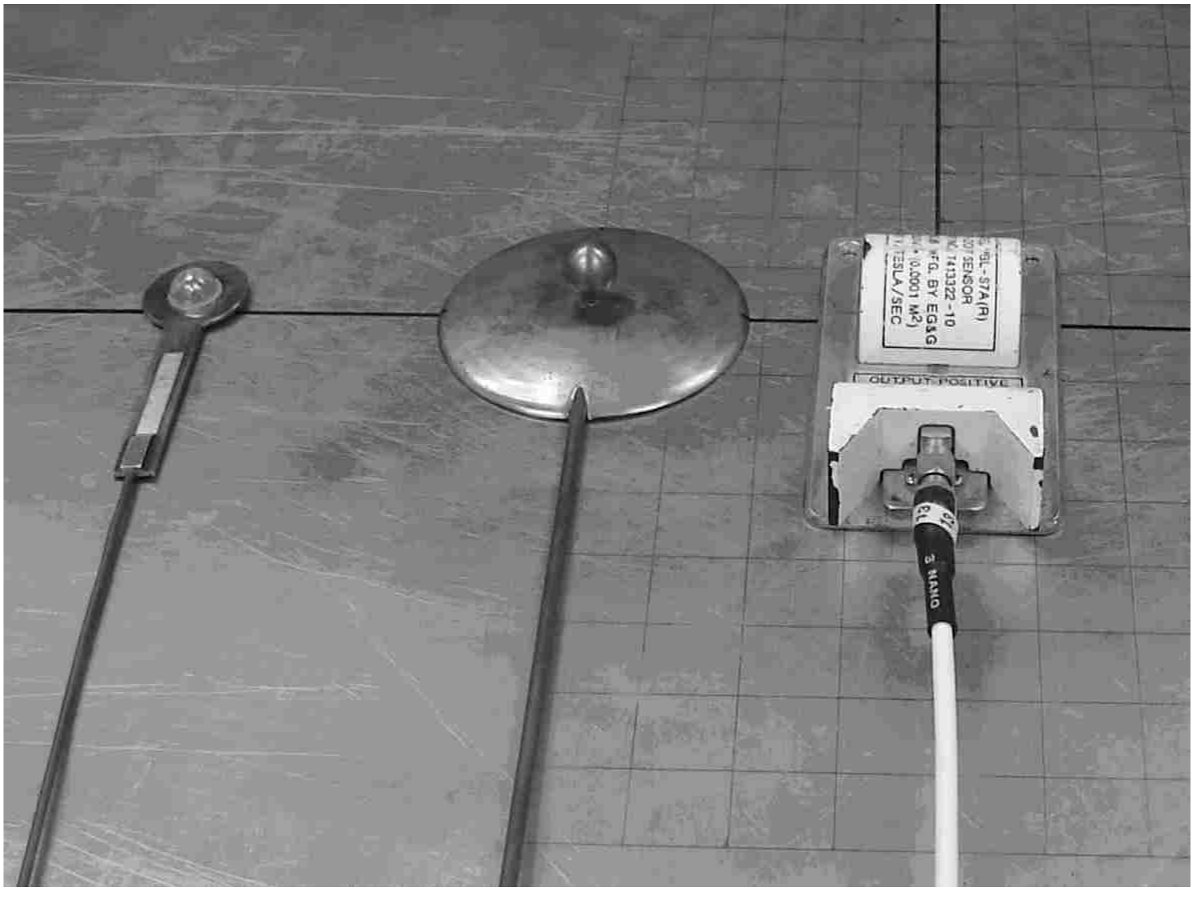

Figure 6.7: Fast D-Dot, slow D-Dot and B-Dot probes (from left to right) used for measurements.

We can find the equivalent electric field as

$$E_{eq} = cB = \frac{c}{A_{eq}} \int_{-\infty}^{t} V(t')\,dt' . \tag{6.2}$$

This equivalent electric field, E_{eq}, gives the exact result for the prepulse because we have a TEM wave and $E / H = \eta_0 \approx 377\ \Omega$ for free space. We calibrate our D-Dot data by comparing the prepulse term. We obtain the data from the D-Dot probe and analyze it as follows:

$$\begin{aligned} I &= \frac{V}{Z_0} = A_{eq} \frac{dD}{dt}, \text{ and} \\ E &= \frac{1}{\varepsilon_0\, Z_0\, A_{eq}} \int_{-\infty}^{t} V(t')\,dt' . \end{aligned} \tag{6.3}$$

Our pulse generator has a $V_0 = 10\,V$ excitation we feed our IRA with

$$V = T\ V_0 , \tag{6.4}$$

where T is the transmission coefficient

$$T = \frac{2Z_L}{Z_L + Z_0} . \tag{6.5}$$

The pulse impedances for the two-arm and 60^o four-feed arm cases are $400\ \Omega$ and $200\ \Omega$, respectively. Since we are using a ground plane $Z_L = 200\ \Omega\ and\ 100\ \Omega$, respectively. The transmission coefficients are 1.6 and 1.33. In our analytical calculation we use $V_0 = 0.5\,V$ and then normalize the data to obtain the electric field as

$$E_N = \frac{1}{20 T\, \varepsilon_0\, Z_0\, A_{eq}} \int_{-\infty}^{t} V(t')\,dt . \tag{6.6}$$

6.2.2 Experimental Results Normalized to 1 Volt Differential Input

Figures 6.8 and 6.9 shows that the results for the focal waveforms are close to each other but for the slow D-Dot sensor we do not have much oscillation in the postpulse since it has a slower frequency response. Although we do not have TEM waves for impulse, we calculate $\eta = E / H$. For the two-arm case η is 384, for the four-arm case η is 408. However in free space $\eta_0 = 377\,\Omega$. This proves that we do not have a purely TEM wave for the impulse.

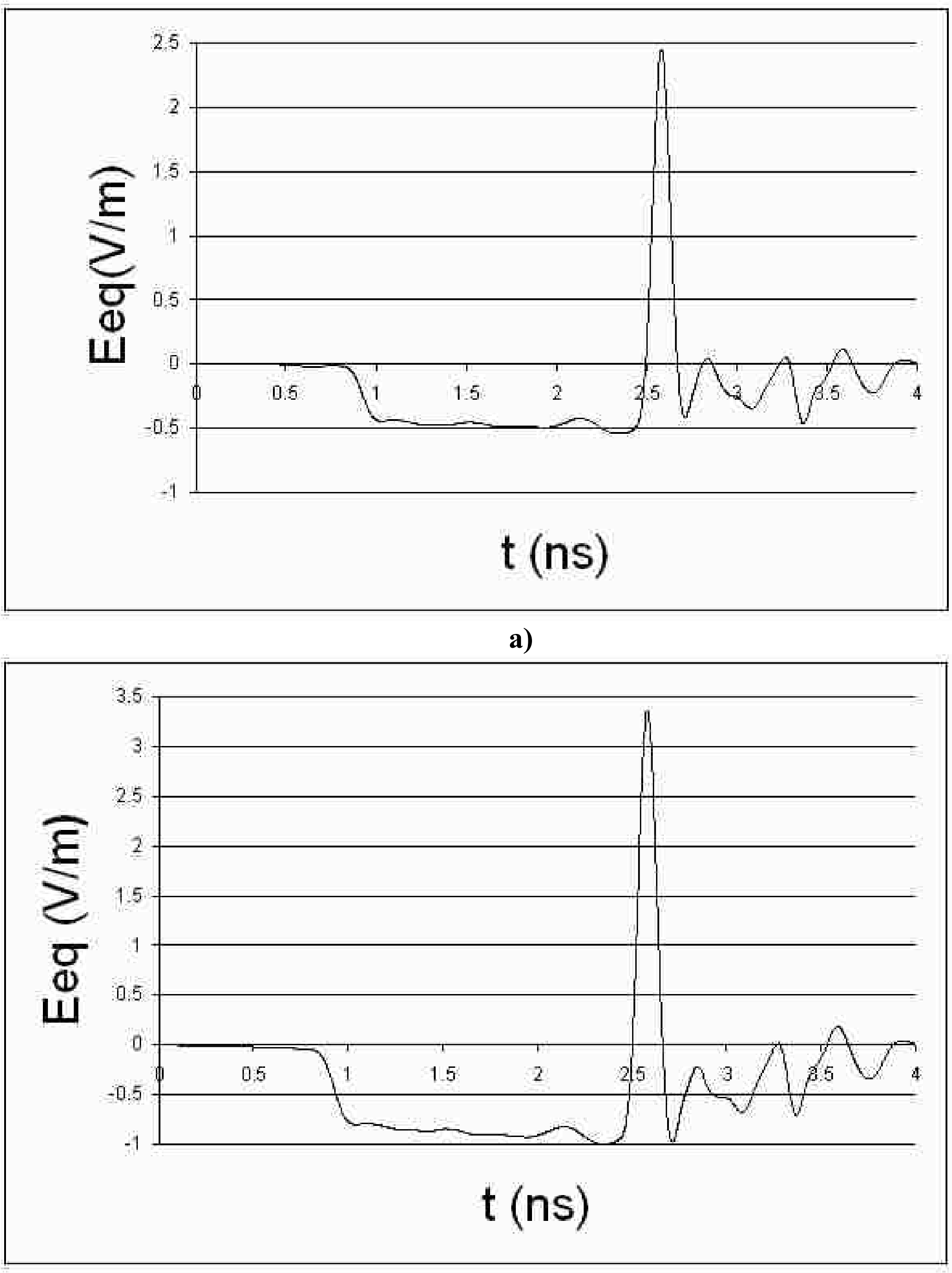

a)

b)

Figure 6.8: B-Dot probe focal waveforms, E_{eq} for a) two-arms, and b) 60^{o} four-feed arms.

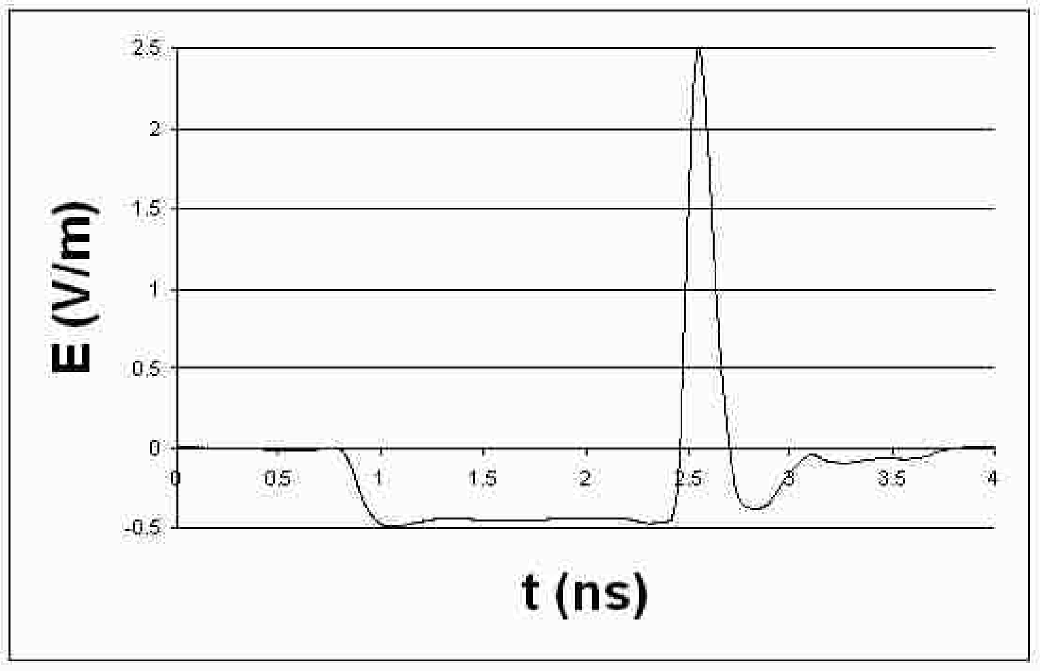

a)

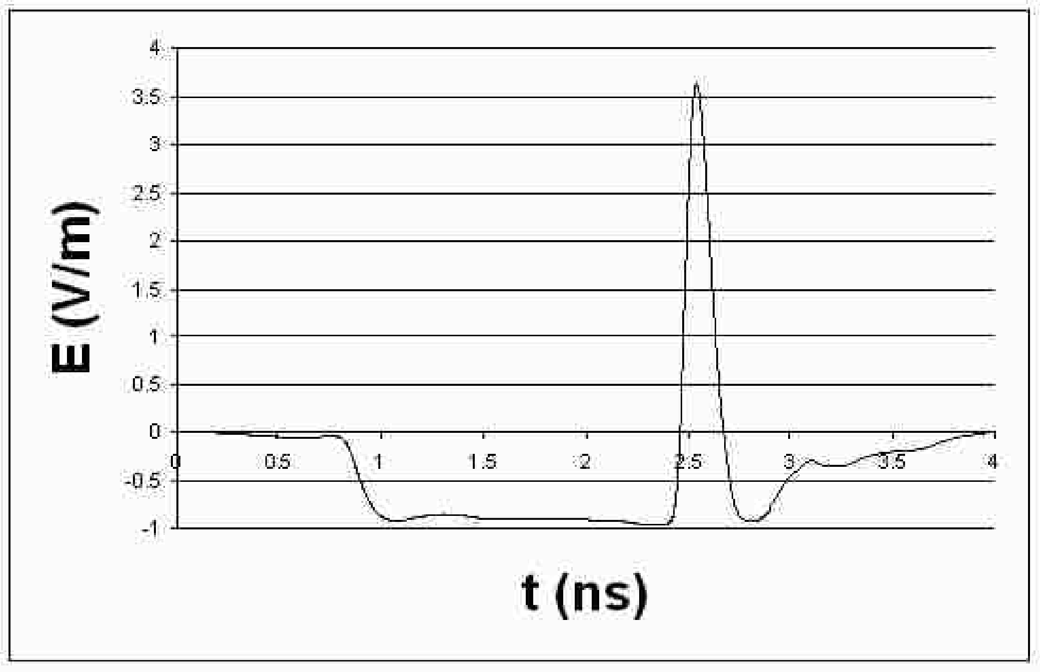

b)

Figure 6.9: Slow D-Dot probe focal waveforms, for a) two-arms, and b) 60^o four-feed arms.

We can see from Figure 6.10 that if we use the fast D-Dot sensor we have this oscillation the oscillation may not be due to the different type of sensors we are using.

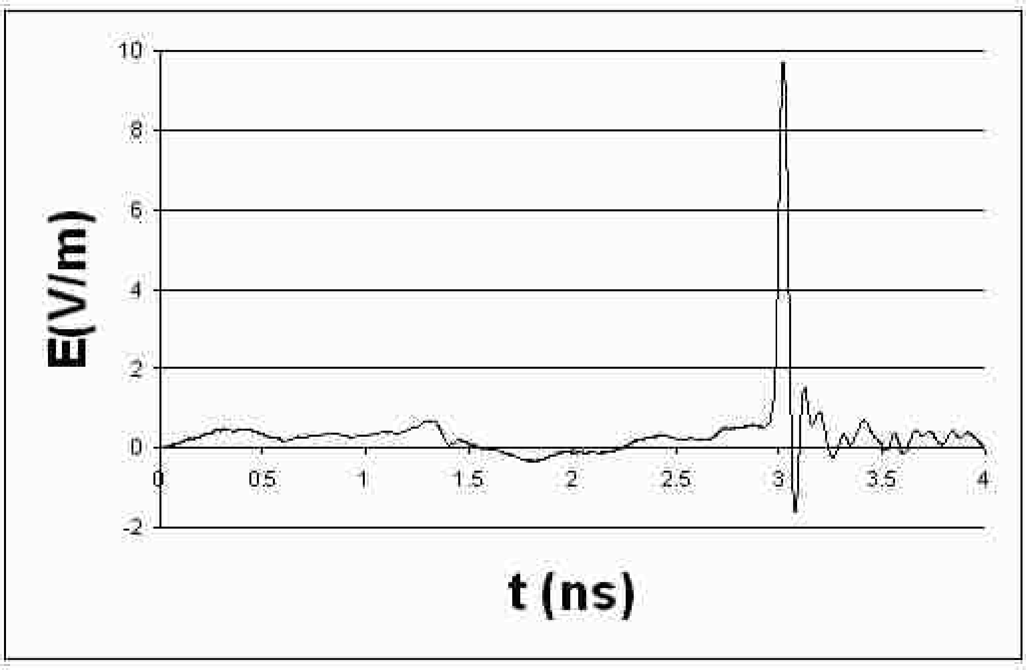

a)

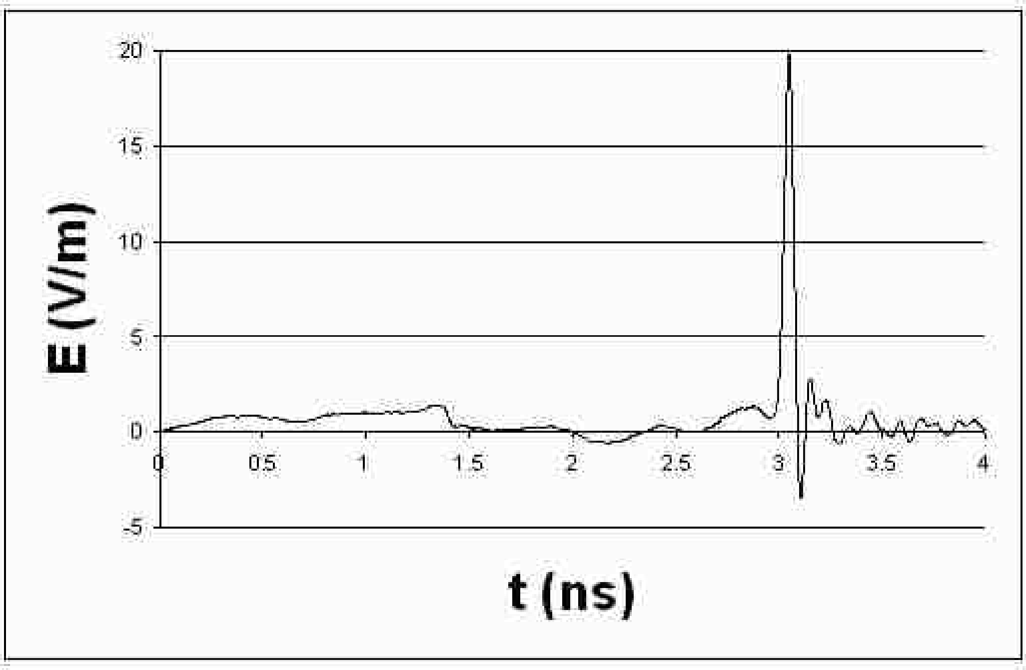

b)

Figure 6.10: Fast D-Dot probe focal waveforms for a) two, b) 60^o four-feed arms.

Figure 6.11 presents a comparison of the focal waveform from the B-Dot and the normalized focal waveform from the fast D-dot. They oscillate at different frequencies. The fast D-Dot sensor response is very fast; this can cause differences in the postpulse. We do not have that much ringing in the slow D-Dot postpulse. The B-Dot sensor causes a 3 GHz ringing.

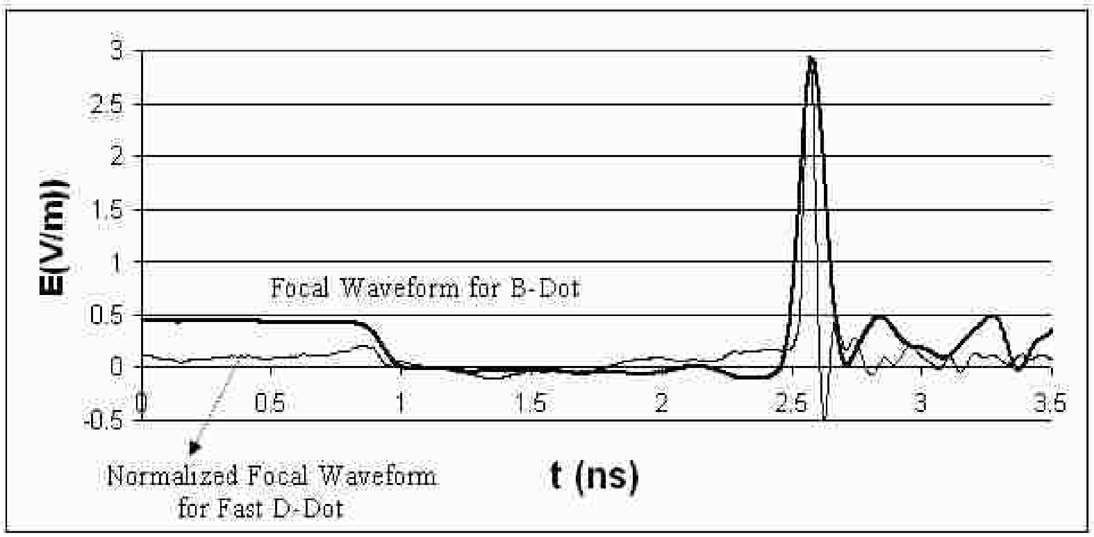

Figure 6.11: Focal waveform from the B-Dot and normalized focal waveform from the fast D-Dot measured of the two-arm IRA.

We connect the B-Dot probe directly to the oscilloscope. Figure 6.12 shows the measured reflection coefficient and arrows show the ringing that can cause the postpulse oscillations.

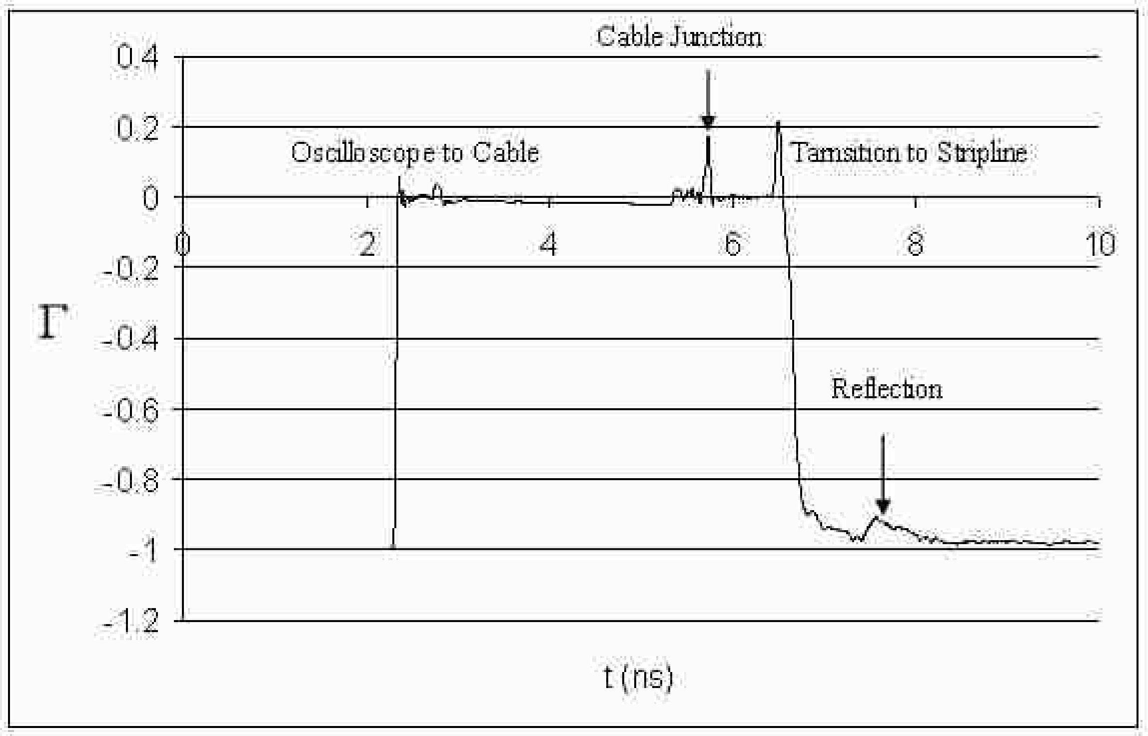

Figure 6.12: Reflection coefficient (Γ) measurements: The B-Dot probe directly connected to the oscilloscope.

There will always be causes for oscillations and aberrations at the levels observed in the fast D-dot trace. There are cable and connection non uniformities, nonlinear effects in the sampler, sampling time errors, digitizing errors, etc. Most importantly, the generator signal is not pure and has lots of aberrations following the step.

6.2.3 Conclusion

Table 6.1: Maximum values of the Eeq variation along the y and z -axis from the B-Dot sensor.

	Focal E(V/m)	y<0, z=0	E (V/m)	y>0, z=0	E (V/m)	y=0, z<0	E (V/m)	y=0, z>0	E (V/m)
2 Arm	2.45	y=-2cm	2.27	y=2cm	2.01	z=-1cm	2.46	z=1cm	2.41
		y=-4cm	2.27	y=4cm	1.44	z=-2cm	**2.47**	z=2cm	2.40
		y=-6cm	1.15	y=6cm	0.97	z=-4cm	2.35	z=4cm	2.28
		y=-8cm	0.79	y=8cm	0.66	z=-6cm	2.21	z=6cm	2.18
						z=-8cm	2.03	z=8cm	2.07
						z=-10cm	1.80	z=10cm	1.95
						z=-12cm	1.57	z=12cm	1.69
						z=-14cm	1.30	z=14cm	1.48
						z=-16cm	1.12	z=16cm	1.38
4 Arm	3.36	y=-2cm	2.95	y=2cm	2.56	z=-1cm	3.41	z=1cm	3.32
		y=-4cm	2.94	y=4cm	1.50	z=-2cm	**3.42**	z=2cm	3.27
		y=-6cm	1.02	y=6cm	0.94	z=-4cm	3.25	z=4cm	3.13
		y=-8cm	0.86	y=8cm	0.89	z=-6cm	2.90	z=6cm	3.01
						z=-8cm	2.65	z=8cm	2.85
						z=-10cm	2.35	z=10cm	2.69
						z=-12cm	2.26	z=12cm	2.35
						z=-14cm	1.85	z=14cm	2.09
						z=-16cm	1.52	z=16cm	1.93

As seen in Table 6.1, our focal point is about 2 cm closer to the reflector because we do not have sufficient high frequency components and we also have a step term E_s affecting of the amplitude of impulse. Figure 4.3 shows that the amplitude of the impulse is proportional to E_δ and E_s, but E_δ is the dominant term. The E_δ value is larger for high frequencies and E_s is larger at the aperture plane. E_s decreases more than E_δ toward the focal point. Thus we have two computing parameters, E_δ and E_s. Because of these two terms, our peak point is 2 cm closer to the reflector. At the focal point our prolate-spheroidal IRA works like a differentiator or high-pass filter, high frequencies contribute more than low frequencies.

Although the amplitudes of the electric fields should be symmetric along the *x*-axis with respect to x=0, they are different. We believe this is because of errors in the geometric shape or alignment of the prolate-spheroidal reflector.

The slow sensors are more sensitive than the fast D-Dot sensor, but they are not fast enough to obtain the actual t_{mr} values. We obtain larger t_{mr} values which result in a decrease in the amplitude of the impulse part of the focal waveform. If we use the fast D-Dot sensor, it is not sensitive enough. We obtain higher amplitudes in the impulse part, whereas we obtain more differences in the amplitude of the impulse part of the focal waveform. The analytical, experimental results, oscillation amplitude, t_{mr} and differences in experimental results compared to the analytical results are summarized in Table 6.2.

Table 6.2: Analytical, experimental results, oscillation amplitude, t_{mr} and difference in experimental results compared to analytical results.

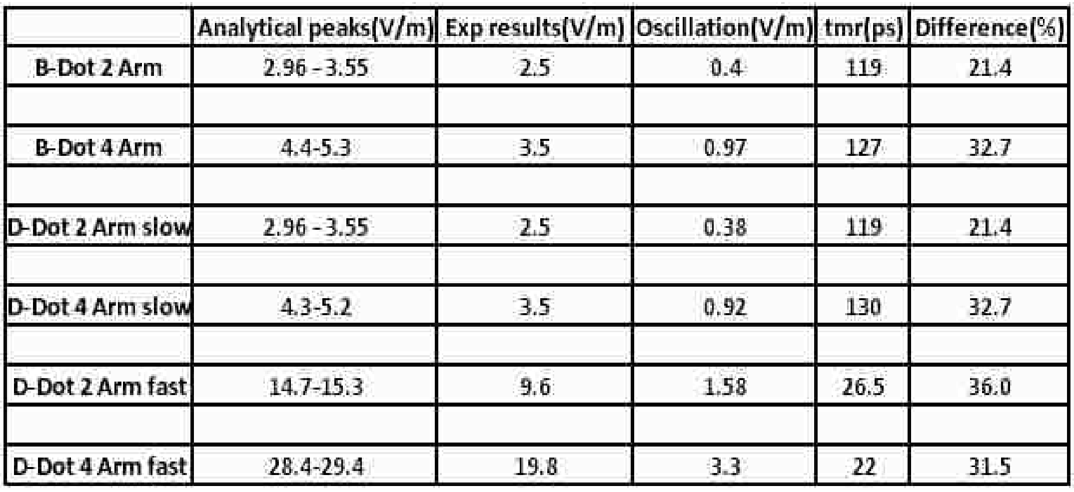

	Analytical peaks(V/m)	Exp results(V/m)	Oscillation(V/m)	tmr(ps)	Difference(%)
B-Dot 2 Arm	2.96 – 3.55	2.5	0.4	119	21.4
B-Dot 4 Arm	4.4-5.3	3.5	0.97	127	32.7
D-Dot 2 Arm slow	2.96 – 3.55	2.5	0.38	119	21.4
D-Dot 4 Arm slow	4.3-5.2	3.5	0.92	130	32.7
D-Dot 2 Arm fast	14.7-15.3	9.6	1.58	26.5	36.0
D-Dot 4 Arm fast	28.4-29.4	19.8	3.3	22	31.5

There are several factors that can lead to differences in the analytical expressions and experiments. When the focal fields are calculated in Chapter 4 and [3], the aperture integral did not consider the feed arms and feed-arms' thicknesses. This can cause an error in the calculation of the impulse amplitude of the focal waveform.

There are errors in the experiments that need to be accounted for. We are in the limit of our instrumentation, we have less accuracy because of the limitation of the probes.

We have checked the pulser and the connection cables to find the reason for the postpulse oscillations. These results are presented in Figure 6.13. One can see from Figure 6.13 that the postpulse oscillations are not related to the pulser or the 2 nano-second and 3 nano-second long cables that we use to connect the pulser to the feed arms and sensors to the sampling oscilloscope. They are not oscillating at the same frequencies and they do not have the same amplitudes. We do not have any problem with the pulser and connection cables.

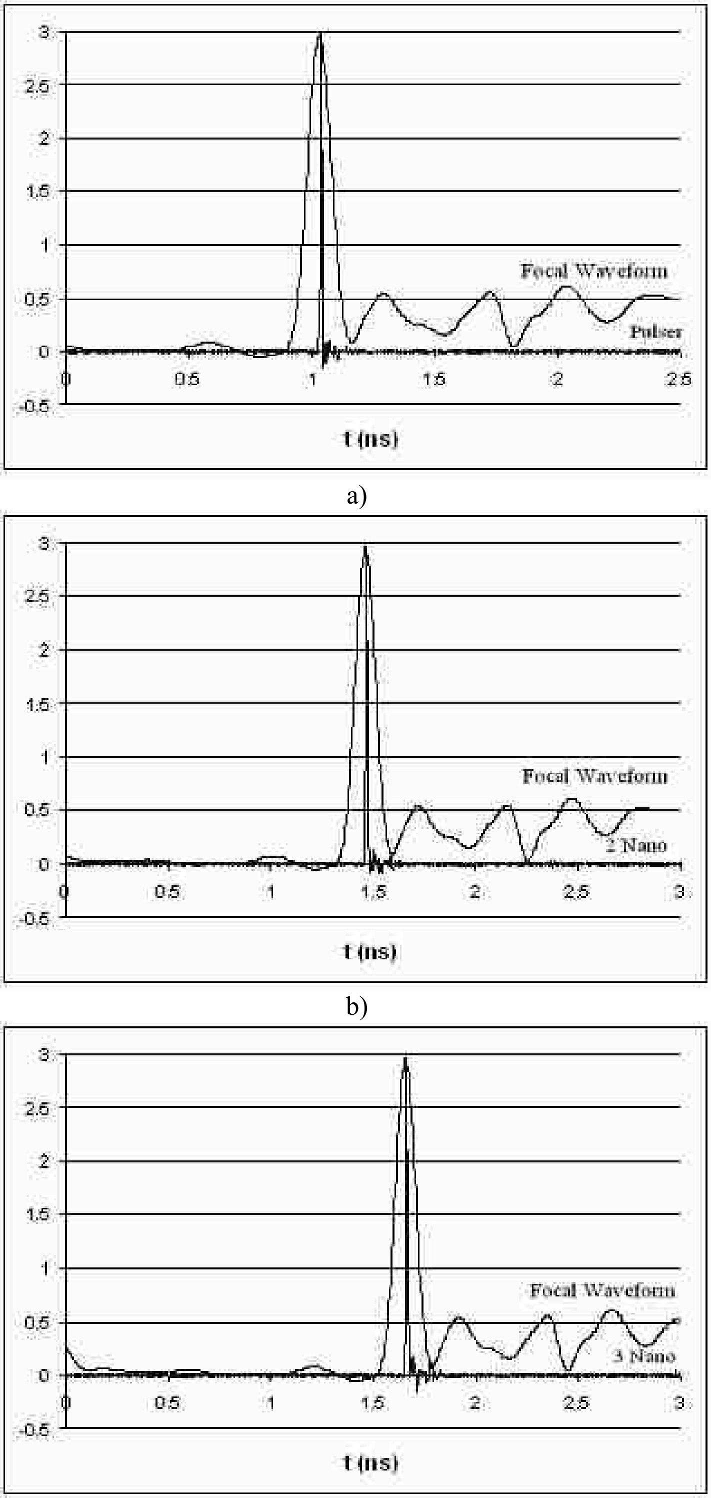

a)

b)

c)

Figure 6.13: The focal waveform data: a) the normalized data from the pulser, b) with 2 nano-second, c) with 3 nano-second long cables.

We next checked the prepulse term and took its derivative, shown in Figure 6.14.

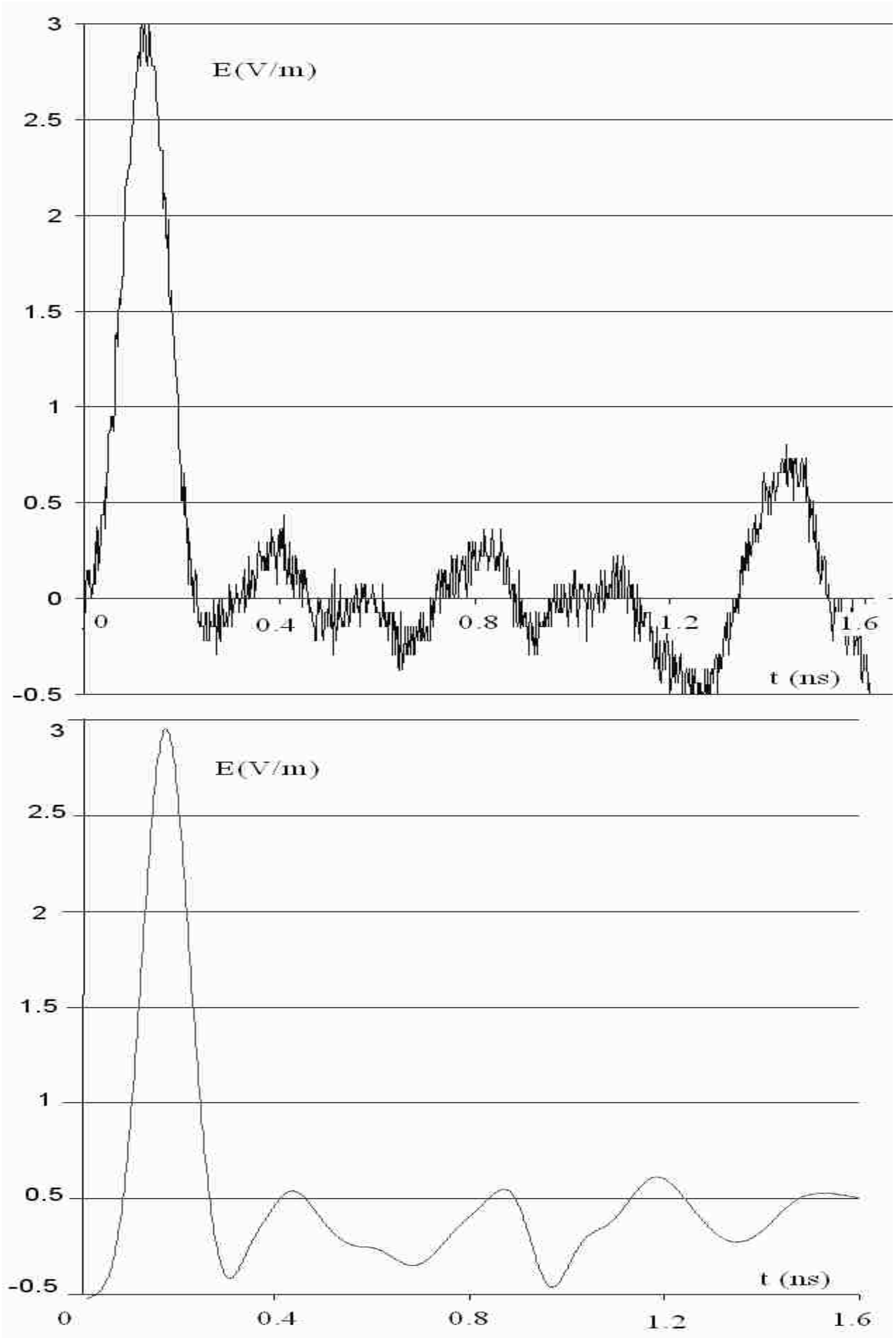

Figure 6.14: The derivative of the normalized prepulse term and the focal waveform.

In Figure 6.14 we compare the derivative of the normalized prepulse term and the focal waveform. They are oscillating at similar frequencies. This proves that the ripples in the prepulse cannot be associated with the feed arms near the reflector, by causality (speed of light). The ripples come from the prepulse not from the reflected waves; we do not have any problem with the reflector and the feed arms. These ripples come either from the feed point or from the sensor. We considered the feed point first and measured the reflection coefficient (Γ) to check for problems with it.

One can see the reflection coefficient (Γ) values from Figure 6.15. It starts from -1 at short circuit, it goes to 0 when the current reaches the 50 Ω cable, it goes to 0.3 when it reaches the feed arms. Finally, it goes to -1 because the reflector feed arms are shorted. We can calculate the feed arms pulse impedance as

$$\Gamma = \frac{Z_L - Z_0}{Z_L + Z_0} . \tag{6.7}$$

$\Gamma = 0.3$ and $Z_L = 93\,\Omega$, which is close to the our analytical value of $Z_L = 100\ \Omega$ we do not have any problem in the feed arms geometry.

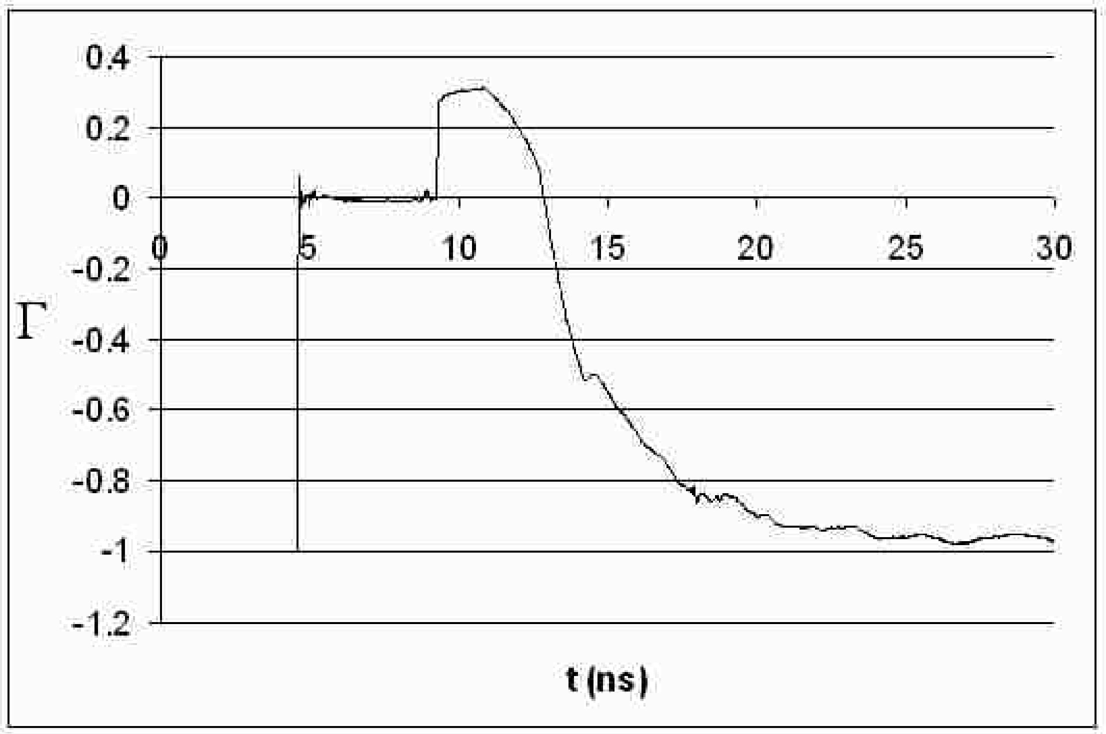

Figure 6.15: Reflection coefficient (Γ) measurements of the reflector with feed arms for impulse impedance calculation.

Figure 6.16 shows the ripples in the Γ with feed arm and open circuit case. If we compare the normalized derivative of the Γ with the focal waveform for feed arms and open circuit case as presented in Figure 6.17, they do not oscillate at the same frequencies, the transition between barrels may not cause these oscillations. Even if we have perfect connection between the feed arms and excitation point, it is difficult to obtain the actual focal waveform because of geometric restrictions. This can cause some differences but it should not be that significant.

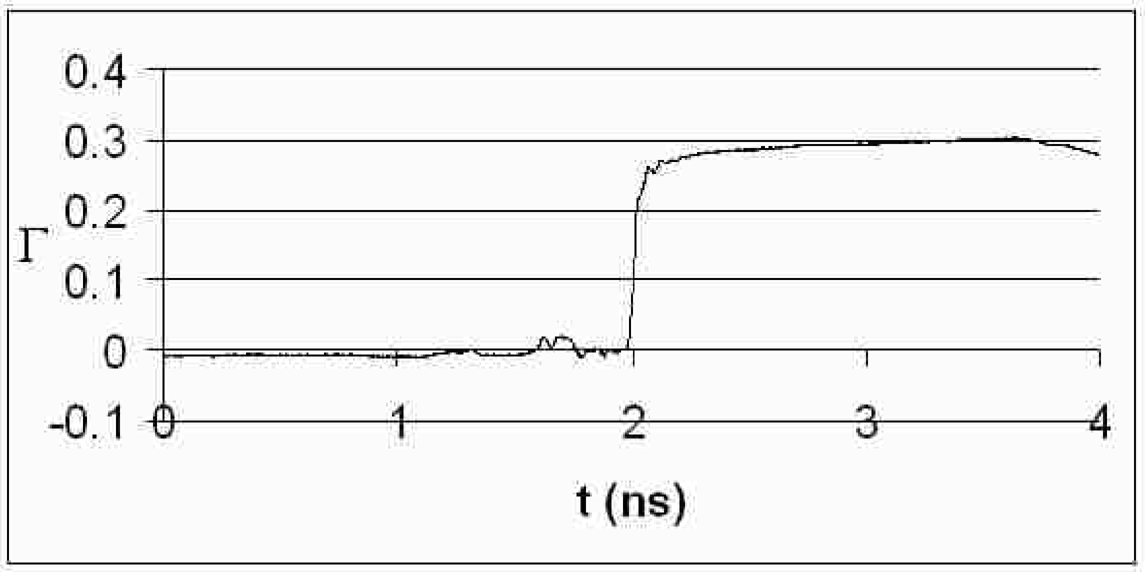

a)

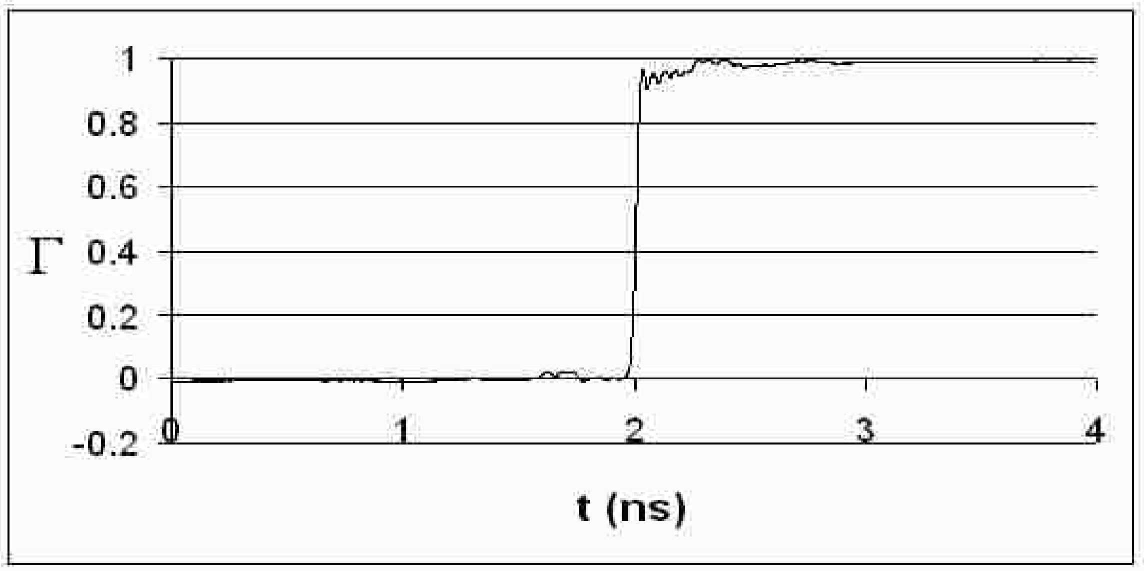

b)

Figure 6.16: Reflection coefficient (Γ) measurement a) with feed arms, b) open circuit.

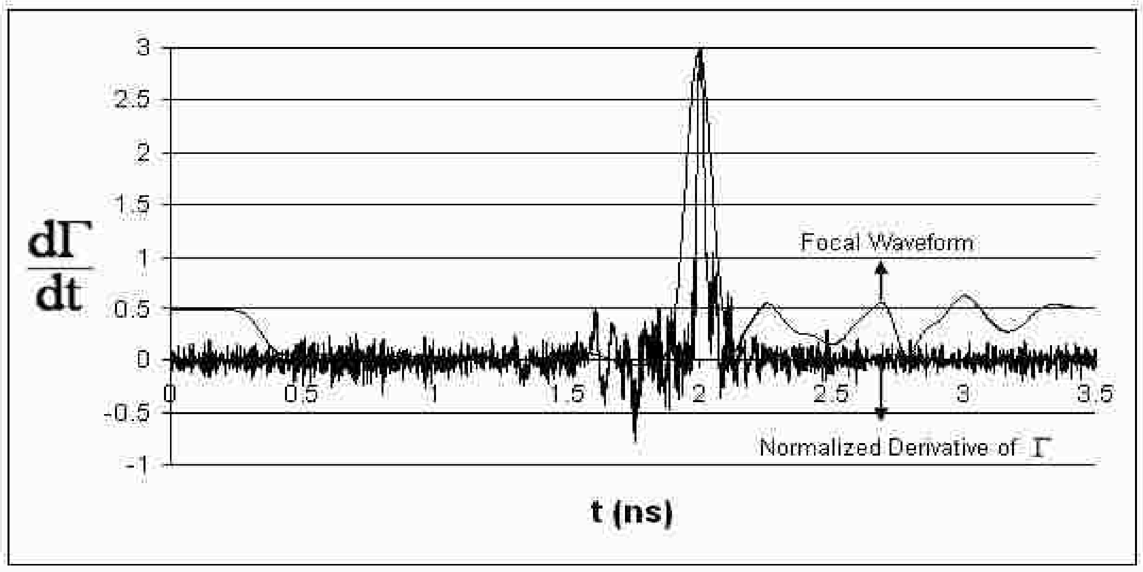

a)

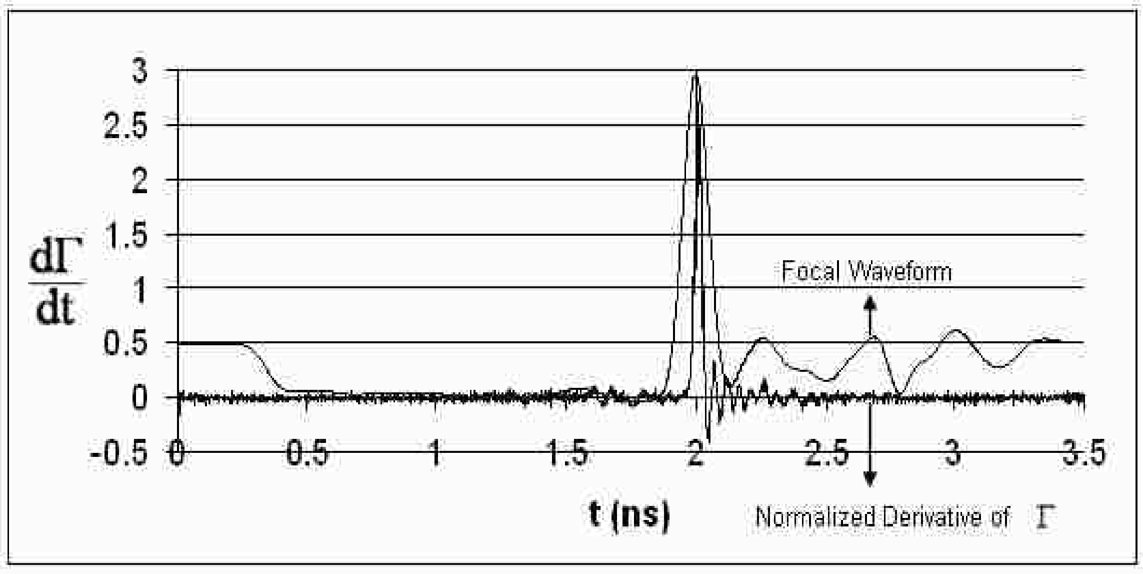

b)

Figure 6.17: Normalized derivative of Γ and focal waveform a) with feed arms, b) open circuit.

We can see from Figure 6.12 that the B-Dot sensor causes the ringing in the postpulse. For the D-Dot probe we cannot obtain the expected analytical postpulse. There should also be another factor causing the ringing and the decrease in the amplitude. When the focal fields are calculated in [3] and Appendix A, the aperture integral does not consider the feed arms and feed-arms' thicknesses. This can cause an error in the calculation of the impulse amplitude of the focal waveform; we believe this can cause the inconsistency between the analytical and experimental results. We want to see the effect of the feed arms on the aperture plane S_a, we performed another experiment. Assume we have an arbitrary piece of metal (13cmX18cmX0.8cm) on the aperture plane S_a. Figure 6.18 shows the experiments that are presented in Figure 6.19.

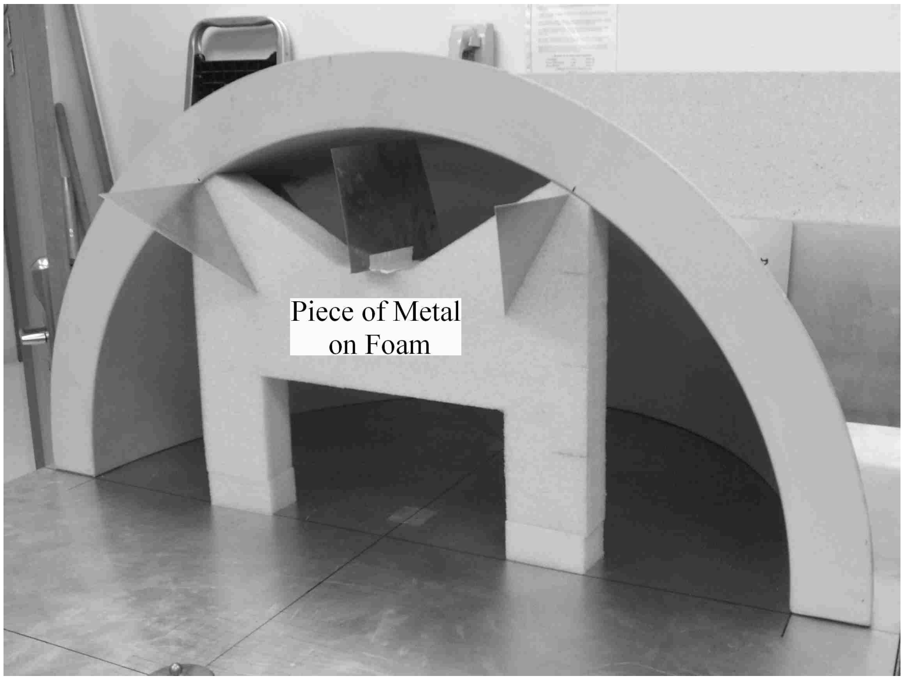

a)

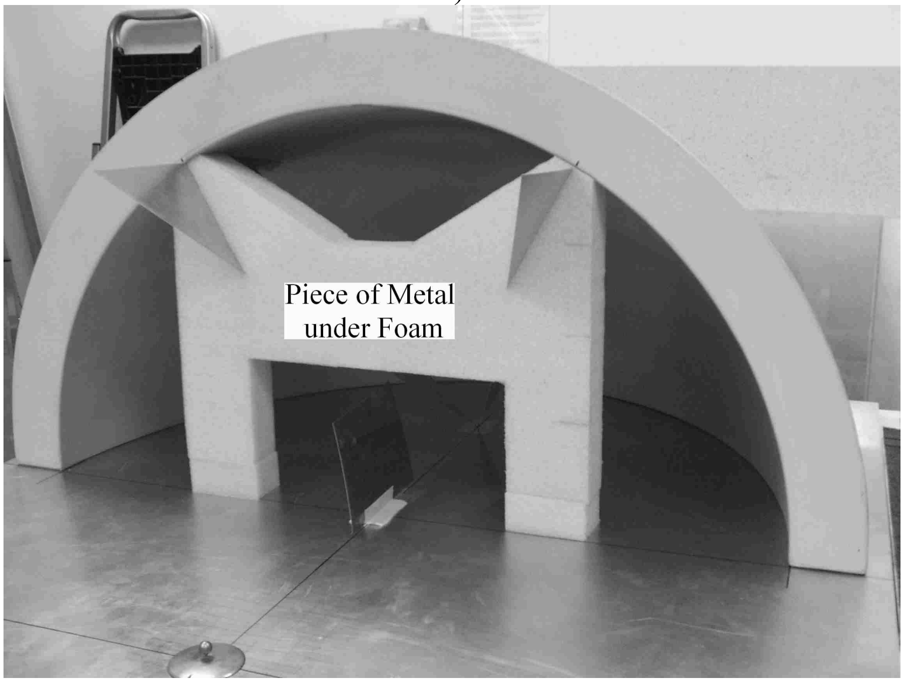

b)

Figure 6.18: 60^o four-feed arms a) with a piece of metal on the foam, b) with a piece of metal under the foam.

In Figure 6.18 metal conductors are on the aperture plane S_a where we integrate the fields to find the focal field at the second focal point. We try to see the effect of the feed arms on the aperture integral by inserting a piece of metal.

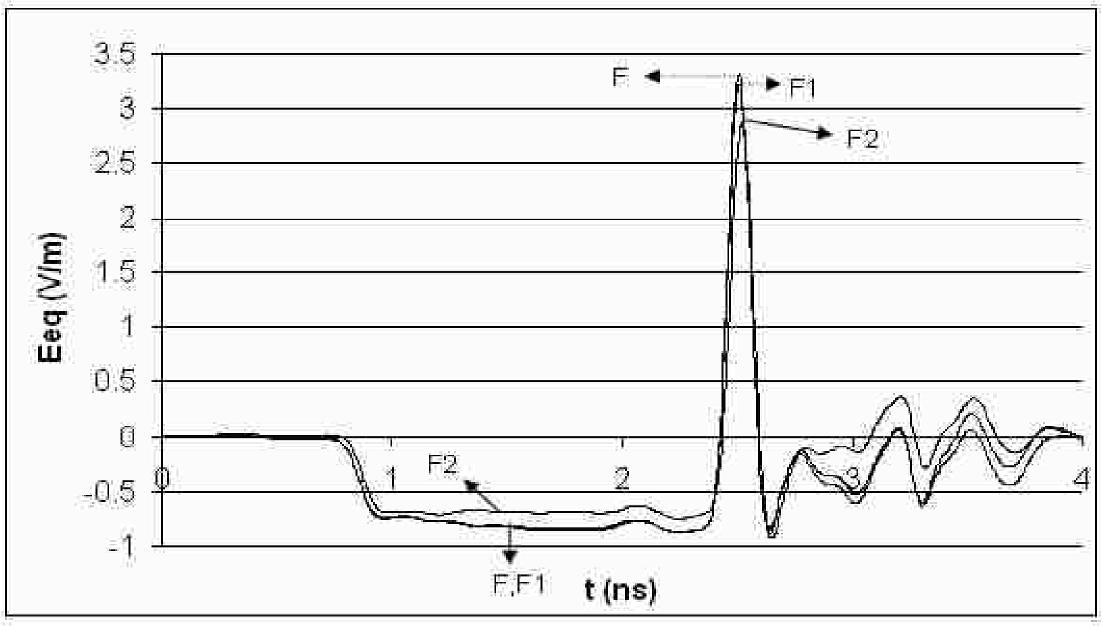

Figure 6.19: Focal waveforms from B-Dot probe for 60^o four-feed arms: F (focal waveform), F1 (focal waveform with a piece of metal on the foam), F2 (focal waveform with a piece of metal under the foam).

Table 6.3: Maximum values of F, F1 and F2.

Max(F (V/m))	Max(F1(V/m))	Max(F2(V/m))
3.32	3.23	2.86

Figure 6.19 presents the values of F (focal waveform), F1 (focal waveform with a piece of metal on the foam), and F2 (focal waveform with a piece of metal under the foam). The peak value of these waveforms are given in Table 6.3. In Figure 6.19, the behaviors of F and F1 are almost the identical. However, as seen from Table 6.3, F1<F but as expected this difference is not significant. This is because we have a null point

right between the feed arms at the top of the reflector. We have a significant difference between the behavior of F and F2.

One can easily see that, although inserting a metal on the top of the S_a does not disturb the field that much because of the null point, inserting a metal under the foam disturbs the focal field. If we insert a piece of metal under the foam, we have aperture scattering. Significant destructive interference occurs because of the feed arm itself and it blocks the reflected fields. The reflected fields are scattered through diffraction.

We can easily find the difference by comparing F and F2 from Table 6.3

$$\mathit{Difference(\%)} = \frac{F - F2}{F} * 100 = \frac{3.32 - 2.86}{3.32} * 100 = 14\% . \tag{6.8}$$

A 14% difference is a significant difference. If we compare F and F1, we have a difference of about 3%. The feed arm itself does not affect the prepulse because the prepulse is the direct radiated field from the feed arms we obtain almost the exact prepulse value in our experiments; however, any other metal scatters the prepulse field.

The geometric shape or alignment of the prolate-spheroidal reflector may also causes some errors. The misshape of the reflector will lead to a broader focus and smaller amplitude.

The prolate-spheroidal reflector was manufactured from fiber and the inside of the reflector is painted with copper conductive paint. The surface resistivity of the paint is <0.3 ohm/square at 1 mil dry film thickness; <0.10 ohm/square at 2 mil dry film thickness. We checked the reflection from the conductive paint on the reflector and measured about 99% reflection; however, there might be some hot spots that do not reflect very well and this can cause some errors.

We are consistent with Table 6.2 regarding the analysis of the differences. Focal waveforms from the slow D-Dot probe for 60^o four-feed arms: F, F1 and F2 are presented in Figure 6.20 and one can see the peak values for these focal waveforms in Table 6.4.

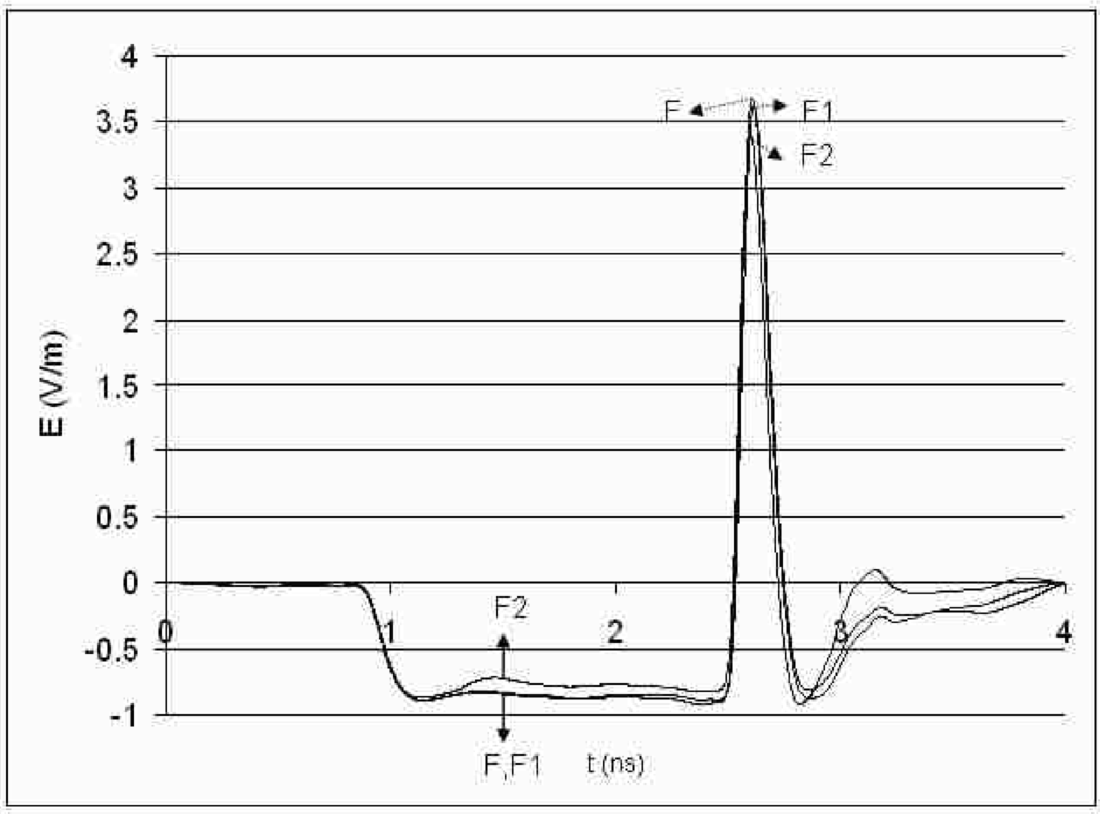

Figure 6.20: Focal waveforms from the slow D-Dot probe for 60^o four-feed arms: F (focal waveform), F1 (focal waveform with a piece of metal on the foam) , F2 (focal waveform with a piece of metal under the foam).

We can easily calculate the difference by comparing F and F2 from Table 6.4 and the resulting difference is 8%.

Table 6.4: Maximum values of F, F1 and F2.

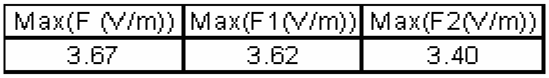

Max(F (V/m))	Max(F1(V/m))	Max(F2(V/m))
3.67	3.62	3.40

We compare our analytical, numerical and experimental focal waveforms for a two-arm prolate-spheroidal IRA in Figure 6.21.

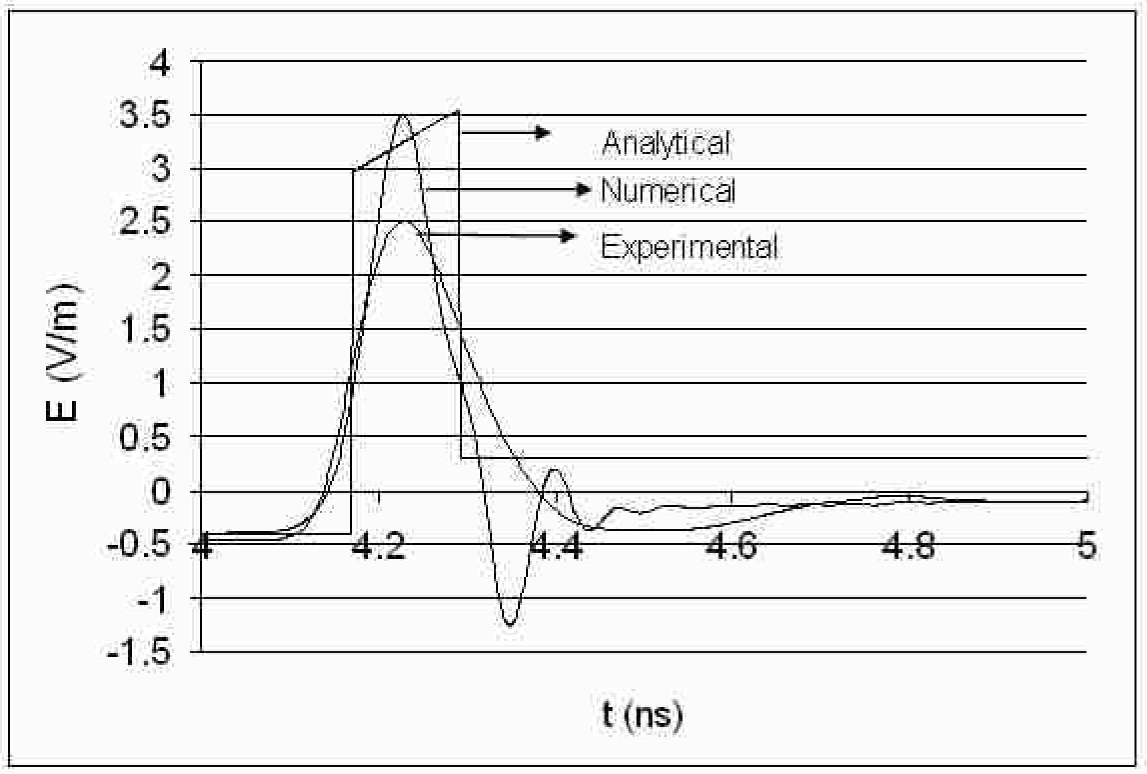

Figure 6.21: Analytical (slow D-Dot probe), numerical and experimental focal waveforms of a two-arm prolate-spheroidal IRA for tmr =119 ps.

One can see by comparing analytical, numerical and experimental focal waveforms that the prepulses agree very well. The analytical and numerical impulses' amplitudes agree as well. However, the experimental impulse amplitude is smaller than the others. It is also broader near the base. As discussed before, any misshape of the reflector may lead to this in the experiment. We have also a feed arm blockage effect that decreases the amplitude of the experimental impulse; however we did not see this effect in our numerical results. Our analytical result is based on an idealized assumption and it does not account for the feed arms. Finally, for all cases, the postpulse behaviors are different.

7 LENS DESIGN FOR A PROLATE-SPHEROIDAL IRA

7.1 Introduction

In this chapter, we discuss the design procedure for different types of dielectric lenses for better concentrating the fields at the second focus of a prolate-spheroidal IRA to increase the fields and decrease the spot size. We have a very fast and intense electromagnetic pulse to illuminate the target [3] which is located at the second focal point. One of the most important problems with concentrating the fields on the target is reflection. We have to deal with this reflection because the dielectric property of the target medium and the medium through which the incident wave propagates are different. The reflection of the pulse leads to a smaller field at the second focus where our target is buried. We discuss the addition of a lens to better match the wave to the target. We can obtain larger fields and smaller spot size [22].

To obtain better concentration at the target we can use different types of lenses. The transmission coefficient from one medium to the another one can be defined as

$$T = 2\left[1 + \varepsilon_{rt}^{1/2}\right]^{-1}, \tag{7.1}$$

where ε_{rt} is the relative permittivity of the target medium.

Suppose now that we have a lens in front of the target with relative permittivity

$$\varepsilon_{\ell} = \varepsilon_{rt}\,. \tag{7.2}$$

The fields from the reflector are transmitted with transmission coefficient given by

$$T_0 = 2\left[1+\varepsilon_{rt}^{1/2}\right]^{-1} . \tag{7.3}$$

We will have a slower wave speed and an enhancement factor which is an increase in the impulse portion of the focal waveform from [22] as

$$\begin{gathered} v = \left[\varepsilon_{r\ell}\varepsilon_0\mu_0\right]^{-1/2} = c\,\varepsilon_{r\ell}^{-1/2} , \\ F_0 = \varepsilon_{r\ell}^{1/2} = \varepsilon_{rt}^{1/2} . \end{gathered} \tag{7.4}$$

Thus, for the impulse part of the field we will have a net increase of

$$F_0\,T_0 = 2\left[1+\varepsilon_{rt}^{-1/2}\right]^{-1} . \tag{7.5}$$

Suppose now that we have a lens in front of the target with relative permittivity

$$1 < \varepsilon_{r\ell} < \varepsilon_{rt} . \tag{7.6}$$

We will have then two transmission coefficients and the total transmission coefficient can be defined as

$$T = T_1\,T_2 = 2\left[1+\varepsilon_{rt}^{1/2}\right]^{-1} 2\left[1+\left(\frac{\varepsilon_{rt}}{\varepsilon_{r\ell}}\right)^{1/2}\right]^{-1} = \frac{4}{\left(1+\varepsilon_{rt}^{1/2}\right)\left(1+\left(\frac{\varepsilon_{rt}}{\varepsilon_{r\ell}}\right)^{1/2}\right)} . \tag{7.7}$$

Finally, suppose we have a lens with a graded relative permittivity given by

$$r_1 \geq r_\ell \geq r_2 \,, \quad \varepsilon_{r\ell}(r_1) = 1 \,, \quad \varepsilon_{r\ell}(r_2) = \varepsilon_{rt} \,. \tag{7.9}$$

The wave propagating through this takes the same form as that of a wave in a transmission-line transformer. The high frequency early-time transfer function can be defined as [22]

$$\mathrm{T} = \left(\frac{\mathrm{Z}_0}{\mathrm{Z}_\mathrm{t}} \right)^{1/2} = \varepsilon_{\mathrm{rt}}^{-1/4} \,. \tag{7.10}$$

We still have the enhancement factor the transmission enhancement

$$\mathrm{F}_0 \mathrm{T} = \varepsilon_{\mathrm{rt}}^{+1/2} \varepsilon_{\mathrm{rt}}^{-1/4} = \varepsilon_{\mathrm{rt}}^{+1/4} \,. \tag{7.11}$$

The transmission enhancement of the lens, as discussed in [23] for an exponential variation of the characteristic impedance of the transmission line (for constant wave speed) along the line, is somewhat optimal. In this chapter we present different types of graded lenses for stronger focusing at the target.

The focal point is $z_0 = 37.5$ cm and the other parameters of the prolate-spheroidal IRA are defined in (4.1).

7.2 Calculating the Optimum Number of Layers for a Lens

In this section we calculate the optimum number of layers to obtain the required field at the focal point of a prolate-spheroidal IRA based on a plane-wave approximation. N layers of increasing dielectric constant lenses which have the same ratio of dielectric constant are considered for a prolate-spheroidal IRA that is based on Appendix A and [22]. The geometrical illustration of this design is presented in Figure 7.1.

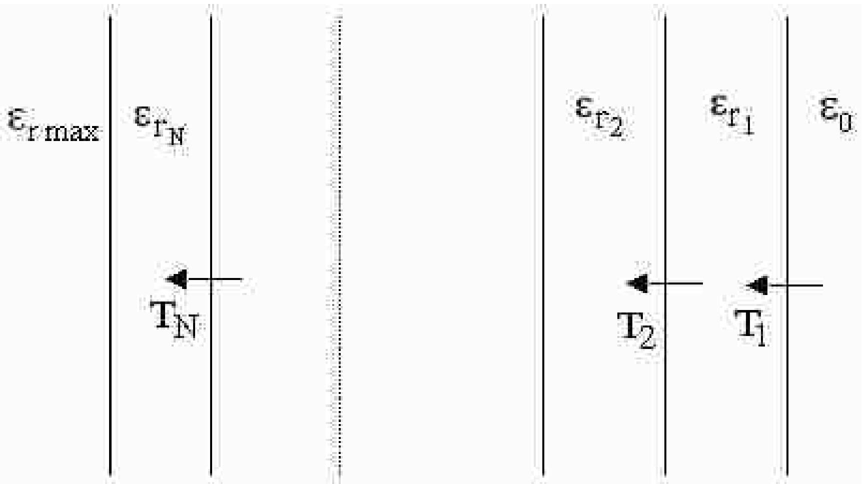

Figure 7.1: N layers of lens, dielectric constants and transmission coefficients.

The total transmission coefficient can be defined as

$$T_{total} = \prod_{1}^{N} T_n \,, \tag{7.1}$$

where T_n is the transmission coefficient between nth and nth+1st layer and it can be defined as

$$T_n = \frac{2Z_{n+1}}{Z_n + Z_{n+1}} = \frac{2\,\varepsilon_{r\,n+1}^{-1/2}}{\varepsilon_{r\,n}^{-1/2} + \varepsilon_{r\,n+1}^{-1/2}}\,. \tag{7.2}$$

The ratio of dielectric constant between subsequent layers are constrained to be the same,

$$\varepsilon_{\text{ratio}} = \varepsilon_{r_{n+1}} / \varepsilon_{r_n}\,. \tag{7.3}$$

For N layers

$$\left(\varepsilon_{r_{n+1}} / \varepsilon_{r_n}\right)^{N} = \varepsilon_{\text{ratio}}^{N} = \varepsilon_{r\,\max}\,. \tag{7.4}$$

Substituting (7.4) in (7.2), we have

$$T_n = \frac{2\left(\varepsilon_{r\,max}^{1/N}\right)^{-1/2}}{1 + \left(\varepsilon_{r\,max}^{1/N}\right)^{-1/2}}\,. \tag{7.5}$$

For N layers from (7.1)

$$T_{total} = \left(\frac{2\left(\varepsilon_{r\,max}^{1/N}\right)^{-1/2}}{1 + \left(\varepsilon_{r\,max}^{1/N}\right)^{-1/2}}\right)^{N}\,. \tag{7.6}$$

If we have a continuously increasing dielectric lens we have a total transmission coefficient defined in (7.10) as

$$T_{total} = \varepsilon_{r\,max}^{-1/4} . \tag{7.7}$$

If we have an infinite number of layers, (7.6) approaches (7.7). We should decide how many layers will be acceptable to obtain the closest transmission coefficient to the continuously increasing dielectric lens case.

Table 7.1: Transmission coefficients for different N and $\varepsilon_{r\,max}$.

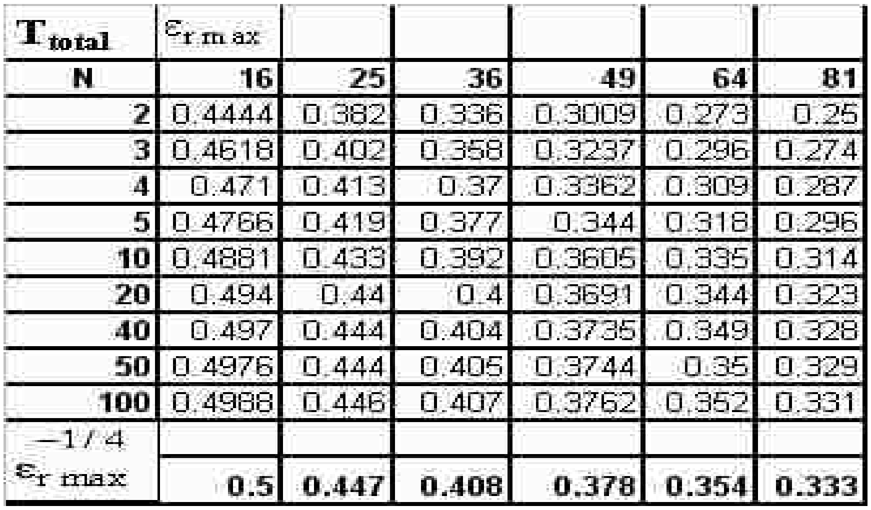

T_{total}	$\varepsilon_{r\,max}$					
N	**16**	**25**	**36**	**49**	**64**	**81**
2	0.4444	0.382	0.336	0.3009	0.273	0.25
3	0.4618	0.402	0.358	0.3237	0.296	0.274
4	0.471	0.413	0.37	0.3362	0.309	0.287
5	0.4766	0.419	0.377	0.344	0.318	0.296
10	0.4881	0.433	0.392	0.3605	0.335	0.314
20	0.494	0.44	0.4	0.3691	0.344	0.323
40	0.497	0.444	0.404	0.3735	0.349	0.328
50	0.4976	0.444	0.405	0.3744	0.35	0.329
100	0.4988	0.446	0.407	0.3762	0.352	0.331
$\varepsilon_{r\,max}^{-1/4}$	**0.5**	**0.447**	**0.408**	**0.378**	**0.354**	**0.333**

The number of layers depends on the sensitivity of the application accuracy. In general using more than 10 layers is not practical for manufacturing and we try to obtain the closest transmission coefficient to the continuously increasing case. From Table 7.1 one can see that, for 10 layers, N=10, T_{total} approaches close to the continuously increasing dielectric lens case. Even though 10 layers does not give us that much improvement if we compare it with N=2 layers, we took N=10 layers for our later calculations. One can easily decrease or increase the number of layers for specific applications. We took the maximum number of layers, which is N=10, that can be manufactured for later calculations.

7.3 Three Different Types of Graded Lens Design for a Prolate-Spheroidal IRA

The basic design considerations for the physical concept of three different types of increasing permittivity dielectric lens are considered. The focal point is $z_0 = 37.5$ cm and the other parameters of the prolate-spheroidal IRA are defined in (4.1). The lens is a half sphere (or half ball in mathematicians terms) and its radius is r_{max}, as shown in Figure 7.2.

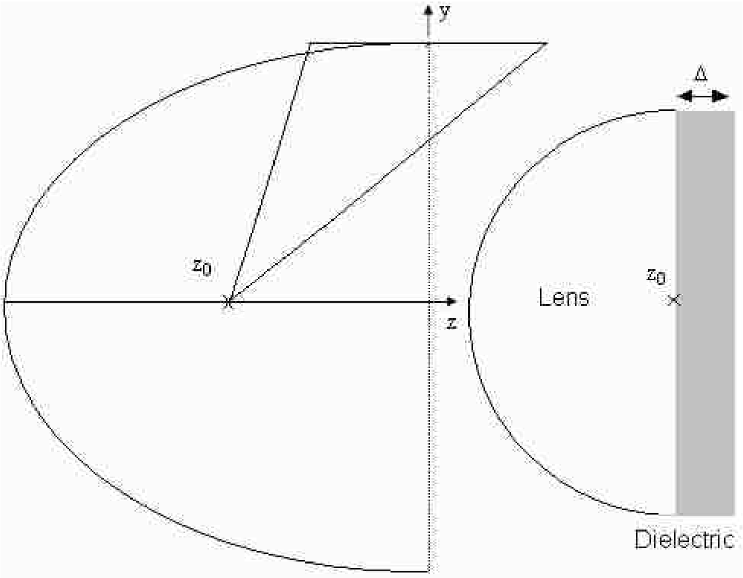

Figure 7.2: Addition of lens with prolate-spheroidal IRA geometry.

As discussed in [20] before, the exponential variation of the characteristic impedance of a transmission line along the line is optimal, provided that the speed of propagation is constant along the line. Some modification may be useful here since the speed varies inversely with the square root of the dielectric constant.

The lens relative permittivity is

$$\varepsilon_r(\mathrm{r}) = \begin{cases} 1 & \text{at } \mathrm{r} = \mathrm{r}_{\max} \\ \varepsilon_{r\max} & \text{at } \mathrm{r} = 0 \end{cases} . \tag{7.8}$$

7.3.1 Exponential Variation of ε_r

One suitable form for ε_r is an exponential function as

$$\varepsilon_r(r) = e^{q(r_{max}-r)} . \tag{7.9}$$

As we know at $r = 0$ the relative permittivity is $\varepsilon_{r=}\varepsilon_{r\,max}$ so

$$\begin{aligned} \varepsilon_{r\,max} &= e^{C_1(r_{max})}, \\ C_1 &= \frac{1}{r_{max}} ln(\varepsilon_{r\,max}). \end{aligned} \tag{7.10}$$

If we substitute (7.10) in (7.9), ε_r can be found as

$$\varepsilon_r(r) = e^{ln(\varepsilon_{r\,max})(1-\frac{r}{r_{max}})} . \tag{7.11}$$

The rise time is estimated as $t_\delta = 100\,ps$ the distance corresponding to this rise time is

$$\ell_\delta = c t_\delta = 3cm \tag{7.12}$$

in air.

The propagation distance of the wave from $r = r_{max}$ *to* $r = 0$ is

$$
\begin{aligned}
ct_{lens} &= c\int_{0}^{r_{max}} \frac{1}{v}\,dr = \int_{0}^{r_{max}} \varepsilon_r^{1/2}(r)\,dr = \int_{0}^{r_{max}} e^{\frac{1}{2}ln(\varepsilon_{r\,max})\left(1-\frac{r}{r_{max}}\right)}\,dr \\
&= (\varepsilon_{r\,max}^{1/2}-1)\frac{2\,r_{max}}{ln(\varepsilon_{r\,max})}.
\end{aligned}
\tag{7.13}
$$

The normalized ct_{lens} is

$$
\frac{ct_{lens}}{r_{max}} = (\varepsilon_{r\,max}^{1/2}-1)\frac{2}{ln(\varepsilon_{r\,max})}\ . \tag{7.14}
$$

The distance between the source and lens is $(0.375\,\mathrm{m} + \mathrm{r}_{\mathrm{max}})$.

After this design procedure we designed a lens that is matched to the target dielectric $\varepsilon_{r\,max}$. The thickness of the target dielectric material should be

$$
\Delta = n\frac{c\,t_{\delta}}{\sqrt{\varepsilon_{r\,max}}}\ ,\ n \geq 2\ , \tag{7.15}
$$

in order to minimize the effect of the reflected wave on the impulse term.

7.3.2 Compensated Incremental Speed (CIS) form of ε_r

As we mentioned before the exponential form assumes that the propagation speed is constant. However, it is not constant we need to compensate for this assumption. Let us assume we have a plane wave problem in an inhomogeneous (isotropic) slab with $\varepsilon_r(z)$ and set the relative change in wave impedance over a transit time $\Delta\tau$

$$\frac{\Delta ln(\varepsilon_r^{-1/2})}{\Delta\tau} = C_2 \tag{7.16}$$

with the wave impedance Z_c proportional to $\varepsilon_r^{-1/2}$. The distance based on the transit time can be written as

$$c\,d\tau = \varepsilon_r^{1/2}\,dz\,. \tag{7.17}$$

For a given $\Delta\tau$ the Δz decreases as $\varepsilon_r^{-1/2}$. For a given $\Delta\tau$ the change in $ln(\varepsilon_r^{-1/2})$ is independent of z and if we substitute (7.17) in (7.16) we obtain

$$\varepsilon_r^{-1/2}\,\frac{d\,ln(\varepsilon_r^{-1/2})}{dz} = C_2\,. \tag{7.18}$$

Integrating (7.18)

$$\begin{aligned} &\int \varepsilon_r^{-1/2} d\,ln(\varepsilon_r^{-1/2}) = \int e^{ln(\varepsilon_r^{-1/2})}\,d\,ln(\varepsilon_r^{-1/2}) = \int C_2\,dz \\ &\varepsilon_r^{-1/2} = C_2 z + C_3\,. \end{aligned} \tag{7.19}$$

We can define ε_r from (7.19) as

$$\varepsilon_r = \left(C_2 z + C_3\right)^{-2} = \begin{cases} 1 & at\ z = z_{max} \\ \varepsilon_{r\,max} & at\ z = 0 \end{cases}, \tag{7.20}$$

such that from (7.20)

$$C_2 = \frac{1-\varepsilon_{r\,max}^{-1/2}}{z_{max}}\ ,\ C_3 = \varepsilon_{r\,max}^{-1/2}\ . \tag{7.21}$$

Then, if we substitute (7.21) in (7.20) we have

$$\varepsilon_r = \left((1-\varepsilon_{r\,max}^{-1/2})\frac{z}{z_{max}} + \varepsilon_{r\,max}^{-1/2} \right)^{-2} . \tag{7.22}$$

How much time does the propagation of the wave take from r_{max} to the focal point in the lens? Substituting (7.22) in (7.14)

$$ct_{lens} = \int_0^{r_{max}} \varepsilon_r^{1/2}\ dr = \int_0^{r_{max}} \left((1-\varepsilon_{r\,max}^{1/2})\frac{r}{r_{max}} + \varepsilon_{r\,max}^{-1/2} \right)^{-1} dr\ . \tag{7.23}$$

Changing the variable of the integral as $\xi = r / r_{max}$, we obtain

$$ct_{lens} = r_{max}\int_0^1 \left((1-\varepsilon_{r\,max}^{-1/2})\xi + \varepsilon_{r\,max}^{-1/2} \right)^{-1} d\xi\ . \tag{7.24}$$

Let us change the variable of the integral as $\varsigma = (1-\varepsilon_{r\,max}^{-1/2})\xi + \varepsilon_{r\,max}^{-1/2}$

$d\,\varsigma = (1-\varepsilon_{r\,max}^{-1/2})\,d\xi$ and we will have normalized

$$ct_{lens} = \frac{r_{max}}{1-\varepsilon_{r\,max}^{-1/2}} \int_{\varepsilon_{r\,max}^{-1/2}}^{1} (\zeta)^{-1}\, d\zeta = \frac{1}{2}\frac{r_{max}}{1-\varepsilon_{r\,max}^{-1/2}}\ ln(\varepsilon_{r\,max})\ . \tag{7.25}$$

Then, we can find the normalized ct_{lens} is

$$\frac{ct_{lens}}{r_{max}} = \frac{1}{2} \frac{1}{1-\varepsilon_{r\,max}^{-1/2}} \, ln(\varepsilon_{r\,max}) . \tag{7.26}$$

7.3.3 Linear form of ε_r

The exponential variation and CIS form of ε_r are two different approaches having some advantages and disadvantages in terms of focusing. After these approaches we tried to use another approach, a linearly increasing form of ε_r. Let us assume we have a linear ε_r variation as

$$\varepsilon_r(r) = r / r_{max} + \varepsilon_{r\,max}\left(1 - r / r_{max}\right), \tag{7.27}$$

which satisfies (2.2), we can find the normalized propagation time of the wave from $r = r_{max}\ to\ r = 0$ as

$$\frac{ct_{lens}}{r_{max}} = \frac{1}{r_{max}} \int_0^{r_{max}} \varepsilon_r^{1/2}(r)\,dr = \int_0^{r_{max}} \left(r / r_{max} + \varepsilon_{r\,max}\left(1 - r / r_{max}\right)\right)^{1/2} dr . \tag{7.28}$$

Let us change the variable of this integral as $\zeta = r / r_{max}$ to obtain

$$\frac{ct_{lens}}{r_{max}} = \int_0^1 \left[\zeta + \varepsilon_{r\,max}(1-\zeta)\right]^{1/2} d\zeta . \tag{7.29}$$

We can also change this variable ζ as

$$\begin{aligned} \xi &= \zeta + \varepsilon_{r\,max}[1-\zeta] \\ d\xi &= d\zeta\left[1-\varepsilon_{r\,max}\right] \end{aligned} \quad . \tag{7.30}$$

Using (7.29),

$$\frac{ct_{lens}}{r_{max}} = \frac{1}{1-\varepsilon_{r\,max}} \int_{\varepsilon_{r\,max}}^{1} \xi^{1/2} d\xi = \frac{2}{3}(\varepsilon_{r\,max}-1)^{-1}(\varepsilon_{r\,max}^{3/2}-1). \tag{7.31}$$

7.3.4 Conclusion

A dielectric exponentially increasing dielectric constant, CIS, and linear increasing lens designs were discussed. One can see from Figure 7.3 that the wave propagates faster for the CIS form of ε_r. We can see from Figure 7.4 a-d) that if $\varepsilon_{r\,max}$ increases, the wave propagates slower as expected. $\varepsilon_{r\,max}$ varies from 1 to 81 (with 81 corresponding to water, which is the highest ε_r that is used in biological applications). If we increase $\varepsilon_{r\,max}$ from 36 to 81, the CIS design of ε_r has the deepest curvature. The focusing property of the lens increases from the CIS to the linear design because for the same $\mathrm{r}/\mathrm{r}_{\mathrm{max}}$ we have an increase in ε_r, we expect the lens to become more effective. Also from [22] if we increase ε_r the spot size decreases while the wave impedance decreases and the amplitude of the waveform increases by a factor of $\varepsilon_r^{1/4}$. This rough calculation has to extend out some distance from the target for effective focusing to occur and thus requires more detailed calculations.

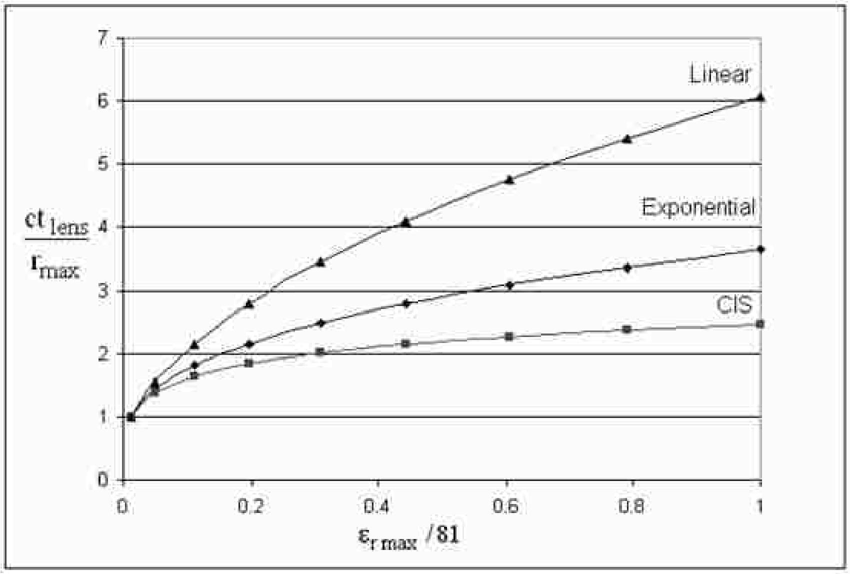

Figure 7.3: ct_{lens} / r_{max} for linear, exponential and CIS forms of ε_r.

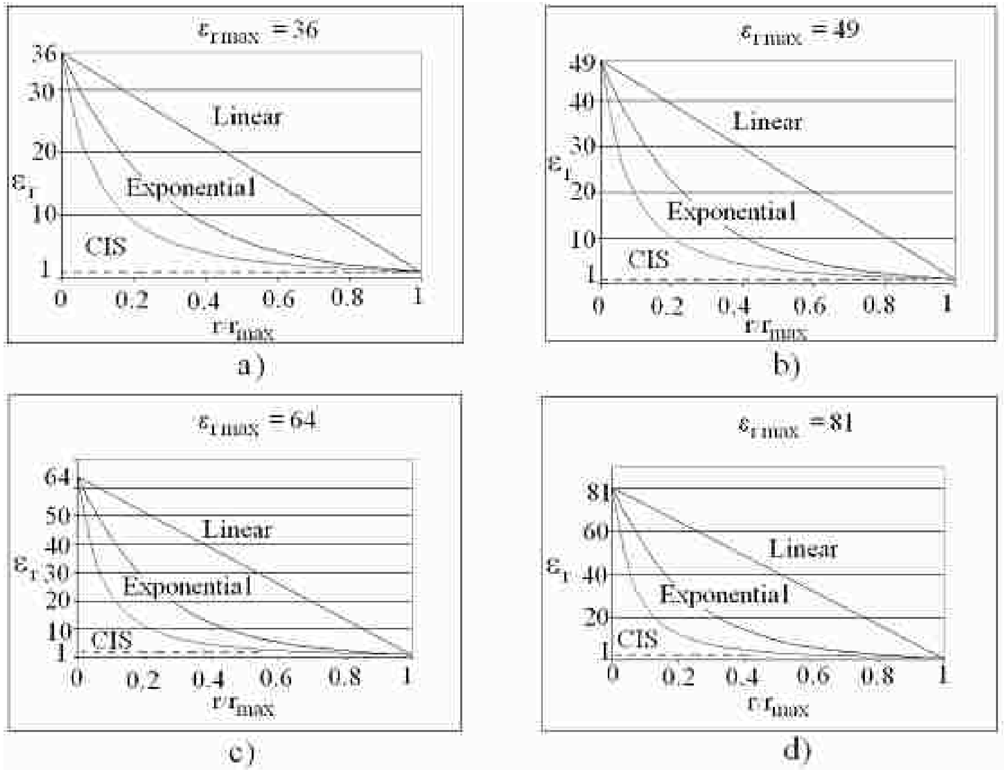

Figure 7.4: ε_r values for linear, exponential and CIS forms of ε_r for different $\varepsilon_{r\,max}$ with respect to r / r_{max}.

7.4 Spatially Limited Exponential Lens Design for Better Focusing an Impulse

A spatial limited exponential lens design is discussed and an analytical formulation has been used to examine the pulse droop in order to minimize it.

A formulation in [23] has been used to examine the pulse droop for a transmission line with an exponentially tapered impedance profile. We wish to minimize this droop, or ask how long the transmission line should be for a given droop. The exponentially tapered transmission line has an optimal transfer function in terms of early time voltage gain and improved droop characteristics. We apply this result to an exponentially tapered dielectric constant of a focusing lens. We find the required lens dimensions for a given droop. The lens geometry and incoming spherical wave are presented in Figure 7.5. Our calculations are based on a one-dimensional plane-wave approximation (Figure 7.6). This will not directly give an estimate of spot size, only the transmission/reflection by the lens. Other considerations also apply [22].

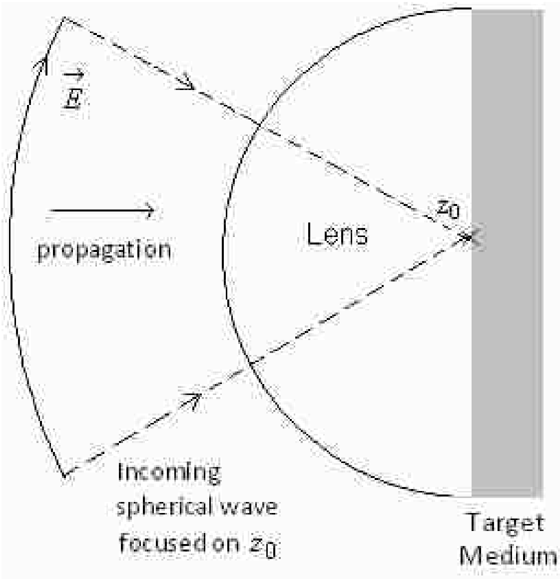

Figure 7.5: Lens geometry and incoming spherical wave.

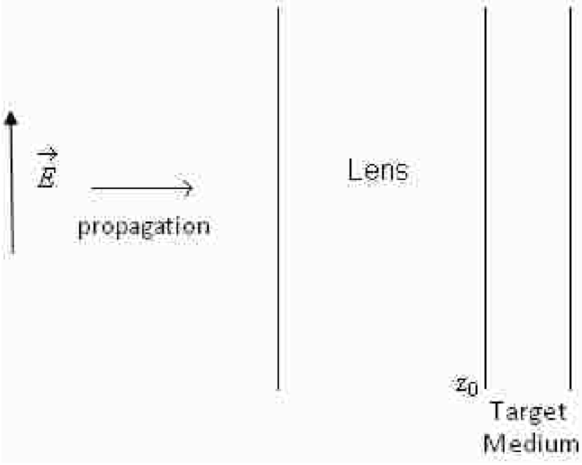

Figure 7.6: Equivalent plane wave geometry.

7.4.1 Equivalent Transmission-Line Model (One Dimensional) of Lens

As discussed in [23], the exponentially tapered lens has a minimized droop and the optimal transfer function for the case of uniform propagation speed. Here we adapt this solution to a dielectric lens, noting that the propagation speed slows as the wave propagates in higher-permittivity media. This model does not include any information about spot size.

We can define the lens wave impedance as follows: z =spatial coordinate, ζ = modified space coordinate, we have a new coordinate where the wave propagates with a constant v_1 speed and has an exponential wave impedance variation through the lens. We use a plane wave approximation and this approximation is valid up to the case when the wavelength is still small compared to the cross section of the beam

$$\frac{\zeta}{c} = \text{transit time to } z \text{ and hence } \zeta . \tag{7.32}$$

Let

$$Z(\zeta) = Z_1 \, e^{-\zeta / \zeta_0} , \tag{7.33}$$

where Z_1 is the wave impedance at the beginning of the lens; which is $Z_0 = 377\,\Omega$ in our case.

$$Z_2 = Z_1 \, e^{-\zeta_{max} / \zeta_0} , \tag{7.34}$$

where Z_2 is the wave impedance at the end of the lens.

$$Z(\zeta) = \left[\frac{\mu_0}{\varepsilon(\zeta)}\right]^{1/2} = Z_1\, \varepsilon_r^{-1/2}(\zeta)\,. \tag{7.35}$$

The propagation speed can be defined as

$$\mathrm{v} = \frac{1}{\left[\mu_0\, \varepsilon(\zeta)\right]^{1/2}} = \mathrm{v}_1\, \varepsilon_r^{-1/2}(\zeta)\,, \tag{7.36}$$

where v_1 is the propagation speed before the lens, which is typically c.

The transit time through the lens can be defined as

$$t_\zeta \equiv t_z \equiv \int_0^z \mathrm{v}^{-1}(z')\, dz' = \int_0^\zeta \mathrm{v}_1^{-1}\; d\zeta = \frac{\zeta}{\mathrm{v}_1}\,. \tag{7.37}$$

Taking the derivative of both sides of (7.37), we have

$$\frac{dt}{d\zeta} = \mathrm{v}_1^{-1} = \mathrm{v}^{-1}(\mathrm{z})\frac{dz}{d\zeta}\,,$$

$$\frac{dt}{dz} = \mathrm{v}^{-1}(\mathrm{z})\,, \tag{7.38}$$

$$\frac{d\zeta}{dz} = \frac{\mathrm{v}_1}{\mathrm{v}(\mathrm{z})} = \varepsilon_r^{1/2}(\zeta) = e^{\zeta_{max}/\zeta_0}\,.$$

Using (7.38) to solve for the spatial coordinate *z* in terms of modified space coordinate ζ can be find as

$$z = \int_0^\zeta \varepsilon_r^{-1/2}(\zeta')\, d\zeta'\,. \tag{7.39}$$

From (7.33) and (7.35) we can write (7.39) as

$$z = \int_0^{\zeta} e^{-\zeta'/\zeta_0}\, d\zeta' = \zeta_0 \left[1 - e^{-\zeta/\zeta_0}\right]. \tag{7.40}$$

We can see from (7.40) as $\zeta \to \infty$, $z \to \zeta_0$ and this does not continue to grow. This gives us a spatially limited lens. This is convenient for purposes of implementation.

The wave propagation can be described by the source-free telegrapher equations ((2.3) in [23]). We can transform the 1D wave equation to an equivalent ζ space coordinate as

$$\begin{aligned} \frac{dE(\zeta,s)}{d\zeta} &= -\frac{\mu_0}{Z_0} Z_0 e^{-\zeta/\zeta_0}\, H, \\ \frac{dH(\zeta,s)}{d\zeta} &= -\frac{\varepsilon_r \varepsilon_0}{Z_0} Z_0 e^{-\zeta/\zeta_0}\, E = -\frac{\varepsilon_0}{Z_0} Z_0 e^{\zeta/\zeta_0}\, E. \end{aligned} \tag{7.41}$$

7.4.2. Solution of the Transmission-Line Equations

We solve an equivalent problem of [23], but instead of an increase in the transmission-line impedance we have a decrease in wave impedance, but the equations in [23] still apply.

One can define the transmission coefficient for high T_h and low frequency T_ℓ as follows

$$T_h = \left[\frac{Z_2}{Z_1}\right]^{1/2}, \quad T_\ell = \frac{2Z_2}{Z_1 + Z_2} \tag{7.42}$$

Calculate the difference between these two coefficients as

$$T_h - T_\ell = \frac{Z_2^{1/2}\left[Z_1 + Z_2\right] - 2Z_2 Z_1^{1/2}}{Z_1 + Z_2} = \frac{Z_2^{1/2}\left[Z_1^{1/2} - Z_2^{1/2}\right]^2}{Z_1 + Z_2} > 0 \ . \tag{7.43}$$

This is always positive except at $Z_1 = Z_2$. Thus, there is a droop (positive, i.e. a decrease) from initial to final value for both increasing and decreasing impedances. The impedance is decreasing but there is still a droop.

We can use the exact solution of the transfer function in (3.8) of [23],

$$\tilde{T} = e^{S+G}\left[cosh\left(\left(S^2 + G^2\right)^{1/2}\right) + \frac{S}{\left(S^2 + G^2\right)^{1/2}} sinh\left(\left(S^2 + G^2\right)^{1/2}\right)\right]^{-1} , \tag{7.44}$$

where S is the normalized complex frequency

$$S = s\,t_{\zeta\ max} = (\Omega + j\omega)t_{\zeta\ max} \,. \tag{7.45}$$

The high-frequency gain is defined in (3.4) of [23] as

$$g = e^G = \sqrt{Z_2 / Z_1} = \varepsilon_r^{-1/4} . \tag{7.46}$$

One can define the transit, normalized and droop time ((3.11) of [23]) parameters as follows

$$\begin{aligned} &t_{\zeta\ max} \equiv \zeta_{max} / \mathrm{v}_1 && \text{transit time through lens,} \\ &\tau \equiv t / t_\zeta && \text{normalized time,} \\ &\tau_d = 2\ ln^{-2}(g) && \text{normalized droop time} \\ &\quad = t_d / t_{\zeta\ max} \,. && \end{aligned} \tag{7.47}$$

t_d is the droop time, the step-response form is defined as (3.13) of [23]

$$R(\tau) = g\left[1 + \tau / \tau_d + O(\tau^2)\right] \quad as \quad \tau \to 0. \tag{7.48}$$

7.4.3 Example

Now we can calculate the lens thickness for a given dielectric target permittivity $\varepsilon_{r\,max}$. Setting $t / t_d = 0.05$ *and* 0.1, and using a $t = 100\,\text{ps}$ pulse width (maximum time of interest) from (7.45)

$$\begin{aligned} &t_d = 2\text{ ns} \;\; and \;\; 1\text{ns}, \\ &\zeta_{max} = \frac{2\, t_d}{ln^2(g)}. \end{aligned} \tag{7.49}$$

From (7.34) and (7.47)

$$\begin{aligned} &\frac{Z_2}{Z_1} = \varepsilon_{r\,max}^{-1/2} = e^{-\zeta_{max} / \zeta_0}, \\ &\zeta_0 = \frac{c\, t_d\, ln^2(g)}{ln(\varepsilon_{r\,max})} \quad \text{(meters)}. \end{aligned} \tag{7.50}$$

Substituting (7.49) in (7.40) we have

$$z_{max} = \zeta_0\left[1 - e^{-\zeta_{max} / \zeta_0}\right] = \frac{c\, t_d\, ln^2(g)}{ln(\varepsilon_{r\,max})}\left[1 - \varepsilon_{r\,max}^{-1/2}\right] \quad \text{(meters)}. \tag{7.51}$$

7.4.4 Conclusion

We might design a spatially limited exponential lens based on [23]. This lens is designed for a biological application [1]. From (7.51) we can find the z_{max} values for different biological tissues, which are summarized in Table 7.2.

Table 7.2 Design parameter values for different biological tissues [24,25].

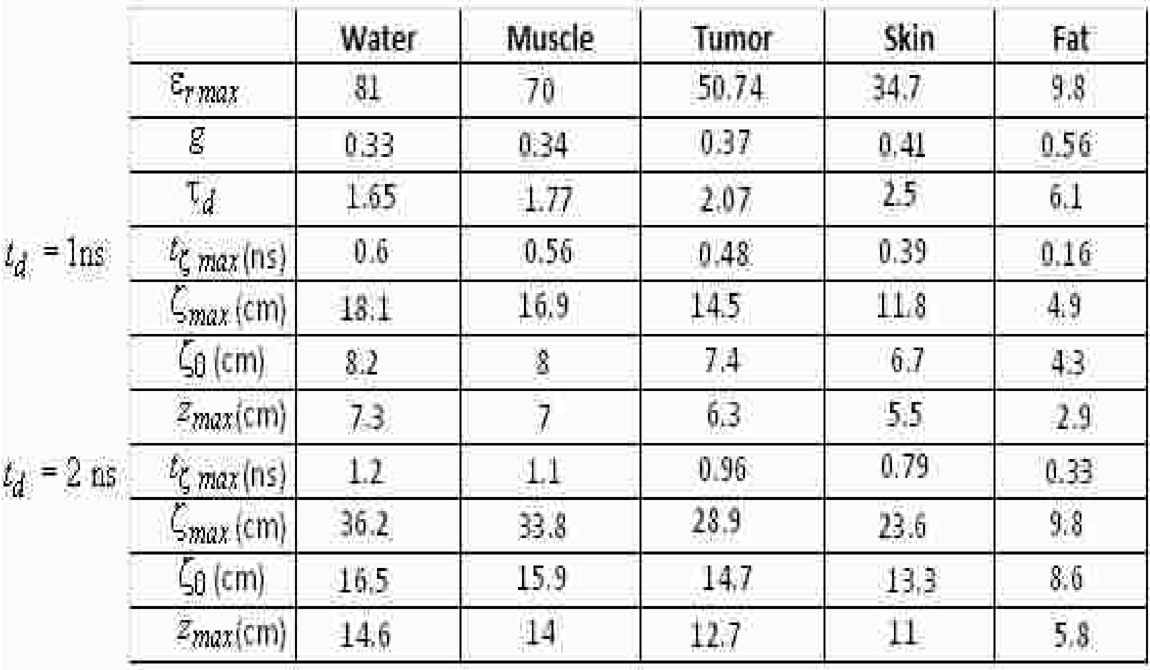

		Water	Muscle	Tumor	Skin	Fat
	$\varepsilon_{r\,max}$	81	70	50.74	34.7	9.8
	g	0.33	0.34	0.37	0.41	0.56
	τ_d	1.65	1.77	2.07	2.5	6.1
t_d = 1ns	$t_{\zeta\,max}$(ns)	0.6	0.56	0.48	0.39	0.16
	ζ_{max}(cm)	18.1	16.9	14.5	11.8	4.9
	ζ_0 (cm)	8.2	8	7.4	6.7	4.3
	z_{max}(cm)	7.3	7	6.3	5.5	2.9
t_d = 2 ns	$t_{\zeta\,max}$(ns)	1.2	1.1	0.96	0.79	0.33
	ζ_{max}(cm)	36.2	33.8	28.9	23.6	9.8
	ζ_0 (cm)	16.5	15.9	14.7	13.3	8.6
	z_{max}(cm)	14.6	14	12.7	11	5.8

One can see from Table 7.2 that, if we have lower dielectric constant for target biological tissue, we need a smaller lens. This is not the only consideration. A larger dielectric constant in the lens exit results in a smaller spot size and higher fields. The smaller spot size concentrates the energy in the vicinity of the skin cancer.

One can find how ε_r changes as a function of ζ and z from (7.40) and (7.50)

$$
\begin{aligned}
&\varepsilon_r(\zeta) = e^{2\zeta/\zeta_0}\,,\\
&\varepsilon_r(z) = \left(\frac{\zeta_0}{\zeta_0 - z}\right)^2.
\end{aligned}
\qquad (7.52)
$$

Let us consider $t_d = 1$ ns and find $\varepsilon_r(\zeta)$ and $\varepsilon_r(z)$ with respect to ζ and z for different dielectric tissues. These are presented in Figures 7.7 and 7.8.

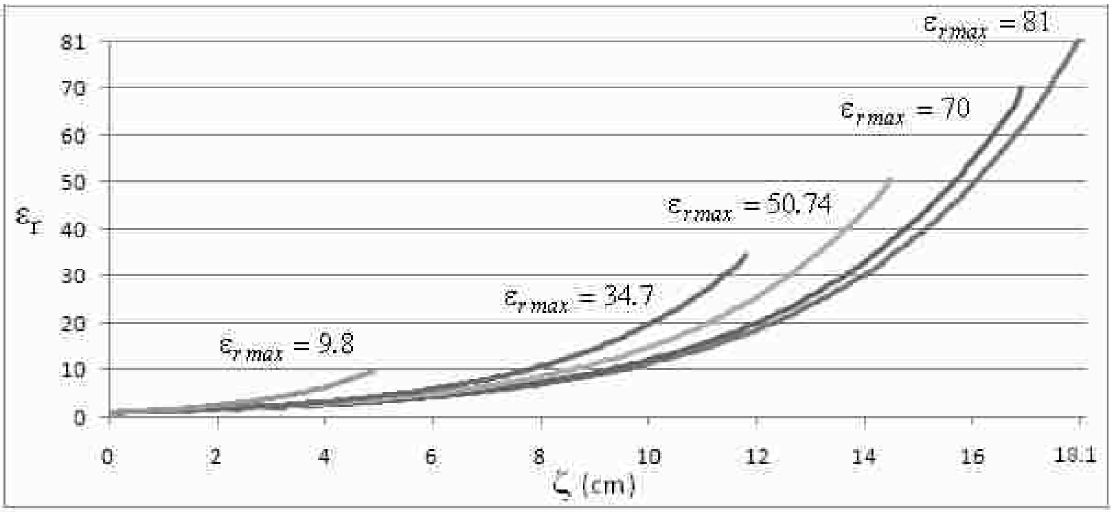

Figure 7.7: $\varepsilon_r(\zeta)$ values for different dielectric tissues.

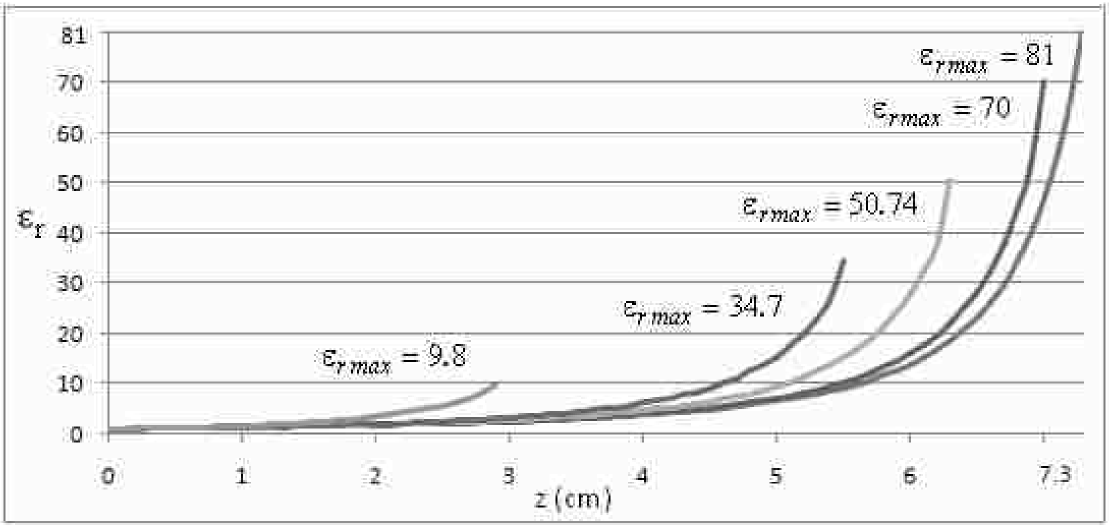

Figure 7.8: $\varepsilon_r(z)$ values for different dielectric tissues.

The compression of the coordinates for $t_d = 1$ ns and $\varepsilon_{r\ \max} = 81$ is presented in Figure 7.9.

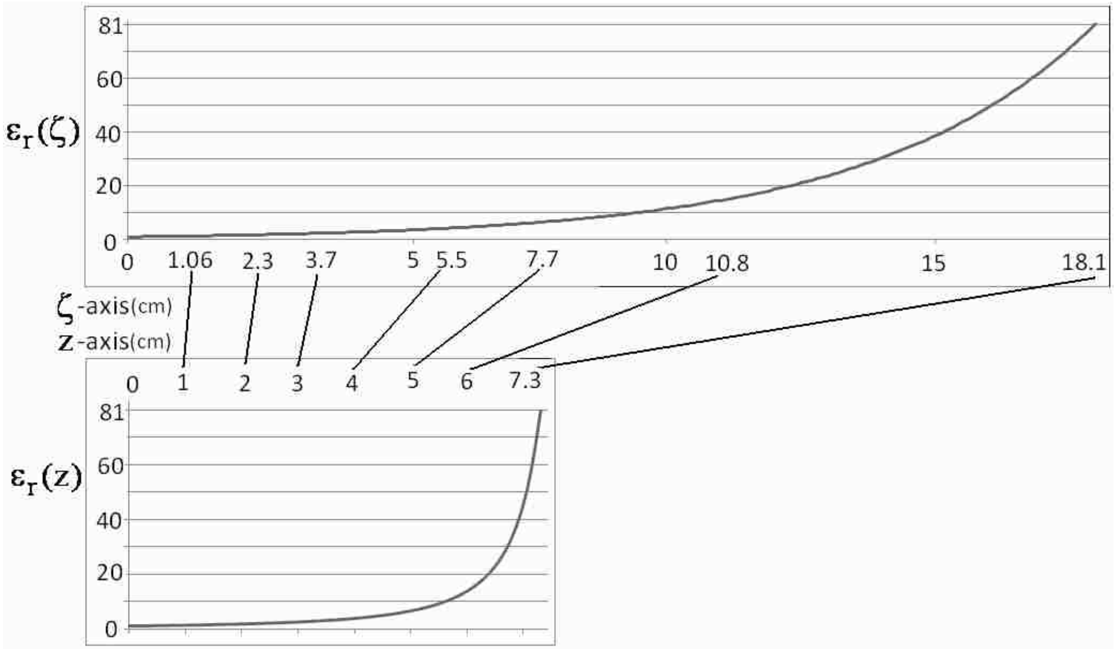

Figure 7.9: Compression of the coordinates for $t_d = 1$ ns and $\varepsilon_{r\ \max} = 81$.

7.5 Lens Design for Incoming Spherical Wave

In this section an alternate lens design procedure is discussed to obtain better focusing from a prolate-spheroidal in which the lens is not a sphere. This is an extension of Section 7.2 and the lens design considerations are based on [26]. N layers of an increasing dielectric lens, which have the same ratio of dielectric constants between adjacent layers, are considered for a prolate-spheroidal IRA. Instead of using a half-spherical lens, a new approach is proposed for incoming spherical waves to obtain better focusing for a prolate-spheroidal IRA.

7.5.1 Design Considerations

10 layers of increasing-dielectric-constant lens are used based on the calculations in Section 7.2. We use the same ratio of dielectric constant between subsequent layers as

$$\begin{aligned} &\varepsilon_{ratio} = \varepsilon_{r_{n+1}} / \varepsilon_{r_n} \ , \ \left(\varepsilon_{r_{n+1}} / \varepsilon_{r_n}\right)^N = \varepsilon_{ratio}^{N} = \varepsilon_{r\,max} \ , \\ &\varepsilon_{ratio} = \varepsilon_{r\,max}^{1/N} \ . \end{aligned} \tag{7.53}$$

We use N=10 layers and $\varepsilon_{r\max} = 81$ for the worst case scenario for biological applications. We start from free space $\varepsilon_r = 1$ and our target dielectric is $\varepsilon_{r\max} = 81$ and $\varepsilon_{\text{ratio}} = 1.55$ between subsequent layers. The first shell of the lens for incoming spherical wave is illustrated in Figure 7.10.

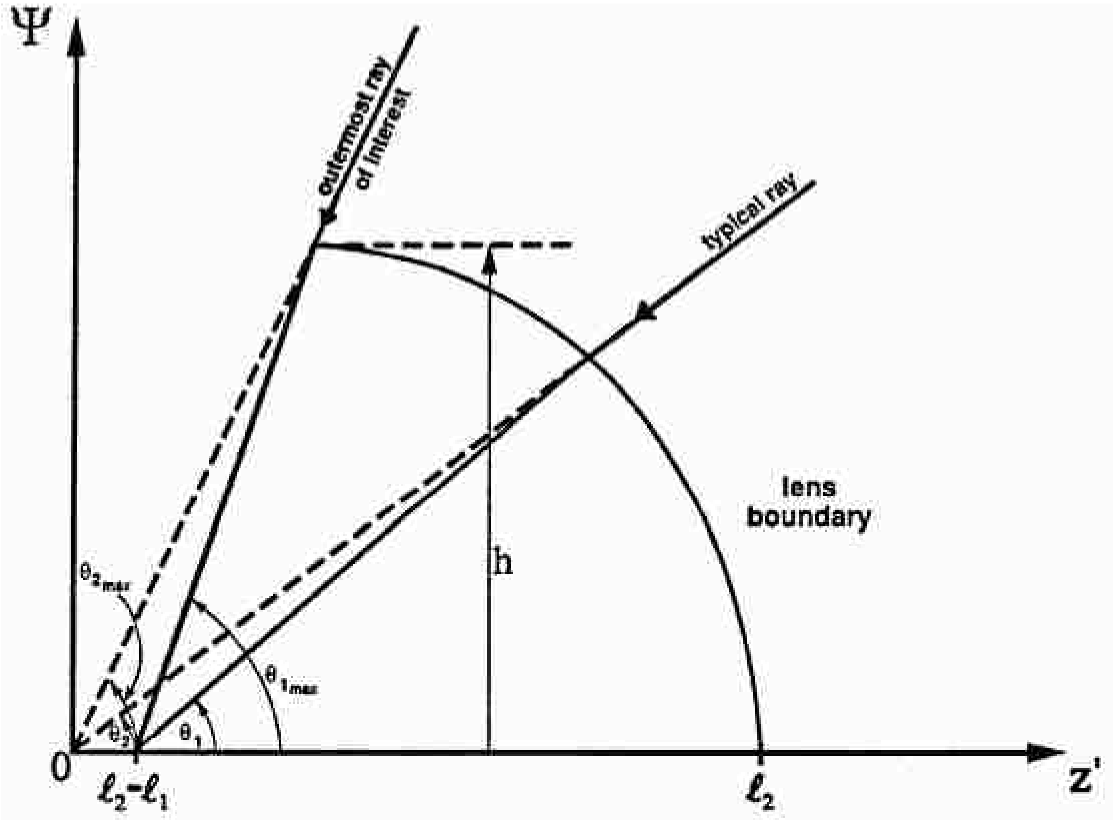

Figure 7.10: Lens for incoming spherical wave [26].

In Figure 7.10

$$\theta_{2\,max} = arctan(b / z_0) \;,\; 0 \le \theta_2 \le \theta_{2\,max}. \tag{7.54}$$

Equation (7.54) represents the range of interest of angles for the incoming wave from the prolate-spheroidal IRA which has the dimensions as given in [16]. From (7.54) and (7.55) for the first shell $\theta_{2\,max} = 53.13^o$. Inside the lens the rays change their direction to the angle of θ_1 with respect to the z'-axis and $\theta_{1\,max} \le \pi / 2$ for geometrical design purposes. ℓ_1 *and* ℓ_2 are the distances on the z'-axis, h is the height of the lens. The normalized ℓ_1 *and* ℓ_2 parameters are defined from (4.7) in [26] as

$$\frac{\ell_1}{h}=\frac{sin(\theta_{1max}-\theta_{2max})+\varepsilon_r^{1/2}\,sin(\theta_{2max})-sin(\theta_{1max})}{(\varepsilon_r^{1/2}-1)\,sin(\theta_{1max})\,sin(\theta_{2max})},$$

$$\frac{\ell_2}{h}=\frac{\varepsilon_r^{1/2}\left[sin(\theta_{1max}-\theta_{2max})+sin(\theta_{2max})\right]-sin(\theta_{1max})}{(\varepsilon_r^{1/2}-1)\,sin(\theta_{1max})\,sin(\theta_{2max})}. \qquad (7.55)$$

To find θ_2 as a function of θ_1 a quadratic equation in either $cos(\theta_2)$ or $sin(\theta_2)$ can be solved from (4.8-5.10) in [26] as

$$cos(\theta_2)=\frac{AB sin^2(\theta_1)+\left|B cos(\theta_1)-A\varepsilon_r^{1/2}\right|\sqrt{\left[B^2-2AB\varepsilon_r^{1/2}cos(\theta_1)+A\varepsilon_r\right]-A^2 sin^2(\theta_1)}}{B^2-2AB\varepsilon_r^{1/2}cos(\theta_1)+A\varepsilon_r},$$

$$sin(\theta_2)=\frac{A(A\varepsilon_r^{1/2}-B cos(\theta_1))+\left|B\right| sin(\theta_1)\sqrt{\left[B^2-2AB\varepsilon_r^{1/2}cos(\theta_1)+A\varepsilon_r\right]-A^2 sin^2(\theta_1)}}{B^2-2AB\varepsilon_r^{1/2}cos(\theta_1)+A\varepsilon_r}, \qquad (7.56)$$

$$A=(\ell_2/\ell_1)-1\ ,\ B=(\ell_2/\ell_1)-\varepsilon_r^{1/2}.$$

A lens boundary curve can be defined by the coordinates of z' and Ψ as a function of θ_1 and θ_2 from (4.11) and (4.12) in [26] as

$$\frac{z'}{h}=\frac{(\ell_2-\ell_1)/h\,tan(\theta_1)}{tan(\theta_1)-tan(\theta_2)}$$

$$\frac{\Psi}{h}=\frac{z}{h}tan(\theta_2)=\frac{(\ell_2-\ell_1)/h\,tan(\theta_1)tan(\theta_2)}{tan(\theta_1)-tan(\theta_2)}. \qquad (7.57)$$

This approach is just for the first shell, but we can expand it to the other shells. $\varepsilon_r = \varepsilon_{ratio} = 1.55$ and we will have different $\ell_1, \ell_2, \theta_{1max}$ *and* θ_{2max} for each layer.

We can define a new coordinate system which is centered at $z = z_0$. We will call this system z' and it can be defined as

$$z' / h = -(z - z_0) / h. \tag{7.58}$$

The IRA and lens geometry are presented in Figure 7.11. The angles of $\theta_{1\max}$ and $\theta_{2\max}$ are in given Figure 7.12

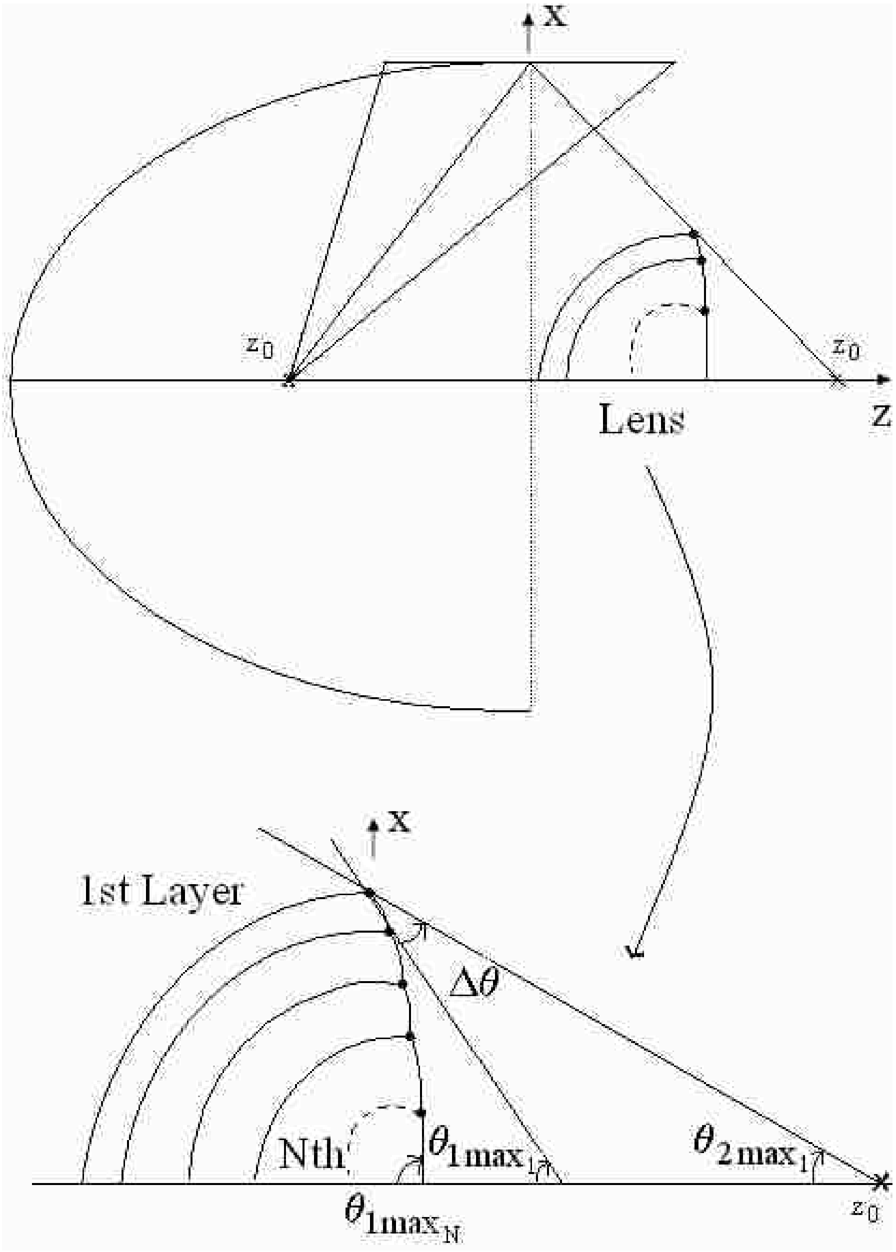

Figure 7.11: IRA and lens geometry.

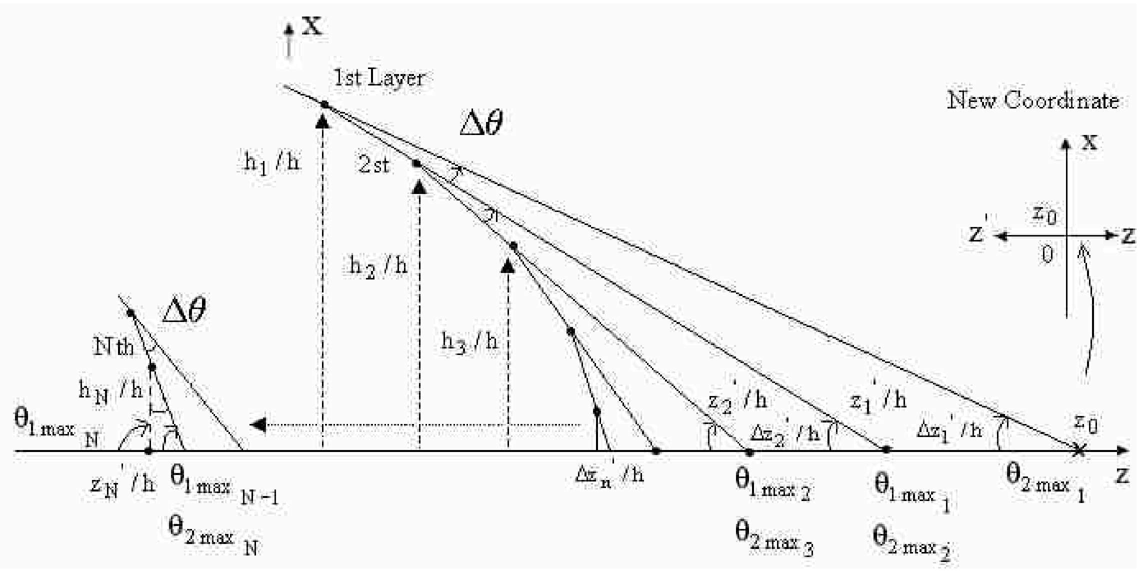

Figure 7.12: $\theta_{1\max}$ and $\theta_{2\max}$ values.

We use N=10 layers and $\Delta\theta$ is the change in the angle as one goes from one layer to the next. This is constant and is given by

$$\Delta\theta = (\theta_{1max_N} - \theta_{2max_1}) / N . \tag{7.59}$$

We design the lens for two different $\theta_{1max_{10}}$ angles as:

$$\theta_{1max_{10}} = \begin{cases} 90^o\,(\pi/2) \\ 85^o \end{cases} . \tag{7.60}$$

For the $\pi/2$ case $\Delta\theta = 3.7^o$ and for the 85^o case $\Delta\theta = 3.2^o$. $\Delta z_n{}' / h$ is the normalized distance between each layer-beginning point on the z'-axis. $z_n{}' / h$ is the sum of the n distances on the z'-axis which is shown in Figure 7.12.

7.5.2 Concluding Remarks for the Lens Design for Incoming Spherical Wave

We have designed a lens for incoming spherical waves to obtain better focusing from a prolate-spheroidal IRA. This design is based on the same procedure as in [26].In this design, however, just a single layer was used. We extended this design to N=10 layers. In this case we have different ℓ_1 / h ,ℓ_2 / h ,θ_{1max}, θ_{2max} , h_n / h, and z_n' / h . We calculated these values for the first layer. Then we correct the values for the other layers.

First we calculate the Ψ / h and z' / h values for the first layer, then for the second layer we calculate Ψ / h and z' / h. We correct them by multiplying with $h_{corrected} = h_n / h$ value, then we add $\Delta z_n' / h$ for each layer to find the corrected $\mathrm{z}_\mathrm{n}' / \mathrm{h}$ values at that layer.

As one can see from Figures 7.13 and 7.14, for $\theta_{1max_{10}} = 85^\circ$ case we obtain better focusing. We call *h* the radius of the shell, it is a universal normalization parameter. But this calculation is not determining h because it is an optical calculation (infinite frequency). To determine how large *h* should be is a difficult problem. Clearly *h/c* must be much greater than the focus pulse width at the focus, and the rise-time of the incoming wave, otherwise it does not focus, $\lambda <<$ other dimensions of the lens. *h* should be smaller than the radius of the reflector as well

$$ct_\delta = 3\,cm << h < b = 50\ cm. \tag{7.61}$$

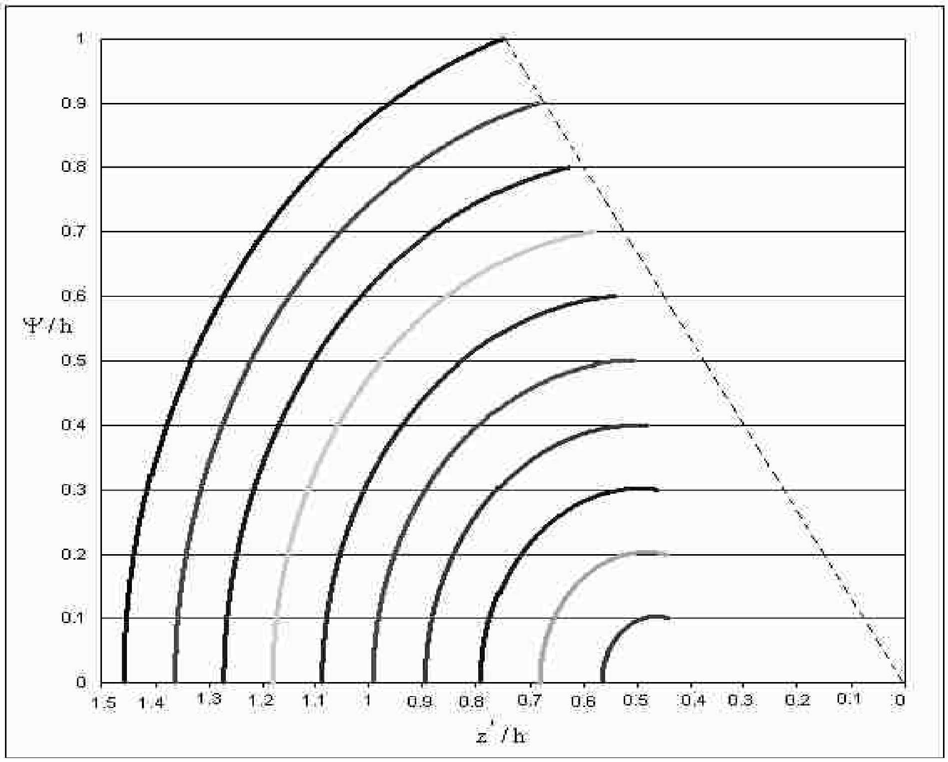

Figure 7.13: Ψ / h vs z' / h for $\theta_{1\max_{10}} = \pi / 2$.

Table 7.3: h_n / h, $\Delta z_n' / h$, z_n' / h, θ_{1max}, and θ_{2max} values for $\theta_{1max_{10}} = \pi / 2$.

Layer	h_n / h	$\Delta z_n' / h$	z_n' / h	$\theta_{1\max}$	$\theta_{2\max}$
1	1.0	0.096	0.000	0.992	0.927
2	0.9	0.079	0.096	1.056	0.992
3	0.8	0.066	0.175	1.120	1.056
4	0.7	0.054	0.241	1.185	1.120
5	0.6	0.044	0.295	1.249	1.185
6	0.5	0.035	0.339	1.313	1.249
7	0.4	0.027	0.374	1.378	1.313
8	0.3	0.020	0.401	1.442	1.378
9	0.2	0.013	0.421	1.506	1.442
10	0.1	0.006	0.434	1.571	1.506

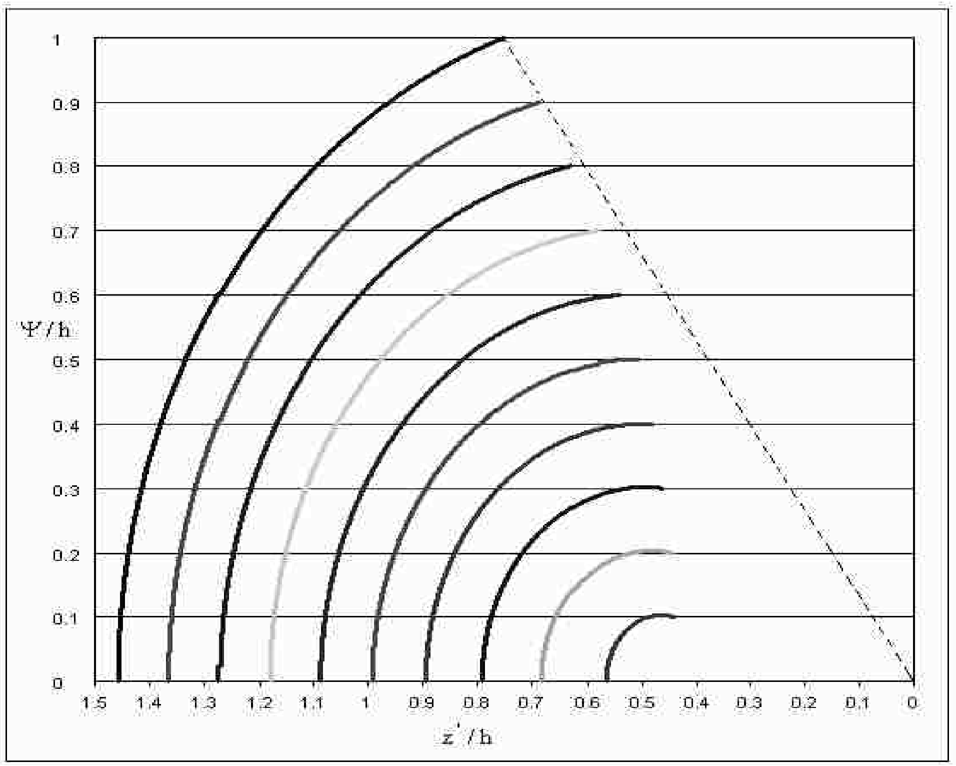

Figure 7.14: Ψ / h and z' / h for $\theta_{1max_{10}} = 85^o$.

Table 7.4: h_n / h, $\Delta z_n' / h$, z_n' / h, θ_{1max}, and θ_{2max} values for $\theta_{1max_{10}} = 85^o$.

Layer	h_n / h	$\Delta z_n' / h$	z_n' / h	θ_{1max}	θ_{2max}
1	1.0	0.096	0.000	0.983	0.927
2	0.9	0.079	0.096	1.039	0.983
3	0.8	0.066	0.175	1.094	1.039
4	0.7	0.054	0.241	1.150	1.094
5	0.6	0.044	0.295	1.205	1.150
6	0.5	0.035	0.339	1.261	1.205
7	0.4	0.027	0.374	1.317	1.261
8	0.3	0.020	0.401	1.372	1.317
9	0.2	0.013	0.421	1.428	1.372
10	0.1	0.006	0.434	1.484	1.428

7.5.3 Lens Design for Incoming Spherical Wave for Different Biological Dielectric Tissues

Five different biological dielectric tissues are used as different target dielectrics and we try to obtain better focusing from a prolate-spheroidal IRA for an incoming spherical wave from the reflector for these tissues. This subsection is an extension of the previous one. We use 5 different target dielectric tissues comprising water, muscle, tumor, skin and fat. Ten layers of an increasing dielectric constant lens that have the same ratio of dielectric constants between adjacent layers are considered for a prolate-spheroidal IRA.We use the same ratio of dielectric constant between subsequent layers as

$$\varepsilon_{ratio} = \varepsilon_{r\,max}^{1/N} , \tag{7.62}$$

where $\varepsilon_{r\,\max}$ and $\varepsilon_{\mathrm{ratio}}$ values for different human tissues are presented in Table 7.5.

Table 7.5: $\varepsilon_{\mathrm{ratio}}$ and $\varepsilon_{r\,\max}$ values for different human tissues [24,25].

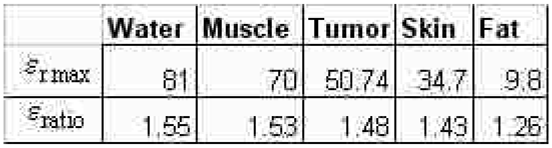

	Water	Muscle	Tumor	Skin	Fat
$\varepsilon_{r\,max}$	81	70	50.74	34.7	9.8
ε_{ratio}	1.55	1.53	1.48	1.43	1.26

A lens is designed for incoming spherical waves to obtain better focusing from a prolate-spheroidal IRA for different dielectric human tissues. We obtain better focusing for the higher dielectric lens. Ψ / h vs z' / h values for $\theta_{1\,max_{10}} = \pi / 2$ and 85^o for different $\varepsilon_{r\,\max}$ are presented in Figure 3.1 and Figure 3.2. One can see from Figure 7.15 and Figure 7.16 that for smaller $\varepsilon_{r\,max}$, the first shell moves left. We have fixed the vertical (Ψ / h) axis values to increment by a uniform value of 0.1, leaving some variation (small) in the location along the horizontal coordinate.

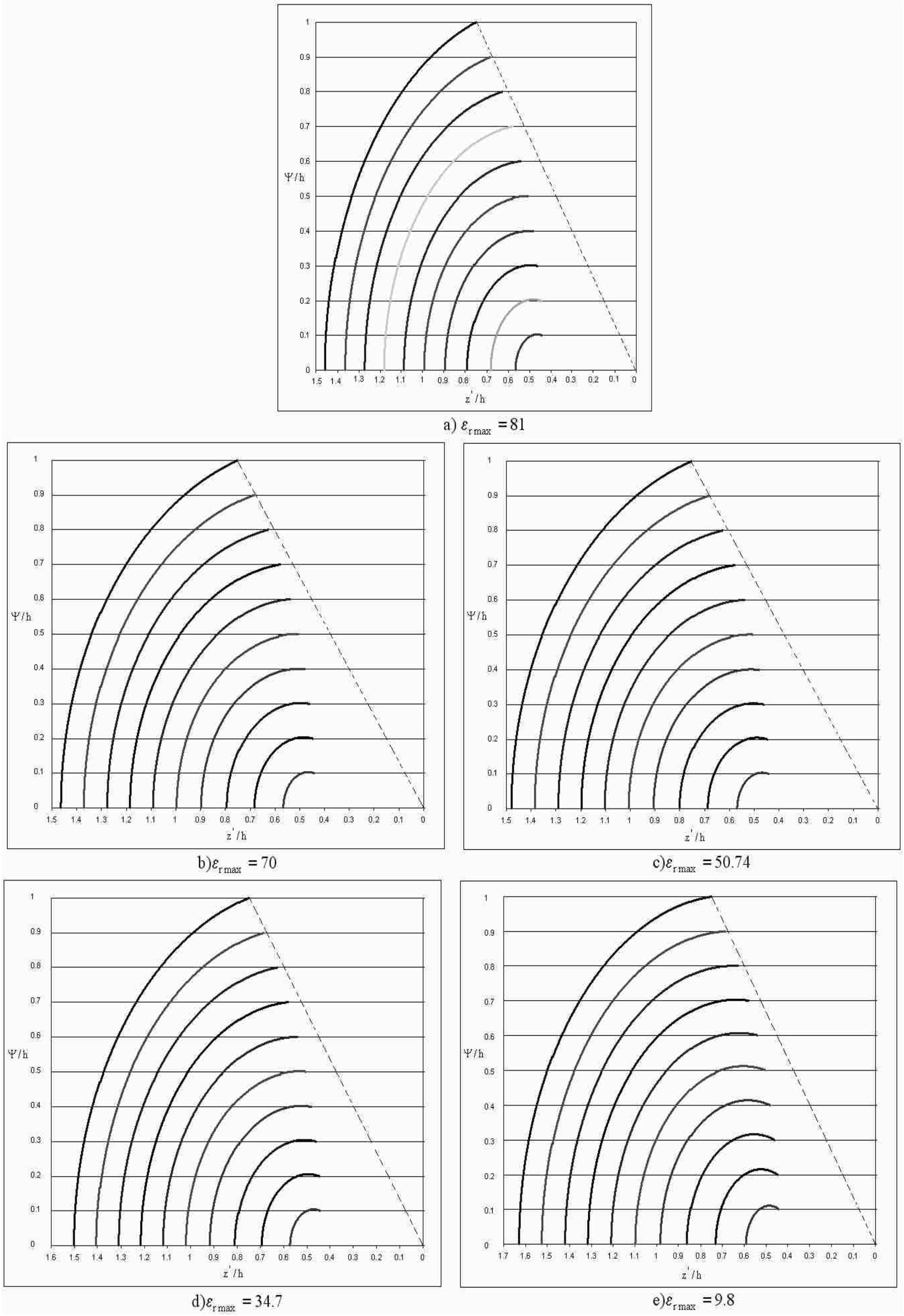

a) $\varepsilon_{r\max} = 81$

b) $\varepsilon_{r\max} = 70$

c) $\varepsilon_{r\max} = 50.74$

d) $\varepsilon_{r\max} = 34.7$

e) $\varepsilon_{r\max} = 9.8$

Figure 7.15: Ψ / h *vs* z' / h for $\theta_{1\,max_{10}} = 90^o$ and different $\varepsilon_{r\,max}$.

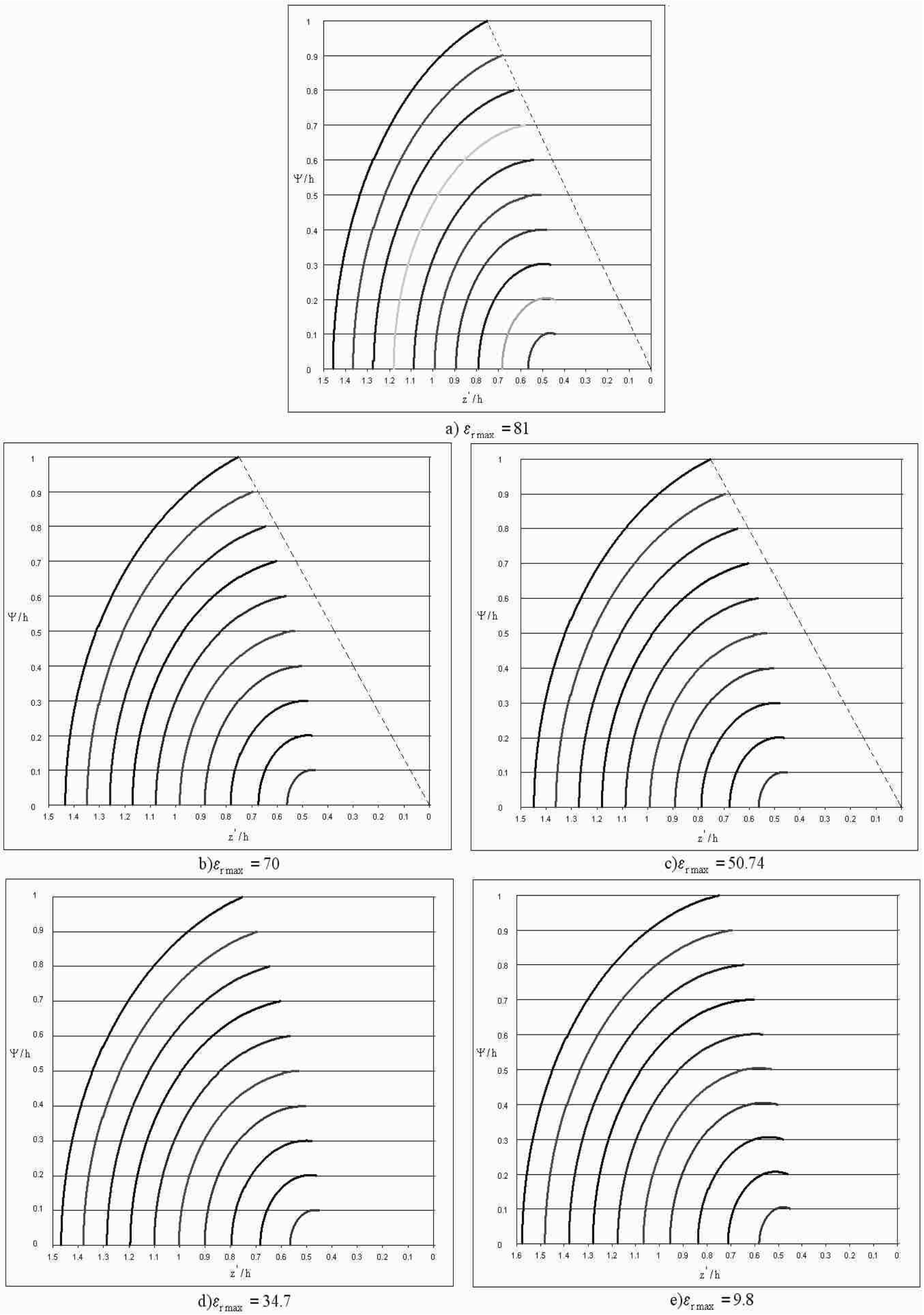

a) $\varepsilon_{r\,max} = 81$

b) $\varepsilon_{r\,max} = 70$

c) $\varepsilon_{r\,max} = 50.74$

d) $\varepsilon_{r\,max} = 34.7$

e) $\varepsilon_{r\,max} = 9.8$

Figure 7.16: Ψ / h vs z' / h for $\theta_{1max_{10}} = 85^o$ and different $\varepsilon_{r\,max}$.

8 CONCLUSIONS

In this dissertation we have designed, constructed and tested a prolate-spheroidal IRA that was designed to be used to kill skin cancer in the near field region. This technique is much more convenient than inserting electrodes near the tumor [1]. This work used analytical calculations, numerical simulations, experiments as well as different lens designs to obtain improved electromagnetic-field concentration at the second focus of a prolate-spheroidal IRA.

First, a parameteric study of the focal waveform produced at the second focus of a prolate-spheroidal reflector was discussed. The optimal dimensions and the z-coordinate of the truncation plane, z_p, for the reflector were found. Then, the analytical behaviors of the focal waveforms of two and four-feed arm prolate-spheroidal IRAs were calculated.

We explored the analytic behavior of the waveform near the second focal region and showed that the impulse part of the waveform at the second focus can be described by a delta-like pulse forming for $z < z_0$ and in the limit as $z \to z_0$ gives the required true delta function. Then, the aperture integral gives the same result (at early time) as the exact incident wave before truncation. We observed that the area of the $\delta-$like pulse was the same for both before and after z_0. We illustrated these results with a graphical example. We continued the analytical evaluation of the prepulse term, E_{p_2}, after the impulse, when the aperture integral is truncated by the aperture edge. The actual analytical waveform was illustrated, including all the terms. These analytical calculations were for a two-arm prolate-spheroidal IRA. However, we have shown that these calculations can be easily extended for 45^o and 60^o four TEM feed arm cases by just multiplying the analytical values by 1.404 and 1.606, respectively.

Finally, the time domain characteristics of some analytic source waveforms, used for determining the waveform characteristic of a prolate- spheroidal IRA at the second focus, were discussed. By appropriate choice at the driving waveform, we maximize the impulse field at the second focus.

CST MWS computer simulations were used for verification of our analytical results. This was a numerical attempt to reproduce the analytical results for the focal waveform of a prolate-spheroidal IRA. We discussed the numerical results for the waveforms near the second focus for spot size analysis. Since we want better concentrating at the second focus, we plan to use a medium that has a higher relative dielectric constant ε_r. This also increases the complexity of our problem; however, experimental results showed that the wave propagation medium with the highest ε_r (in our case it is water $\varepsilon_r = 81$ [1]) is dispersive. We simulated two-arm $400\ \Omega$, 45^o four-arm $200\ \Omega$ and 60^o four-arm $200\ \Omega$ prolate-spheroidal IRAs to obtain the focal waveforms. The spot sizes were analyzed for the two-arm case along the *x*-, *y*- and *z*-axis. We compared our numerical results with analytical results for verification. For future work, we present an equivalent geometry that can be used as an equivalent source to simplify our problem computationally.

We performed several experiments at the UNM Transient Antenna Laboratory in order to compare our experimental results with our analytical and numerical results. Experiments with two-arm and 60^o four-arm prolate-spheroidal IRA were performed.

Experimental setup and problems related with measurements or devices were discussed. Experimental and analytical results were compared. Differences between these results were discussed and the differences were analyzed.

Analytical, numerical and experimental prepulses' amplitude agree very well. The analytical and numerical impulses' amplitudes agree. However, the experimental impulse amplitude was smaller than the others. It was also broader near the base. We have also a feed arm blockage effect that decreases the amplitude of the experimental impulse, however we did not see this effect in our numerical results. Our analytical result was an based on idealized assumption and it did not account for the feed arms. Finally, for all cases the postpulse behaviors were different. However, this part of the pulse was less important for our biological application. Our concern was obtaining the largest possible impulse amplitudes at the focal point to kill skin cancer. The analytical waveform, while simple, is still good, albeit not perfect.

Different lens design procedures were discussed theoretically for better focusing the fields at the second focus of a prolate-spheroidal IRA and having lower spot size. We have a very fast and intense electromagnetic pulse to illuminate the target which is located at the second focal point. For future work, these lens designs can be built and they can be simulated numerically.

APPENDIX

A ANALYTICAL CALCULATIONS FOR THE FOCAL WAVEFORM OF A PROLATE-SPHEROIDAL IRA

A.1 Introduction

This appendix is a summary of [3]. The analytical calculations in [3] were extended in Chapter 4.

Some analytical approximations for the transient focal waveform produced at the second focus of a prolate-spheroidal reflector due to a pulse TEM wave launched from the first focus are developed. This is extended to consider the spot size of the peak field near the second focus.

An inhomogeneous spherical TEM wave launched on guiding conical conductors from one focus is converted by a double stereographic transformation to a second (reflected) inhomogeneous spherical TEM wave propagating toward the second focus [3]. Both waves have the same temporal waveforms before other scattered waves (from feed arms, etc.) can reach the observer.

Inhomogeneous TEM waves in a uniform, isotropic medium (e.g., free space) are exactly transformed by stereographic projection into second such waves in the case of paraboloidal and hyperboloidal scatterers, provided the incident wave is centered on an appropriate focal point (including infinity) of these quadric surfaces [2]. One spherical or planar TEM wave is then transformed into another with an exact matching of the boundary conditions on the (perfectly conducting) reflector. This provides exact solutions of the Maxwell equations, valid up until some time related to a signal arriving at the observer from some truncation of the reflector, or from some structure used to guide the incident wave (i.e., conical or cylindrical perfectly conducting transmission lines). Keeping with bodies of revolution, which give focal *points*, another quadric surface to consider is the prolate spheroid, a special case of an ellipsoid. In this case both focal points are inside the volume enclosed by the surface S_p. Thus, our consideration is to launch an inhomogeneous spherical wave from one focus, and reflect it toward the second.

A.2 Description of Geometry

We are concerned with analytical calculations of the waveform at the second focus in this section. The geometry of the IRA is presented in Figure A.1.

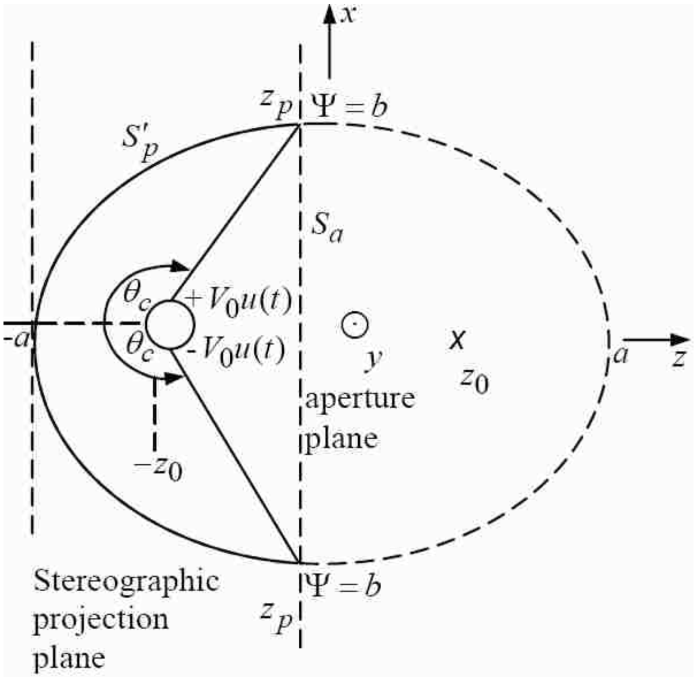

Figure A.1: Schematic diagram of IRA [3].

We have two thin perfectly conducting cone wave launchers with electrical centers lying in the *xz* plane. In the wave-launching spherical system $(r_1\ ,\ \theta_1\ ,\ \phi_1)$ they are oriented at (with respect to the negative z axis) $\theta_1 = \theta_c$. One can relate the $(r_1\ ,\ \theta_1\ ,\ \phi_1)$ system to the cylindrical $(\Psi_1\ ,\ \phi_1\ ,\ z_1)$ and cartesian (x ,y,z) coordinates as

$$\begin{aligned} &\Psi_1 = r_1\, sin(\theta_1)\ ,\quad \phi_1 = -\phi \quad ,\quad z_1 = -z + z_0\ , \\ &x = \Psi_1\, cos(\theta_1) \quad ,\quad y = \Psi_1\, sin(\theta_1) \quad ,\quad z = -z_0 - r_1\, cos(\theta_1)\,. \end{aligned} \tag{A.1}$$

We can describe the prolate spheroid as

$$\begin{aligned} &\left[\frac{\Psi}{b}\right]^2 + \left[\frac{z}{a}\right]^2 = 1 \qquad\qquad 0 \le \phi \le 2\pi, \\ &z_0 = \left[a^2 - b^2\right]^{1/2} \qquad\qquad focii\ at\ \pm z_0\,. \end{aligned} \tag{A.2}$$

We can describe the thin-cone electrical centers by the angle θ_c with

$$\begin{aligned} &\Psi_c = r_c\, sin(\theta_c\,), \\ &z_c = -z_0 - r_1\, cos(\theta_c\,). \end{aligned} \tag{A.3}$$

At the reflector we have (subscript *p*)

$$z_p = -z_0 - \Psi_p\, cot(\theta_c\,)\,. \tag{A.4}$$

If we substitute (A.4) in (A.2), then we have

$$tan^2(\theta_c\,) = \left[\frac{b}{z_0 + z_p}\right]^2 \left[1 - \left[\frac{z_p}{a}\right]^2\right]. \tag{A.5}$$

For given θ_c one can solve for z_p and Ψ_p and we can also specify z_p and compute Ψ_p and θ_c.

We truncate the reflector at the $z = z_p$ plane. The portion used is S'_p, to the left. This is consistent with the traditional truncation of a paraboloidal reflector in impulse radiating antennas (IRAs). More sophisticated truncation contours can be considered, but are beyond the scope of this dissertation. For later use the truncation plane will be taken as an aperture plane. The portion of this plane inside the prolate sphere is designated S_a. It is this surface which will be used for integrating over the reflected TEM wave to find the fields at the second focus, $\overset{\rightarrow}{r_0}$.

A.3 Matching Spherical TEM Waves

We launch an inhomogeneous plane wave from one focus, and reflect it toward the second. In spherical coordinates centered on $-\overset{\rightarrow}{r_0}$ with $\theta_1 = 0$ pointing along the negative z axis (toward the stereo graphic-projection plane), we have an outward propagating (from $-\overset{\rightarrow}{r_0}$) inhomogeneous transient TEM wave as

$$\begin{gathered}
\overrightarrow{E}_1 = -\overrightarrow{r}_0 \nabla_{\theta_1,\phi_1} V_1(\theta_1,\phi_1) f\left(t - \frac{r_1}{c}\right), \\
\nabla^2{}_{\theta_1,\phi_1} V_1(\theta_1,\phi_1) = 0, \\
\nabla_{\theta_1,\phi_1} = \overrightarrow{1}_{\theta_1} \frac{d}{d_{\theta_1}} + \overrightarrow{1}_{\phi_1} \frac{d}{\sin\theta_1} \frac{d}{d\theta_1}, \\
\nabla^2{}_{\theta_1,\phi_1} = \frac{1}{\sin\theta_1} \frac{d}{d_{\theta_1}} \sin\theta_1 \frac{d}{d_{\theta_1}} + \frac{1}{\sin^2\theta_1} \frac{d^2}{d^2\phi_1}.
\end{gathered} \tag{A.6}$$

The stereographic transformation relating spherical TEM waves to cylindrical TEM waves takes the form as

$$\Psi_0 = 2a\left[a - z_0\right]\tan(\theta_1/2)\ , \quad \phi_0 = \phi_0 = -\phi . \tag{A.7}$$

In this projection V_1 satisfies the Laplace equation in cylindrical (Ψ_0, ϕ_0) coordinates.

Here we are imagining a wave launched to the “left” to be reflected on $S_p^{'}$. The portion to the “right”, around the target location, is assumed not used for the reflector, allowing access to the target vicinity. However, the symmetry of the geometry allows one to interchange the roles of source and target. Let us consider a second spherical TEM wave centered (incoming) on $\overrightarrow{r}_0$ of the form

$$\overrightarrow{E}_2 = -\overrightarrow{r}_2 \nabla_{\theta_2,\phi_2} V_2(\theta_2,\phi_2) f\left(t + \frac{r_2 - 2a}{c}\right). \tag{A.8}$$

The projection formula for this wave is

$$\Psi_0 = 2\left[a + z_0\right]\tan(\theta_2/2)\ , \quad \phi_0 = -\phi_2 = -\phi . \tag{A.9}$$

The formulas in (A.6) also apply, substituting subscripts 2 for 1.

Now let

$$V_2(\Psi_0\,,\,\phi_0\,)=-V_1(\Psi_0\,,\,\phi_0\,) \tag{A.10}$$

on the projection plane. Since V_1 satisfies the Laplace equation there, so does V_2. Here we have a diverging wave reflected into a converging wave. Note that the waveforms are the same *f(t)* for these two waves. We merely need to know that $V_1+V_2=0$ (or its tangential derivative, i.e., tangential electric field) on the reflector. On the reflector we have, due to the stereographic transforms

$$V_2(\theta_2\,,\phi_2\,)=-V_1(\theta_1\,,\phi_1\,). \tag{A.11}$$

The two waves match in time as well on the reflector. Differentiating the potential (net zero) on the reflection gives zero tangential electric field, the required boundary condition. This gives an exact solution of the Maxwell equations for times (clear times) before scattering from feed arms and S_p' truncation to S_p' is seen by the observer. Such a clear time is observer-position dependent. For analytical convenience we can take the time-domain waveform as a step function

$$f(t)=u(t), \tag{A.12}$$

applying to both transmitted and reflected waves. The feed arms also fit into the spherical Laplace equation. Their electrical "centers" have been considered in the case of impulse-radiating antennas (IRAs) [27], allowing for placement which in some sense is optimal.

Consider that these intersect S'_p at some z_p. The double stereographic transform then has “image” feed arms pointing to $\vec{r}_0$ from the intersection at z_p. This leads to an interesting symmetry concept by setting

$$z_p = 0 . \tag{A.13}$$

This makes $z = 0$ a symmetry plane between the wave launching side ($z < 0$) and the wave receiving side ($z > 0$). In practice (inverse) feed arms are not included on the receiving side (at least not down to the focal point at $\vec{r}_0$).

A.4 Prepulse

The stereographic projections in the previous section can be used to calculate the fields. Let E_1 have the form

$$\vec{E}_1 = -\vec{r}_0 \nabla_{\theta_1, \phi_1} V_1(\theta_1, \phi_1) f\left(t - \frac{r_1}{c} \right) . \tag{A.14}$$

Let $V_1 = \pm V_0$ on the two cones. The stereographic projection of this wave is

$$\Psi_0 = 2\left[a - z_0\right] tan(\theta_1 / 2) \ , \ \ \phi_0 = \phi_0 = -\phi . \tag{A.15}$$

The electrical center of the thin wire on this projection plane is

$$\Psi_{c0} = 2\left[a - z_0\right] tan(\theta_c / 2) \ , \ \ \phi_{c0} = 0 \ , \ \pi . \tag{A.16}$$

If we use the well–known solution in [28,29] for the two thin wires, we get the prepulse in [3] as

$$E_p = \frac{V_0}{2\pi f_g z_0} tan\left(\frac{\theta_c}{2}\right). \tag{A.17}$$

A.5 Fields at Second Focus

We consider the wave heading from the reflector toward the second focus. There is no set of conical conductors guiding the wave there. Thus, we consider this second spherical TEM wave $\vec{E}_2$ on the aperture plane, which we can use in turn to find the fields at $\vec{r}_0$ (and other positions as well). For present purposes we take the aperture plane as $z = z_p$, the reflected wave illuminates S_a, a disk of radius Ψ_p. Note that the reflector is truncated at the aperture plane. This is because the field from the wavelauncher reverses sign for the wave on the "other side" of the launching conductors. The reflected wave is related to the first wave by a double stereographic transformation. They are equal (except for a minus sign) on the stereographic projection plane for which

$$\begin{gathered} V_2(\Psi_0, \phi_0) = -V_1(\Psi_0, \phi_0), \\ \Psi_0 = 2[a - z_0] tan(\theta_1 / 2) = 2[a + z_0] tan(\theta_2 / 2), \quad \phi_0 = -\phi_1 = -\phi_2. \end{gathered} \tag{A.18}$$

$\vec{E}_2$ is focused on $\vec{r}_0$. Without guiding conductors a double stereographic transformation cannot hold all the way as $r_2 \to 0$. We are therefore considering the fields on S_a for later integration. On the center of S_a we have the electric field E_0

polarized in the $\overrightarrow{1}_x$ direction. In previous papers [29,30] it has been seen that, for circular apertures, the field at the center is an important parameter. The boresight radiated field can be found by integrating the TEM field over the aperture, or by integrating a uniform field of the center value (including polarization) over the same circular aperture. Seen another way, one can expand the field in cylindrical coordinates and note that terms with $cos(m\phi)$ and $sin(m\phi)$ for $m \geq 2$ integrate to zero (for observation field points on the z axis) (there is no m= 0 term). This is basically a symmetry result. for a uniform field E_0 is polarized in the x direction. We can match this field to the second wave at the center of the projection plane and find the x component of the tangential electric field as

$$E_{2x} = 2E_0 \frac{a+z_0}{r_2+z_0-z_p}\left[\frac{z_0-z_p}{r_2}cos^2(\phi)+sin^2(\phi)\right]u(t+\frac{r_2-2a}{c}). \qquad \text{(A.19)}$$

After we evaluate the tangential fields on S_a we can evaluate the fields at $\overrightarrow{r_0}$ by integrating over the fields on S_a. The formulations for the fields at the second focus from a circular aperture that has uniform distribution of electric field were evaluated in (3.3) of [18] and for step excitation we have

$$E_\delta = \frac{V_0}{\pi f_g c} \frac{a+z_0}{a-z_0} \cot\left(\frac{\theta_c}{2}\right) \left[1 - \left[1 + \left[\frac{\Psi_p}{z_0 - z_p} \right]^2 \right]^{-1/2} \right],$$

$$E_s = \frac{V_0}{2\pi f_g} \frac{1}{z_0 - z_p} \frac{a+z_0}{a-z_0} \cot\left(\frac{\theta_c}{2}\right) \left[1 + \left[\frac{z_0 - z_p}{\Psi_p} \right]^2 \right]^{-1},$$

$$E_p = \frac{V_0}{2\pi f_g z_0} \tan\left(\frac{\theta_c}{2}\right), \tag{A.20}$$

$$E_{pa} = E_p \Delta t_p = \frac{V_0}{2\pi f_g c} \frac{a-z_0}{z_0} \tan\left(\frac{\theta_c}{2}\right) \textit{ Area of prepulse, and}$$

$$E_0 = \frac{V_0}{\pi f_g} \frac{1}{a-z_0} \cot\left(\frac{\theta_c}{2}\right),$$

where E_δ and E_s are the impulse and step terms from the reflection from the prolate sphere and E_p is the magnitude of the prepulse wave from first focus (valid up to the time of aperture truncation), z_p is the z-coordinate of the truncation plane, a and b are the two radii for the prolate spheroid, z_0 is the focal distance, and Δt_p is the length of the prepulse and can be defined as

$$\Delta t_p = 2[a - z_0]/c. \tag{A.21}$$

f_g is the transmission line parameter and can be described as

$$f_g = Z_c / Z_0, \tag{A.22}$$

where Z_c *and* Z_0 are the pulse and medium wave impedance.

One can see from (A.20) that E_s has units V/m, while E_δ has units Vs/m corresponding to the time integral (or area) of the δ function. Assuming that the prepulse is a negative E_x, corresponding to a positive potential on the upper feed arms, the reflected pulse reaching toward $\vec{r_0}$ has a positive sign. In [18] the case of the guiding arms is considered by use of an aperture integral. The field at $\vec{r_0}$ has a delta-function part and a step-function part. The detailed calculation was presented in Chapter 4.

A.6 Spot Size Analysis

Figure A.2 indicates the maximum differences from the edges and center of S_a to the observer.

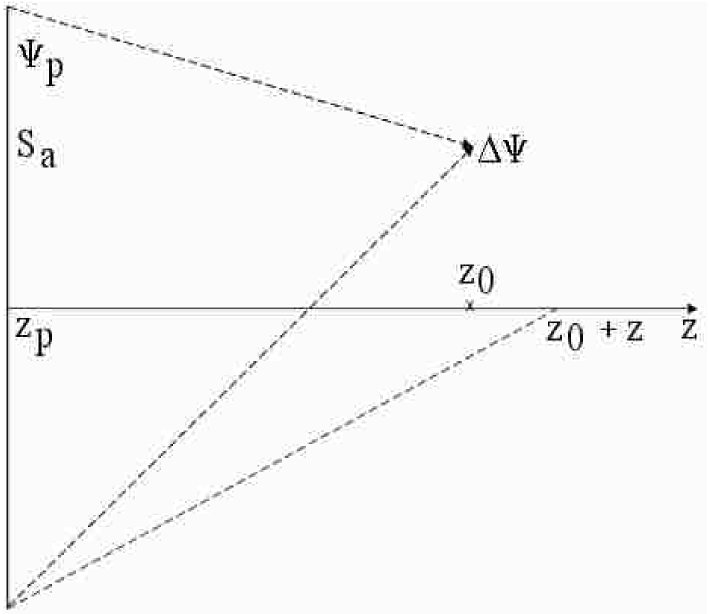

Figure A.2: Spot size of focal waveform [3].

If we have small impulse width t_δ, we will have a really small spot size around $\vec{r_0}$. For the δ-function pulse we have the wave from every position on S_a arriving at exactly the same time at $\vec{r_0}$. We can then estimate a pulse width near $\vec{r_0}$ by the dispersion in the arrival times from all parts of S_a at the observation point.

For $z_p = 0$ the spot sizes in Ψ and z directions are calculated in [3] as

$$\begin{aligned} \Delta\Psi &= \frac{a}{b} c t_\delta , \\ \Delta z &\approx 2\left[1-\frac{z_0}{a}\right]^{-1} c t_\delta . \end{aligned} \tag{A.23}$$

References

[1] K.H. Schoenbach, R. Nuccitelli and S.J. Beebe, “ZAP,” IEEE Spectrum, Aug 2006, pp. 20-26.

[2] E.G. Farr and C.E. Baum, “Prepulse associated with the TEM feed of an impulse radiating antenna,” in Sensor and Simulation Notes #337 (C.E. Baum, ed.), Albuquerque, NM: Phillips Laboratory, 1992.

[3] C.E. Baum, “Focal waveform of a prolate-spheroidal impulse-radiating antenna (IRA),” Radio Science , accepted for publication.

[4] C.E. Baum, S. Altunc, C.G. Christodouou and E. Schamiloglu, “Electromagnetic implosion using an array,” submitted to IEEE Trans. Plasma Science in April 2008.

[5] C.E. Baum, “Radiation of impulse-like transient fields,” Sensor and Simulation Note 321, Nov 1998.

[6] C.E. Baum, E. G. Farr, and D. Giri, “Review of impulse-radiating antennas,” W. Ross Stone, Ed., Review of Radio Science 1996-1999, Oxford U. Press, 1999, pp. 403-439.

[7] W.S. Smythe, *Static and Dynamic Electricip,* Third Ed., Hemisphere, 1989, Sections 6.14 and 12.06.

[8] E.G. Farr and C.E. Baum, “A conical scatterer for transient scattering range calibration,” Sensor and Simulation Notes 342, June 1992.

[9] C.E. Baum and E. G. Farr, “Hyperboloidal scatterer for spherical TEM waves,” Sensor and Simulation Notes 343, July 1992.

[10] C.E. Baum, D.V. Giri and E.G. Farr, 2006 John Kraus antenna Award of the IEEE Antennas and Propagation Society with Citation, “For development of novel and innovative ultra-wideband antenna concepts that have enabled a new area of electromagnetics.”

[11] J.S. Tyo and C.J. Buchenauer, “Experimental verification of the effect of aperture shape on prompt IRA response,” IEEE Trans. Antennas and Propagation, vol. 50, pp. 1032-1034, July 2002.

[12] K. Kim and W.R. Scott , “Analysis of impulse-radiating antennas with ellipsoidal reflectors,” Sensor and simulation Note 481.

[13] D.V. Giri, H. Lackner, I.D. Smith, D.W. Morton, C.E. Baum, J.R. Marek, W.D. Prather, D.W. Scholfield, "Design, fabrication, and testing of a paraboidal reflector antenna and pulser system for impulse-like waveforms," IEEE Trans. Plasma Science, vol. 25, pp. 318-326, April 1997.

[14] C.E. Baum, W.L. Baker, W.L Prather, J. M. Lehr, J.P. O'loughlin, D.V.Giri, I. D. Smith, R. Altes, J. Fockler, D. Mclemore, M.D. Abdalla, and M.C. Skipper "JOLT:A highly directive, very intensive, impulse-like radiator," Proceedings IEEE Special Issue on: Pulse Power: Technology& Applications, vol. 92, pp. 1096-1109, July 2004.

[15] M.J. Baretela and J.S. Tyo, "Improvement of prompt radiated response from impulse radiating antennas by aperture trimming," IEEE Trans. Antennas Propagat., vol. 51, pp. 2158 – 2167, 2003.

[16] S. Altunc and C.E. Baum. "Extension of the analytic results for the focal waveform of a two-arm prolate-spheroidal impulse-radiating antenna (IRA)," Sensor and Simulation Note 518, Nov. 2006.

[17] E.G. Farr, "Optimizing the feed impedance of impulse radiating antennas, part I. reflector IRAs," in Sensor and Simulation Notes #354, C.E. Baum, Ed., Abq, NM: Phillips Laboratory, 1993.

[18] C.E. Baum, "Focused aperture antennas," Sensor and Simulation Note 306, May 1987.

[19] S. Altunc and C.E. Baum, "Comparison of analytical and numerical results for a prolate-spheroidal impulse-radiating antenna (IRA)," Sensor and Simulation Note 519, Nov 2006.

[20] C.E. Baum, "Some considerations concerning analytical EMP criteria waveforms," Theoretical Note 285, Oct 1976.

[21] www.cst.com

[22] C.E. Baum, "Addition of a Lens Before the Second focus of a Prolate-Spheroidal IRA " Sensor and Simulation Note 512, April 2006.

[23] C.E. Baum and J.M. Lehr, "Tapered transmission-line transformers for fast high-voltage transients," IEEE Trans. Plasma Science, vol. 30, 2002, pp. 1712-1721.

[24] M. Converse, E.J. Bond, B.D.V. Veen and S.C. Hagness, "A computational study of ultra-wideband versus for breast cancer treatment," IEEE Transcations on Microwave and Techniques, vol. 54, 2006, pp 2169-2180.

[25] C. Gabriel, S. Gabriel and E. Corthout, “The dielectric properties of biological tissues: I. Literature Survey,” Phys. Med. Boil.vol. 41, 1996, pp 2231-2249.

[26] C.E. Baum , J.J. Sadler and A.P. Stone “A uniform dielectric lens for launching a spherical wave into a paraboidal reflector,” SSN 360, July 1993.

[27] E.22G. Farr and C.E. Baum, “Radiation from self-reciprocal apertures,” Chap. 6, pp. 281-308, in C.E. Baum and H.N. Kritikos (eds.), Electromagnetic Symmetry, Taylor & Francis, 1995.

[28] C.E. Baum, “Impedances and field distributions for symmetrical two wire and four wire transmission line simulators,” Sensor and Simulation Note 27, October 1966.

[29] C.E. Baum, “Aperture efficiencies for IRAs,” Sensor and Simulation Note 328, June 1991.

[30] C.E. Baum, “Circular aperture antennas in time domain,” Sensor and Simulation Note 351, Nov. 1992.